Tension Stiffening in Reinforced Concrete Members with Large Diameter Reinforcement

WENKENBACH, IAN

Ian Wenkenbach

Tension Stiffening in Reinforced Concrete Members with Large Diameter Reinforcement

Abstract

Modern structural designs increasingly often call for the use of large diameter reinforcement as well as full deflection calculations to be carried out in serviceability limit state analysis. In order to achieve this effectively knowledge of the nature of time dependent effects such as tension stiffening is required. There is, however, virtually no experimental data available for reinforced concrete with bar diameters greater than 25 mm. This project aims to identify the behaviour of tension stiffening for reinforced concrete specimens with large diameter reinforcement under sustained loading. Four tension specimens with single H25, H32, H40 and H50 strain gauged reinforcing bars were tested at multiple load stages. In addition, a finite element model was developed in ABAQUS with the aim of evaluating various steel concrete interface models. The applicability of finite element models in the structural analysis of reinforced concrete was also evaluated. The experimental results indicate that the existing conclusions for small diameter cases hold for the larger diameters. Tension stiffening, however, decays at a much higher rate than previously believed and reached a constant value within a maximum of 10 days in each case. The suggestion that only the long-term calculation methods presented in the various building codes for tension stiffening should be used for serviceability limit state calculations is supported. Additionally, a trend is identified which indicates a decrease in tension stiffening decay time with increasing bar diameter.

School of Engineering and Computing Sciences

Tension Stiffening in Reinforced Concrete Members with Large Diameter Reinforcement

Thesis submitted for the degree of
Master of Science

Ian Wenkenbach

2011

Contents

List of Figures

List of Tables

Nomenclature

A	[mm^2]	Total specimen cross-sectional area.
A_c	[mm^2]	Cross-sectional area of concrete.
A_s	[mm^2]	Cross-sectional area of tension reinforcement.
A'_s	[mm^2]	Cross-sectional area of compression reinforcement.
B	[mm]	Specimen width.
D		Scalar damage variable.
D_b	[mm]	Bar diameter.
D_c	[mm]	Concrete test cylinder diameter.
D_n		Scalar damage variable in normal direction.
D_s		Scalar damage variable in tangential direction.
$\mathbf{D^e}$	[N/mm^2]	Bond elasticity matrix for Cox and Herrmann model.
E	[GPa]	Young's modulus.
E_c	[GPa]	Young's modulus for concrete.
E_{ceff}	[GPa]	Long term modulus of elasticity including creep.
E_{c0}	[GPa]	FIB constant (=21.5 GPa).
E_{nn}	[GPa]	Young's modulus of bonding layer in normal direction.
E_s	[GPa]	Young's modulus for steel.
F	[N]	Tensile force on specimen.
I	[mm^4]	Second moment of area about section centroid.
I_{cr}	[mm^4]	Second moment of area for the cracked section.
I_g	[mm^4]	Second moment of area for the uncracked section.
I_{ucr}	[mm^4]	Second moment of area for the transformed uncracked section.
$\mathbf{K}$	[N/mm^3]	Elastic constitutive matrix.
L	[mm]	Concrete specimen length.
L_c	[mm]	Concrete test cylinder length.
M	[Nmm]	Moment in section.
M_a	[Nmm]	Actual moment on section.
M_{cr}	[Nmm]	Cracking moment.
N		Calibration constant Cox and Herrmann model (=1.38).
P	[N]	Concrete cylinder test splitting force.
Q	[mm^3]	First moment of area about the section centroid.
S	[mm]	Crack spacing.

S_0	[mm]	Transfer length.
S_m	[mm]	Average crack spacing.
T	[mm]	Thickness of cohesive layer.
W	[N]	Total load on beam.
a	[mm]	Deflection (Branson method).
a_n		Normal damage evolution equation coefficient.
a_s		Tangential damage evolution equation coefficient.
b	[mm]	Section width.
b_n		Normal damage evolution equation coefficient.
b_s		Tangential damage evolution equation coefficient.
c	[mm]	Concrete cover to reinforcement.
c_s		Tangential damage evolution equation coefficient.
d	[mm]	Section depth.
d_b		Bond zone damage variable.
d_{b0}		Lower limit yield surface interval (=0.38).
d_{b1}		Upper limit yield surface interval (=0.53).
d_{b2}		Bond zone damage at which kinematic softening stops.
d_s		Tangential damage evolution equation coefficient.
f	[MPa]	Model applied tensile stress.
f_c	[MPa]	Concrete stress.
f_{ck}	[MPa]	Characteristic concrete strength.
f_{cu}	[MPa]	Concrete cube strength.
f_t	[MPa]	Concrete tensile strength.
f_s	[MPa]	Stress in tension reinforcement.
f'_s	[MPa]	Stress in compression reinforcement.
f_{yd}	[MPa]	Steel design yield stress.
f^*	[MPa]	Assumed tensile stress supported by concrete.
h	[mm]	Overall model height.
h_s	[mm]	Model reinforcement height.
k_m		Constant related to nature of bending moments.
k_w		Constant related to nature of loading.
l	[mm]	Length along concrete prism.
l_c	[mm]	Model concrete length.
l_s	[mm]	Model steel length.
m		Exponent related Branson equation.
n		Number of cracks.
$\mathbf{q^e}$		Normalised displacement vector for Cox and Herrmann model.
r_u		Ratio of ultimate and maximum displacements (δ_n^u/δ_n^m).
s_r	[mm]	Rib spacing.
$\mathbf{t}$	[MPa]	Traction stress vector.
t_n	[MPa]	Traction component in the normal direction.

t_s	[MPa]	Traction component in the first tangential direction.
t_t	[MPa]	Traction component in the second tangential direction.
t^0	[MPa]	Maximum interface traction before damage occurs.
t^m	[MPa]	Peak interface traction.
t^u	[MPa]	Ultimate interface traction at full interface degradation.
$\bar{t}$	[MPa]	Theoretical elastic interface traction.
w	[mm]	Crack width.
w_m	[mm]	Theoretical crack width.
x_n		Ratio of displacement to displacement at peak traction in normal direction (δ_n/δ_n^m).
x_s		Ratio of displacement to displacement at peak traction in tangential direction (δ_s/δ_s^m).
x	[mm]	distance along member.
Δf	[MPa]	FIB constant (=8MPa).
α		FIB bond model constant (=0.4).
α_1		FIB constant (=0.7).
α_E		Calibration parameter (=0.27).
α_P		Calibration parameter (=0.4).
α_e		Modular ratio (E_s/E_c).
β		Calibration parameter for Cox and Herrmann Model (=2.7).
β_0		Initial calculation variable for Soh, Chiew, and Dong model.
β_1		Coefficient accounting for bond properties of reinforcement in Eurocode 2.
β_2		Coefficient accounting for type of loading in Eurocode 2.
β_u		Ultimate calculation variable for Soh, Chiew, and Dong model.
γ_m		Ratio of initial and peak tangential stiffness coefficients.
γ_u		Ratio of initial and ultimate tangential stiffness coefficients.
δ	[mm]	Deformation or displacement.
$\boldsymbol{\delta}$	[mm]	Separation/displacement vector.
δ_1	[mm]	Deformation for a homogeneous elastic section.
δ_2	[mm]	Deformation for a section ignoring tension in concrete.
δ_m	[mm]	Effective displacement.
δ_m'	[mm]	Effective displacement at full separation.
δ_m^0	[mm]	Effective displacement at damage initiation.
δ_n	[mm]	Normal separation.
δ_s	[mm]	Displacement in the first tangential direction.
δ_t	[mm]	Displacement in the second tangential direction.
δ^0	[mm]	Maximum displacement before damage initiation.
δ^m	[mm]	Displacement at peak traction.
δ^p	[mm]	Plastic slip.
$\bar{\delta}^u$	[mm]	Displacement at which bond is fully broken.

ε		Strain.
ε_{av}		Average strain in concrete member.
ε_c		Concrete strain.
ε_{cs}		Free shrinkage strain.
ε_m		Mean member strain.
ε_{s2}		Strain in reinforcement ignoring the presence of concrete.
ζ		Distribution coefficient indicating the degree of cracking.
η		Factor dependent on amount of tension reinforcement and deflection calculation.
λ	[MPa]	Interface stiffness coefficient.
λ_Δ		Factor for long term deflection.
ξ		Coefficient related to time under load.
ρ		Reinforcement ratio (A_s/A_c).
ρ'		Compression reinforcement ratio.
σ	[MPa]	Stress.
σ_b	[MPa]	Strength of concrete-steel bond.
σ_s	[MPa]	Stress in reinforcement ignoring tension in concrete.
σ_{sr}	[MPa]	Stress in reinforcement at initiation of cracking.
$\hat{\sigma}_0$	[MPa]	Intersect of yield surface with stress axis (=2.25).
ϕ		Creep coefficient.
$(1/r)$	[rad/mm]	Curvature.
$(1/r)_{sh}$	[rad/mm]	Shrinkage curvature.

Declaration

No part of this thesis has been submitted elsewhere for any other degree or qualification and it all my own work unless referenced to the contrary in the text.

Statement of Copyright

Acknowledgements

The author would like to thank Dr. Richard Scott and Dr. Hui Long for providing supervision, support and advice throughout the course of this project; Steve Richardson, Kevan Longley, and the rest of the School of Engineering and Computing Sciences technical staff for their support and patience; and the Durham University School of Engineering and Computing Sciences for providing financial support.

Chapter 1

Introduction

As we enter the second decade of the 21st century civil engineers are frequently presented with new and innovative architectural challenges. There is an increasing demand for large multi-purpose halls with a maximum of floor space and a minimum of columns or other forms of support. In addition, architects specify increasingly slender members in their designs. This does not just make the structure aesthetically pleasing, but also increases material efficiency. The structural design engineer is thus faced with the challenge of designing the smallest possible section for a given span.

For simple members it is common to use span/effective depth ratios in the serviceability design of reinforced concrete beams. It is estimated that this is the method applied in 85% of designs [1]. This could result in conservative member sizes. This is not a problem in simple designs as spans are limited and efficiency is only minimally affected. With the increase in demand for long spans, however, it is more frequently necessary to carry out full deflection calculations for use in serviceability limit state analysis. In order for these to be accurate and efficient in the long term a large number of factors need to be taken into account. These include shrinkage, creep and tension stiffening. Tension stiffening is the least well understood of these three, particularly its behaviour over time.

Traditional calculation methods assumed that all tensile stresses in a beam were carried by the tension reinforcement. This was based on the assumption that concrete is unable to carry any significant tensile stress. This assumption is indeed true at the location of a crack, but in the uncracked zones of the concrete significant tensile stresses can be supported. This resulted in members being stiffer than calculations suggested. It is this extra stiffness which is referred to as tension stiffness. As load is sustained and time dependent cracking occurs tension stiffening decays over time.

Design codes often use a time dependent deflection coefficient to account for the increase in deflection over time due to the loss of tension stiffening. Eurocode 2 [2], for instance, bases the definition of the time dependent deflection factor (β_2) on whether the calculation is for long term sustained loading or short term loading. This is done in order to account for the decay of tension stiffening. There is no guidance as to when

the short term ends and long term begins.

In 2005, Scott and Beeby [3, 4] presented results from an experimental investigation using small diameter (12, 16 and 20 millimetre) reinforcing bars in concrete prisms. These were subjected to sustained tensile loading and the loss of concrete stress was measured over time. The investigation concluded that tension stiffening decay occurs over a very short time period, but no trend could be deduced based on the three diameters investigated.

The increase in span and reduction of member sizes often results in engineers specifying reinforcement with large diameters up to 50 mm. Over the past 40 years a large amount of research has been conducted into time dependent effects affecting deflection such as creep, shrinkage, time dependent cracking and tension stiffening. The largest bar diameters tested experimentally have been limited to 25 mm, however, and there was no experimental data supporting the assumed behaviour of reinforced concrete with 32, 40 or 50 mm reinforcing bars.

This investigation extends the existing data set to include 25, 32, 40, and 50 mm diameter bars. Four uni-axially reinforced tension specimens were cast and subjected to sustained tensile loading. The internal bar strains were measured using gauged reinforcing bars as well as the average surface strains. The use of uniaxially reinforced tensile specimens allowed straight forward accurate calculation of concrete stress using the known tensile load and steel strains.

In addition to the experimental testing program a computational investigation using finite element modelling (FEM) was also carried out. The possibilities for the full analysis of structures using FEM are available, but estimated to only be applied to deflection calculation in 10% of the designs [1]. One reason for this is the lack of a method for applying existing models in a standard finite element software suite. A number of existing bond models are presented and used to define an interface for the concrete-steel bond in the widely used ABAQUS software package. These were then evaluated using the results from the tension tests.

Chapter 2

Literature Review

2.1 Deflection Theory and Reinforced Concrete

Concrete has been one of the main materials used in civil design and construction in the last century. Dating as far back as the Roman Empire and beyond the principles behind concrete construction have remained almost unchanged for a long period of time. With the addition of steel reinforcement, however, the potential of concrete as a construction material increased immensely. The ability to transfer large tensile forces along the steel enabled large beam spans as well as slab design. As the spans increased so did the importance of deflection and deflection control. In the UK the requirement for deflection control associated with such designs was first officially stated in the CP114 Code of Practice of 1948 [5]. Over the decades a large number of research projects were carried out to study the sources of deflection. Particularly the response of deflection under sustained loading over time was of interest as this is a common occurrence in practice. There are three main properties of concrete which affect the response over time: creep, shrinkage, and the loss of tension stiffening. These are briefly introduced below.

2.1.1 Creep

Concrete shows an increase of strain over time during sustained loading even when no cracks form [6]. This is referred to as concrete creep. Figure 2.1 demonstrates this effect through an example [7]. Two stress-strain responses are shown for two identical concrete members, A and B, loaded to an identical final load. In each case the rate at which the load is applied is identical. Curve A shows the response if the load was applied at an uninterrupted constant rate. Due to creep, strains occur over time during the loading process resulting in a curved response. Curve B shows the response if the loading was applied at the same rate as in A, but with two periods during which loading was paused and the section stress remained constant. Although the final load and section stress are identical to that in Member A a higher final strain is achieved. The difference in final strains between the two members is a direct result of concrete

creep. This, in addition to cracks not fully closing, explains why after unloading there can still be significant residual strains present in concrete.

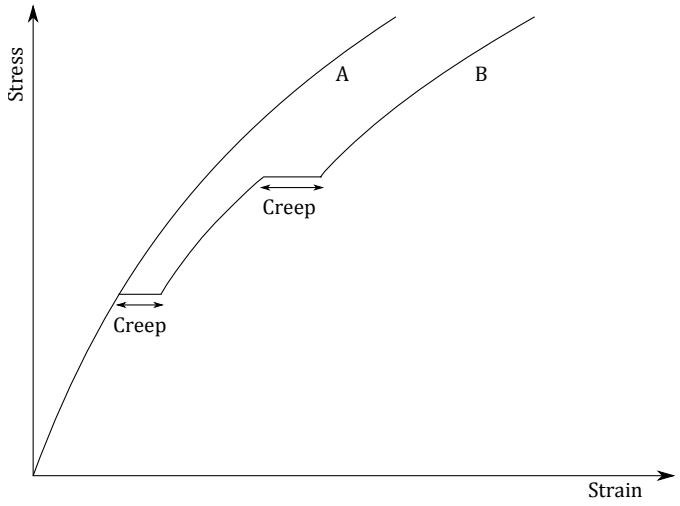

Figure 2.1: Stress-strain curves for two loading paths. [7]

The magnitude of creep is dependent on a number of factors including the concrete strength and age, as well as stress levels. The rate at which creep occurs decreases with the concrete age, and thus the early loading states result in the greatest amount of creep [8].

2.1.2 Shrinkage

Shrinkage is the decrease in volume of a concrete member during the curing process. This occurs due to the combination of a number of effects including aggregate settlement, water evaporation and the hydration reaction between water and cement. The time span over which these effects occur differs from the first hours after casting in the case of aggregate settlement through to indefinitely in the case of the hydration reaction. Figure 2.2 shows a typical shrinkage over time response for concrete. Due to the high dependency of shrinkage rate on relative humidity, temperature, water/cement ratio and specimen geometry there is no single universal shrinkage time response [7]. Additionally, due to shrinkage occurring directly after casting when the concrete is still wet, it is inherently difficult to measure the full shrinkage response [9].

Although shrinkage does not usually result in any internal stresses in simple unrestrained concrete sections, these do arise when the concrete is restrained. This is particularly the case in reinforced concrete where the reinforcement acts as a restraint on the concrete. As a result, significant tensile stresses can be induced in the concrete and internal cracking near the reinforcement can occur [6]. The formation of such internal cracks is important as this leads to a decay of tension stiffening.

Shrinkage, and thus the initial internal strains, can be reduced by providing favourable conditions during curing. These include ensuring a high relative humidity

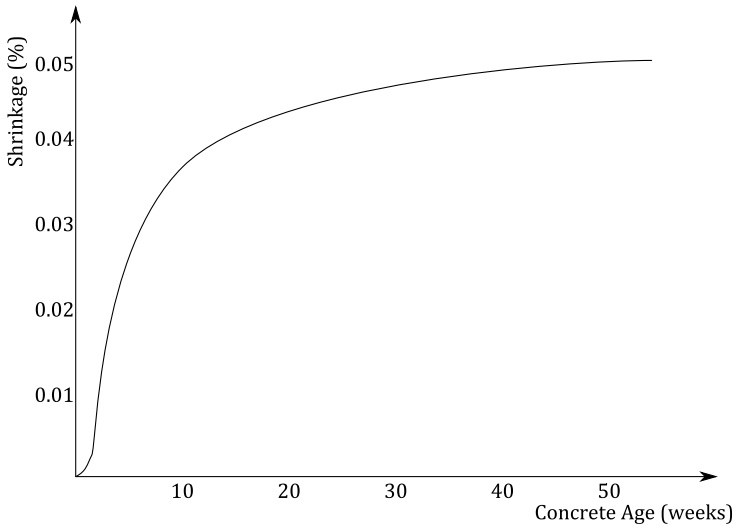

Figure 2.2: Typical shrinkage time response.

by wrapping the specimen in wet hessian and keeping the water/cement ratio as low as possible within the allowable mix design. Use of specialist admixtures can also reduce the effects of shrinkage [10]. Vibrating the concrete during casting also reduces the amount of voids present in the concrete and allows aggregates to settle early in the hydration process.

2.1.3 Tension Stiffening

Tension Stiffening is the least well understood of the time dependent concrete properties and thus still the subject of a large amount of research. It is a direct result of the interaction between the concrete and tensile reinforcement [11]. Tension stiffening is the additional stiffness of a reinforced concrete member attributed to the tensile stresses carried by the concrete. In order to accurately calculate deflections for both beams and slabs this additional stiffness should be taken into account.

The effect of tension stiffening on the deformation of a concrete member is shown in Figure 2.3. As tension is applied to the concrete the deformation initially follows the uncracked response. Once a crack is formed there is a significant increase in deformation. As more cracks form with increased loading the response approaches the line representing the member response in the case of there being no tension carried by the concrete. The additional stiffness originating from the concrete in tension between the cracks, however, limits the deformation to a value less than would be the case if no tension stress were present in the concrete. This difference is the tension stiffening effect [12].

The magnitude of tension stiffening is directly related to the degree of cracking in the concrete. As the cumulative damage to a concrete member increases due to time dependent cracking under sustained loading the tensile capacity of the member

is reduced [3]. Time dependent cracking has been identified to be caused both by shrinkage [13] and construction loading [14]. Tension stiffening is estimated to reach a final value equal to approximately half of its initial value [11]. Tension stiffening is thus time dependent and decays over time with the increase in the degree of cracking.

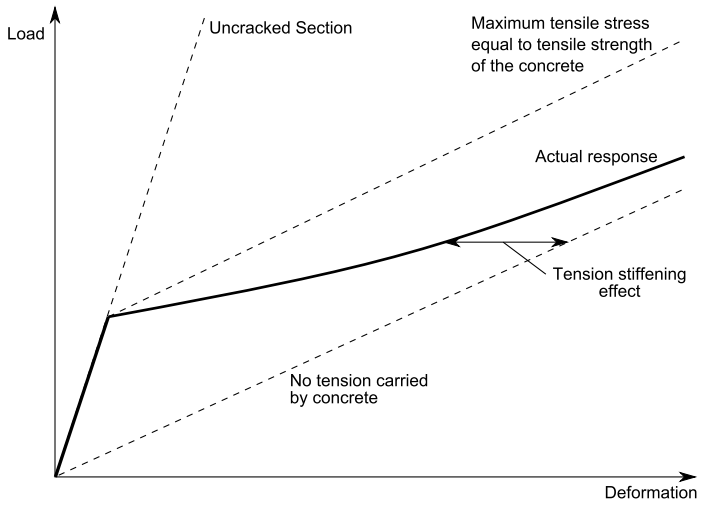

Figure 2.3: Typical load-deformation response for a concrete member. [12]

2.2 Previous Work

The first official UK code of practice, CP114, of 1948 [5] included a short clause on deflection control. Clause 306(a) read as follows:

"Reinforced concrete subject to bending action in a building should possess adequate stiffness to prevent such deflection or deformation as might impair the strength or efficiency of the structure, or produce cracks in finishes or in superimposed partitions, etc."

No guidance on the implementation of this statement was provided. As knowledge of the behaviour of deflection, cracking and the internal strain and stress distributions developed the codes were regularly updated, as described in Section 2.3. What follows is a brief review of the main research over the past decades into deflection, cracking and time dependent effects in reinforced concrete.

In 1951 Mains [15] developed a method for the measurement of strains inside a reinforcing bar. His method consisted of the placement of electrical stain gauges within a cavity running down the centre of a 7/8 inch (22.2mm) diameter reinforcing bar. This was the first investigation in which bar strains were measured directly without affecting the bond properties of the reinforcement. A number of pull out tests were performed, as well as a series of bending experiments. The strain distributions along

the bars were measured at intervals ranging from 2 to 4 inches. Mains concluded that cracking decisively affects the distribution of tensile and bond stresses along the bar. In addition measured peak strains were found to be above calculated values.

Yu and Winter [16] identified a need for serviceability deflection calculations due to the introduction of high yield steels and higher quality concrete in 1960. These improved materials allowed for increasingly shallow members which satisfied ultimate failure criteria, but were prone to large deflections. Two methods for deflection calculations were developed based on 175 deflection tests. An attempt was made to link long term deflections to short term deflections using a single multiplier. It was recognised that such a direct relation did not exist, but that a multiplier related to the duration of loading and reinforcement conditions could result in a good estimate. This relation was derived empirically from 68 test results with a maximum bar diameter of 22.2 mm. Inaccuracies in the long term deflection predictions were attributed to shrinkage, creep and cracking.

In 1963 Hajnal-Konyi [17] presented the results from a set of long term sustained loading experiments. Six beams were subjected to sustained loads over a period of over 4 years. The maximum reinforcement diameter in these tests was 12.2 mm. Hajnal-Konyi concluded that serviceability (deflection) calculations were required even when the member satisfies the 1957 CP114 slenderness ratios. As the codes of practice based calculations on the fact that concrete in tension carries no tensile stresses it was suggested that slenderness ratios should be based on the effective member depth instead of the total member depth. Finally, however, he concluded that methods taking the tension in concrete before cracking into account, such as those applied by the CEB Model Code [18], provided the best estimates.

In 1963 Branson [19] developed a relation for curvature and deflections directly from elasticity theory. This method was adopted by the deflection committee of the American Concrete Institute (ACI 435) in 1966 [20]. The ACI then adopted the Branson method in their ACI 318 building code [21]. The full method is presented in Section 2.3.3. Long term deflections are calculated through the application of a factor to the short term deflection which is based on reinforcement ratio and the time period over which sustained loading is applied.

The first published application of finite element models to reinforced concrete was presented in 1967 by Ngo and Scordelis [22]. Their model was based on triangular constant strain elements representing the steel and concrete. A special set of bond link elements were used to model the steel concrete interface. Simple beams were modelled using a predetermined cracking pattern. Non-linear effects were not taken into account and the analysis was limited to linear elasticity. Ngo and Scordelis did, however, show that the application of finite element analysis to reinforced concrete was possible.

Beeby [23] developed a number of empirical methods for the calculation of short term deflection and evaluated existing formulae based on a large set of experimental data in 1968. Both the Yu and Winter method [16] and the Branson method [19] were

identified as providing similar results which were determined to be the most accurate of the existing methods. Beeby suggested two new methods. The first was based on the moments of inertia and the difference between the applied moment and cracking moment. The second defined a bilinear curvature-moment curve which could be used to graphically provide the curvature of a section under load. The response of deflection over time was not considered.

In 1968 Nilson [24] presented the development of a finite element model for reinforced concrete. This model took into account the influence of reinforcement, progressive cracking, bond stress transfer and non-linear material properties. Some simple analyses were performed and compared to experimental results. The validation of the models was identified as the main limitation to applying the model to other cases. Little experimental information was available for the definition of model properties. The developed model provided a significant improvement on the Ngo and Scordelis [22] model.

An investigation carried out by Goto [25] in 1971 provided a unique insight into cracking mechanisms. Tension was applied to the reinforcement in a series of uni-axially reinforced concrete prisms. During loading, ink was injected into the concrete in order to colour any internal cracks which formed within the members during loading. Once unloaded, the prisms were split and the crack patterns photographed. This led to the identification of internal crack mechanisms and the determination of the schematic deformation diagram shown in Figure 2.4.

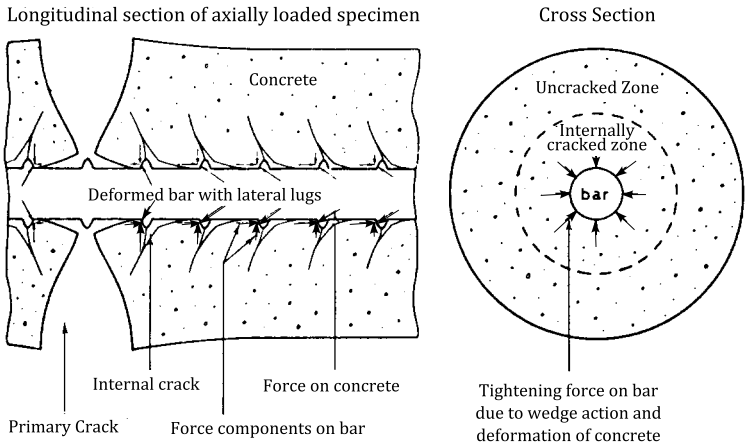

Figure 2.4: The schematic deformation of concrete in a tension specimen. [25]

In 1972 Illston and Stevens [26] presented the results from an investigation in which 60 beams were loaded for a maximum duration of two years. The focus of the investigation was to determine the effect of concrete cover on crack widths over time. Reinforcement with a diameter of 32 mm was used in a small number of test beams. The initial average crack spacing was determined to be 2.3 times the effective

concrete cover. Cracks were observed to grow at a diminishing rate. Illston and Stevens concluded that this diminishing increase in crack width was the result of a reduction of the average tensile strains in the concrete. This was attributed to shrinkage and time dependent curvature changes. The crack widths were thus linked to the shrinkage strain and the steel strain under sustained loading.

An outline of the mechanism by which primary cracks form and the final crack pattern is reached was presented by Beeby [27] in 1972. This theory assumes that the transfer of stress through the concrete and steel bond takes place over a fixed transfer length (S_0). After a first crack forms the next crack will then not form within S_0 of the first crack as the stresses in the concrete are lower within this limit than outside. This process continues until there is no longer any region which lies a distance greater than S_0 from a crack. Figure 2.5 illustrates this process.

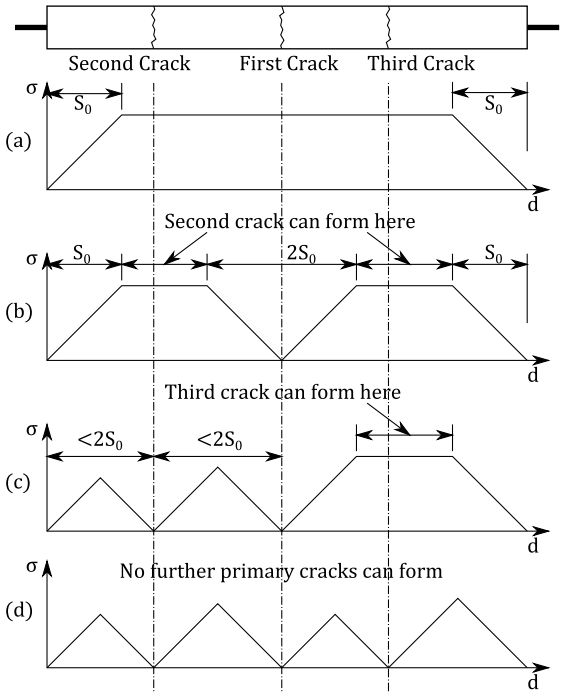

Figure 2.5: The mechanism by which cracks form in a uni-axially reinforced concrete prism under tension. [27]

The prism ends respond in a manner similar to cracks. As a result the first crack can form anywhere along the member outside S_0 of the ends, as shown in Figure 2.5(a). The second crack can then form in any of the remaining regions where there is no stress transfer between the steel and the concrete as shown in Figure 2.5(b). As the distance between the first and second crack, as well as the second crack and the end of the member, is less than $2S_0$ no further cracks can form in this region. On the right hand side of the member, however, there is still a zone in which there is no reduction in concrete stress. It is in this zone that the third and final primary crack can form, as shown in Figure 2.5(c). After this crack has formed there is no longer any region in the

member more than S_0 from a crack and as a result no further primary cracks can form (Figure 2.5(d)). This final distribution of crack spacing (S) must be within the range shown in Equation 2.1. Cracking can still occur as during tension tests at high load levels internal (secondary) cracks can occasionally reach the surface and form cracks within the bonding zones.

$$S_0 \leq S \leq 2S_0 \tag{2.1}$$

where:

S_0 = Transfer length

S = Crack spacing

Rao and Subrahmanyam [28] presented a tri-segmental moment-curvature relationship in 1973. They identified that previously suggested bilinear curves provide a significant over estimation of the curvature. In some cases this was observed to be as high as 100%. During the development of this semi-empirical method the tension in the concrete was taken into account. This was thus the first deflection calculation method which explicitly considered the tension stiffness in a member.

In 1978 Clark and Speirs [29] provided the results from an investigation specifically focused on tension stiffening in beams and slabs. Tests were carried out with reinforced concrete specimens which contained a maximum bar diameter of 25 mm. Deflections and surface strains were measured, the latter using a 200 mm Demec gauge. The report concluded that tension stiffening could be calculated using the average concrete tensile stress, which in turn is a fraction of the concrete tensile strength. The reduction of tension stiffening is linked to the increase in member strains, where the rate was dependent on the bar spacing.

Clark and Cranston [30] concluded in 1979 that the maximum tension stiffening force in a member was a function of the tensile strength of concrete and the area of concrete below the neutral axis. They also concluded that tension stiffening could be considered independent of bar spacing. Additionally they presented a method for the determination of steel strains for which tension stiffness is a maximum based on the ratio of the second moments of area for the full and cracked sections. Finally Clark and Cranston determined that the CEB Model Code [31] methods correctly estimated tension stiffening while the CP110 [32] method resulted in an over estimation of stiffness.

Floegl and Mang [33] analysed the use of tension stiffening factors using finite element models in 1982. These factors were derived on the basis of bond slip and were directly proportional to cracking characteristics, such as spacing, and inversely proportional to the bar diameter, amongst others. The short term response of a number of panels was predicted using the finite element method as an analysis tool. This resulted in predictions which agreed well with experimental results. The finite element model did not, however, discreetly model the reinforcement and did not provide an indication of the mechanisms present in the panel.

In 1987 Scott and Gill [34] performed an experimental investigation using seven tensile specimens with gauged reinforcing bars. The bar diameters were limited to 12 mm and 20 mm and had a gauge spacing of 12.5 mm. The strain distributions along the bars were plotted with great accuracy. The load deformation plot was recognised to be a series of discontinuities instead of the until then assumed single curve. Each discontinuity occurred at the formation of a crack. The stiffness of the specimen thus decreased with the formation of each crack. In addition, the variation in steel strain adjacent to a crack location was observed to be a linear decrease as shown in Figure 2.6. The variation of bond stresses with load was still linear, however, and hence this could not be attributed to plastic behaviour.

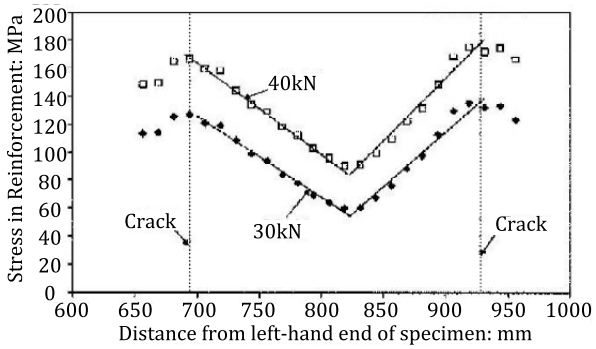

Figure 2.6: Typical bar stress distribution for a Scott and Gill specimen. [34]

In 1999 Gilbert [13] identified deficiencies in the official methods for deflection calculation, namely the Australian standards, but also the ACI 318 (Branson) method [21, 19]. On the basis of experimental data Gilbert demonstrated that for lightly reinforced beams and slabs the loss of stiffness over time due to cracking was not adequately calculated. This resulted in an underestimation of deflection by the design codes. Gilbert concluded with the evaluation of three new methods for deflection calculation, all of which provided an improved estimate for the experimental results considered. The loss of tension stiffening due to cracking over time was attributed to shrinkage.

Vollum [14] and Vollum, Moss and Hossain [35] showed in 2002 that tension stiffening is lost at a higher rate under loading than could be attributed to shrinkage. On the basis of a number of previous test results and measurement of deflection during in situ construction loading of slabs in a building at Cardington, a number of recent methods for deflection calculation were evaluated. The 1990 FIB-CEP Model Code [36] approach to accounting for tension stiffening was observed to provide good results, particularly with some small suggested modifications. Vollum concluded that in cracked members shrinkage no longer significantly contributes to the loss of tension stiffening after loading.

Scott and Beeby [4] performed a large investigation into tension stiffening and

presented their results in 2005. A large number of tension specimens were tested with bar diameters ranging from 12 mm to 20 mm in specially designed tension rigs [37]. A number of members were subjected to up to three load stages. Tension stiffening was determined to decay over a period ranging from less than a day to 4 weeks. The stress levels in the reinforcement as well as the concrete strength were observed to have no effect on the results. In addition a small number of slabs were tested in order to compare the rate of tension stiffening decay between tension specimens and slabs. Scott and Beeby concluded that these rates were similar. In view of the short decay times Beeby, Scott and Jones [38] recommended alterations to the major design codes as described in Section 2.3. These effectively eliminated short term calculations for deflections, supporting only long term deflection calculation.

Beeby and Scott [39] also presented a method for calculating average strains in a tension member based on transfer length and crack spacings in 2004. This was developed based on the experimental results from their long term investigation described above. Equation 2.2 provides the average strain in cracked concrete members [39].

$$\varepsilon_{av} = \begin{cases} \dfrac{\varepsilon_{s2}(\alpha_e\rho + S_0 n/L)}{1+\alpha_e\rho} & S_m \geq 2S_0 \\ \dfrac{\varepsilon_{s2}(1+\alpha_e\rho - S_m/(4S_0))}{1+\alpha_e\rho} & S_m < 2S_0 \end{cases} \tag{2.2}$$

where:

ε_{av}	=	average strain in the cracked concrete member
ε_{s2}	=	strain in the reinforcement ignoring the presence of the concrete
α_e	=	modular ratio (E_s/E_c)
ρ	=	reinforcement ratio (A_s/A_c)
n	=	number of cracks
L	=	specimen length
S_m	=	average crack spacing

For the evaluation of average strain a prediction of the number of cracks that will form in a member must be made. Although this is still a subject of ongoing research [40, 41], an estimation can be made using a combination of Equation 2.1 and experimental results.

In 2005 Bischoff and Scanlon [42] suggested a new method for deflection calculation. This consisted of replacing the effective moment of area equation defined by Branson [19] with a new equation, known as the Bischoff equation. This is presented below in Section 2.3.3. In 2006 Gilbert [43] conducted an evaluation of the Bischoff equation and found this to provide significantly more accurate results in deflection modelling. The good results were not limited to steel reinforced concrete members as deflections in glass fibre reinforced polymer bar specimens were also accurately estimated. It was also identified that the more instantaneous nature of tension stiffening is incorporated in this method.

Vollum and Afshar [44] presented results from a series of tests on one way slabs in

2009. The aim was to investigate the effect of peak construction loading on the long term tension stiffening response and deflections. This showed that long term deflections could be governed by peak loading during construction. In addition, a refinement to the Eurocode 2 deflection calculation method was presented. This is described in more detail in Section 2.3.2. A significant amount of variation between deflection predictions and measurements is attributed to the variation of concrete tensile strength. A final conclusion was that although tension stiffening was observed to decay rapidly in cracked slabs this was not as rapid as observed by Scott and Beeby [4].

2.3 Design Codes

Over the last decades the various design codes have developed from a simple recognition that deflection should be considered to the various detailed guidelines for deflection calculation they provide today. The methods and developments of three main codes are presented here: The UK codes ranging from CP114 [5] to the now superseded BS8110 [45], the European CEB [31] Model Code and its development into Eurocode 2 [2] and the American ACI 318 building code [21].

2.3.1 CP114, CP110 and BS8110

The first code of practice, CP114 [5], in 1948 limited its deflection section to the statement presented previously in Section 2.2. Although a true point, even today [46], no further guidance was provided. In the 1957 revision a simple table of span/effective depth ratios was provided for beams and slabs. In order to accommodate specimens with high steel or concrete stresses a number of modification factors were provided which resulted in a reduced ratio.

As the code progressed through CP110 to BS8110 [45] the basic approach of using span/effective depth ratios was maintained. The overall aim of BS8110 is to limit total deflection to $Span/250$ and the post construction deflection to the smaller of $Span/500$ or 20 mm for beams with a maximum span of 10 metres.

BS8110 provides span/effective depth ratios depending on whether the beam is a cantilever, simply supported or continuous. In order to accommodate alternative deflection limits other than $Span/250$ the span/effective depth ratio can be multiplied by $250/Required\ limit$. For deflection limits other than 20 mm the ratio is multiplied by $Required\ maximum\ deflection/20$. The final ratio is multiplied by a pair of modification factors related to the tension and compression reinforcement which are both dependent on the service stress.

BS8110 allows deflection to be calculated using numerical integration or a simplified formula at the critical section. An average amount of tensile stress is assumed to be supported in the concrete along the entire length of the member as shown in Figure 2.7. This value (f^*) is taken to be 1 MPa for short term loads and 0.55 MPa for

long term loads. The long term value (0.55 MPa) can then be used in combination with the effective modulus of elasticity accounting for creep and the curvature due to shrinkage to determine deflection. The effective modulus of elasticity accounting for creep is calculated according to Equation 2.3.

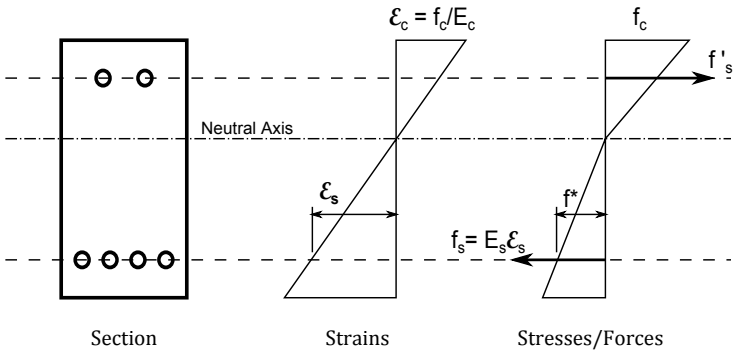

Figure 2.7: BS8110 assumption for stresses and strains in cracked section. [11]

$$E_{ceff} = \frac{E_{c,28}}{1+\phi} \tag{2.3}$$

where:

E_{ceff}	=	effective modulus of elasticity accounting for creep
$E_{c,28}$	=	modulus of elasticity of concrete at 28 days
ϕ	=	creep coefficient

The curvature due to shrinkage can be calculated using Equation 2.4.

$$(1/r)_{sh} = \varepsilon_{cs}\alpha_e\frac{S}{I} \tag{2.4}$$

where:

$(1/r)_{sh}$	=	curvature due to shrinkage
ε_{cs}	=	free shrinkage strain
α_e	=	modular ratio (E_s/E_c)
S	=	first moment of area of reinforcement about the section centroid
I	=	second moment of area of the section

Deflections can be calculated through numerical integration based on the relationship shown in Equation 2.5.

$$(1/r_x) = \frac{d^2a}{dx^2} \tag{2.5}$$

where:

a	=	deflection
$(1/r_x)$	=	curvature at x
x	=	distance along member

Alternatively the deflection at the critical section, mid span for beams and support

for cantilevers, can be calculated using the simplified expression shown in Equation 2.6

$$a = k_m L^2 (1/r) \tag{2.6}$$

where:

k_m	=	factor depending on form of moment diagram
L	=	span length
$(1/r)$	=	curvature

2.3.2 CEB-FIP and Eurocode 2

Eurocode 2 [2] is based on the preceding CEB-FIP Model Codes. This method is based on a weight factor to achieve a balance between the deformation for a homogeneous elastic section (δ_1) and the deformation calculated when tension in the concrete is ignored (δ_2). This weight factor is referred to as the distribution coefficient which provides an indication of the degree of cracking. Equation 2.7 shows the way in which this relationship is set up.

$$\delta = \zeta\delta_1 + (1 - \zeta)\delta_2 \tag{2.7}$$

where:

δ	=	deformation (can be expressed as curvature or strain)
ζ	=	distribution coefficient
δ_1	=	deformation for a homogeneous elastic section
δ_2	=	deformation for the section where tension in the concrete is ignored

The distribution coefficient is defined using bond properties, character of loading, and reinforcement stresses as shown in Equation 2.8.

$$\zeta = 1 - \beta_1\beta_2 \left(\frac{\sigma_{sr}}{\sigma_s}\right)^{\alpha} = 1 - \beta_1\beta_2 \left(\frac{M_{cr}}{M_a}\right)^{\alpha} \tag{2.8}$$

where:

β_1	=	coefficient related to bond properties of the reinforcement (1.0 for ribbed bars and 0.5 for plain bars)
β_2	=	coefficient defined by the type of loading (1.0 for single short-term loads and 0.5 for repeated sustained loads)
M_{cr}	=	cracking moment
M_a	=	actual (serviceability) moment on the section
σ_{sr}	=	stress in the reinforcement due to M_{cr} if tension within the concrete is ignored
σ_s	=	actual reinforcement stress due to M_a if tension within the concrete is ignored

The recent FIB model codes [47] no longer apply the β_1 factor to this calculation.

The presence of creep is taken into account through the same method as BS8110 using the long term modulus of elasticity, E_{ceff}, as calculated in Equation 2.3 using the creep coefficient. Similarly shrinkage deformation is taken into account using the curvature due to shrinkage, $(1/r)_{sh}$, which is calculated using Equation 2.4.

The shrinkage curvature can be determined to be of a sufficient magnitude to indicate that the section is cracked. In this case both the first and second moments of area must be evaluated for the cracked and uncracked section. Equation 2.7 can then be used, taking curvature as the deformation δ, to determine the final curvature. The long term deflection can thus be calculated using $\beta_2 = 0.5$ and the values for creep deflection and shrinkage curvature.

Beeby, Scott and Jones [38] suggested only allowing the use of $\beta_2 = 0.5$ for both long and short term deflections to account for the rapid decrease in tension stiffening observed in the Durham and Leeds tension tests. Recently, however, Vollum and Afshar [44] have suggested a method for the calculation of β_2 for short term loading during the construction period. The distribution coefficient is then taken as the greatest of either that determined using the calculated value of β_2 or that determined using the long term value of $\beta_2 = 0.5$.

2.3.3 ACI 318

The American Concrete Institute has adopted the Branson method in their building code ACI 318 [21] and their more detailed deflection recommendations in ACI 435 [48]. Branson derived the following relations for curvature and deflections directly from elasticity theory [19, 49].

$$(1/r) = \frac{M}{EI} \tag{2.9}$$

$$a = \frac{k_w W L^3}{EI} \tag{2.10}$$

$$a = \frac{k_m M L^2}{EI} \tag{2.11}$$

where:

M	=	moment at the critical section
E	=	modulus of elasticity
k_w	=	coefficient related to the nature of loading
k_m	=	coefficient related to the nature of the bending moments
W	=	total load on the beam

In order to evaluate Equations 2.9 through 2.11 a definition for the second moment of area is required which takes into account the cracked and uncracked moment of areas along the section. This is done using a weighted approach similar to that used

for deflections in Equation 2.7.

$$I_e = \left(\frac{M_{cr}}{M_a}\right)^m I_g + \left[1 - \left(\frac{M_{cr}}{M_a}\right)^m\right] I_{cr} \leq I_g \tag{2.12}$$

where:

I_e = effective second moment of area
I_g = uncracked second moment of area
I_{cr} = cracked second moment of area
m = exponent (3 for use in Equation 2.9 or 4 for use in Equations 2.10 and 2.11)

The difference in the value of the exponent m originated from the fact that Equation 2.9 is based on the local state of cracking while the others take into account the cracking along the entire member length. ACI 318 adopts the value of 3 in combination with Equations 2.10 and 2.11 for the calculation of a short term deflection. The long term deflection is then found by multiplying this by the factor λ_Δ.

$$\lambda_\Delta = \frac{\xi}{1 + 50\rho'} \tag{2.13}$$

$$\rho' = A'_s/bd \tag{2.14}$$

where:

ρ' = compression reinforcement ratio
ξ = coefficient dependent on the time under load
A'_s = area of compression reinforcement
b = section width
d = section effective depth

For the coefficient ξ ACI 318 suggests values of 1.0, 1.2, 1.4 and 2.0 for three months, six months, twelve months and longer than 5 years respectively.

Bischoff [42] recently identified shortcomings in the method proposed by Branson. Experimental analysis showed that Equation 2.12 overestimates deflection for members with small amounts of steel reinforcement ($A_s/bd < 1\%$) and lightly reinforced slabs where $I_g/I_{cr} > 3$. The following replacement is suggested.

$$I_e = \frac{I_{cr}}{1 - (1 - I_{cr}/I_{unc})(M_{cr}/M_a)^2} \leq I_{unc} \tag{2.15}$$

where:

I_{unc} = second moment of area for the uncracked transformed cross-section

For lightly reinforced members the second moment of area for the uncracked transformed cross-section is approximately equal to I_g. This method also performs well for concrete with glass fibre reinforced polymer reinforcement [43]. The more instantaneous

nature of tension stiffening is incorporated within the I_{cr}/I_{unc} factor. ACI committee 435 [48] will be adopting this in the next revision of their deflection recommendations.

2.4 Conclusion

Although a large amount of work has been carried out in an attempt to develop methods for deflection calculation very few have focussed on the tension stiffening effect. The first experimental investigation focussed specifically on tension stiffening was only presented in 1978 by Clark and Speirs [29]. Since then a number of other research projects have taken place and the knowledge of tension stiffening has improved significantly over the last decade. Particularly the research by Scott, Beeby and others [4, 40, 3] as well as that carried out by Vollum and others [14, 35, 44] has provided useful insights into the mechanisms which govern tension stiffening.

The majority of previous investigations have relied on a combination of load and deflection measurement. A number of investigations have used mechanical strain gauges for the recording of average surface strains. As cracking has been identified as one of the main sources for the loss of tension stiffening it is important to have an understanding of the local strain distributions. The knowledge of local stress and strain distributions was limited to those investigations using gauged reinforcing bars.

In modern designs the use of large diameter reinforcing bars has become increasingly popular. All experimental data on tension stiffening and deflection in the past have been limited to a diameter of 25 mm, with the exception of a small number of experiments conducted by Illston and Stevenson [26]. However, these experiments were limited to investigating crack growth. As a result there is a lack of experimental data for the larger bar diameters ranging from 25 mm to 50 mm.

In addition there are large inconsistencies in the methods set out by the design codes for the calculations of deflections. The implementation of tension stiffening remains one of the main factors affecting the accuracies of deflection estimates. The decay of tension stiffness over time in members is not represented accurately in the combination of long and short term calculation methods. Finally there is a lack of guidance as to where the boundary between short term and long term lies.

There is thus need for confirmation regarding the behaviour of reinforced concrete members with large diameter bars and the time over which the loss of tension stiffening occurs. This confirmation can best be achieved through an experimental program in which reinforced concrete members are subjected to sustained loading. Strain gauged bars have proven a reliable method for the recording of strain distributions along reinforcing bars.

There have been a number of investigations using finite elements to analyse the behaviour of reinforced concrete such as those by Nilson [24] and Floegl and Mang [33]. Most of these were developed for a single application and are not easily widely applicable. With the increasing popularity of finite elements various models have been

developed for the modelling of composite concrete structures. The implementations of these models into a single widely available software suite such as ABAQUS [50] has been neglected, however. Chapter 5 investigates this possibility.

Chapter 3

Experimental Method

3.1 Overview

The experimental part of this investigation was based on a tension test program. The main aim was to measure the decay of tension stiffness over time under a sustained load in concrete members with four different large diameter reinforcing bars. This was achieved by approximating the tension zone in a concrete beam as a uni-axially reinforced concrete prism. The use of tension members allowed direct calculation of concrete stress using the tensile load and internal bar strains. This approach was validated in a previous investigation by Scott and Beeby [12] using a limited number of tests on slab specimens subjected to bending. The time over which tension stiffening decayed was similar in the slabs compared to the associated tension specimens despite significantly different cracking patterns. For this investigation four uni-axially reinforced concrete prisms were cast, each containing a different large diameter bar. The bar diameters investigated were 25, 32, 40 and 50 mm. In order to achieve multiple data sets for each diameter each specimen was subjected to three load stages where possible. Strains along the bar and on the concrete surface were measured as well as the load to determine the decay of tension stiffening. Measurements were taken using strain gauged reinforcing bars and Demec studs and gauge for the steel and surface strains respectively. A load cell was used to measure the true applied load. The electronic strain gauges were read using a data logger and computer while the Demec gauge was read manually. The following sections describe the specimens, materials, apparatus and methods used in this experimental stage of the project in detail.

3.2 Testing Program

The four tested specimens were designed to optimise the comparison of the results from this investigation with previous existing results. A previous investigation conducted at Durham and Leeds by Scott and Beeby [4, 3] used three sizes of small diameter bars with diameters of 12, 16 and 20 mm. These were cast in 120 mm square concrete

prisms. In order to allow direct comparison with this previous testing program the prism dimensions for the large diameter bars were designed to result in reinforcement ratios similar to those in the 16 mm and 20 mm specimens in the previous investigation.

The loading stages were similarly determined such that the stresses in the reinforcement were similar to those induced in the Scott and Beeby testing program. This implied that each load stage would result in an average concrete stress of 3, 4, and 5 MPa respectively. Table 3.1 shows the specimen dimensions, loads and associated stresses for the specimens tested in this investigation. The three specimens tested by Beeby and Scott are also shown in order to allow comparison of the reinforcement ratios and steel stresses. The reinforcement ratio and steel stresses in the H25 and H40 specimens were equivalent to the previous T16 tests while the H32 and H50 specimens were linked to the previous T20 tests.

Bar Type	Prism Dimensions [mm]	Reinf. Ratio	Load Stage	Load [kN]	Steel Stress [MPa]
T12*	120×120×1200	0.79 %	1	43	381
			2	58	513
T16*	120×120×1200	1.42 %	1	43	214
			2	58	289
			3	72	358
T20*	120×120×1200	2.23 %	1	43	137
			2	58	185
			3	72	229
H25	190×190×2000	1.38 %	1	108	220
			2	144	293
			3	181	369
H32	190×190×2000	2.28 %	1	108	134
			2	144	179
			3	181	225
H40	300×300×2000	1.42 %	1	270	215
			2	360	286
			3	450	358
H50	300×300×2000	2.31 %	1	270	138
			2	360	183
			3	450	229

*Specimens tested by Scott and Beeby [4, 3]

Table 3.1: Specimen details for this investigation as well as previous investigations.

3.3 Concrete and Casting

For this testing program a target concrete compressive cube strength of 30 MPa was used. This allowed comparisons between the low strength concrete specimens from previous investigations. Table 3.2 shows the typical mix proportions by percentage weight. The aggregates were stored outside, and were thus often wet. Due to oven facilities being insufficient for the volumes of aggregate required the experience and skill of the technical staff was relied upon to achieve the correct water/cement ratio. In order to determine the required weights of each material the volume of concrete required was calculated, taking into account 6 cubes and 4 cylinders for strength testing. This was then multiplied by a density of 2400 kg/m^3 to determine the total weight of concrete required. Depending on the total mix size between 3% and 7% was added in order to account for small losses. The proportions in Table 3.2 were then used to determine the weights of each component required.

Material	Proportion of Weight
20 mm Aggregate	32.1 %
10 mm Aggregate	23.3 %
Sand	27.5 %
Cement	10.7 %
Water	6.5 %

Table 3.2: Typical concrete mix proportions by percentage weight.

Due to the maximum weight limitation of the concrete mixer each casting took place as a series of mixes. The smaller 190 × 190 prisms required 2 mixes while the larger 300 × 300 prisms required 3 mixes. In order to avoid strength inconsistencies the mixes were distributed along the entire prism. If each mix were to be used for a single area the concrete strength could vary along the prism. Mixes were performed directly after each other in order to avoid cold joins. The full casting procedure for each specimen was completed in under two hours.

As stated two sizes of prism were used in this investigation. Both were cast in the same 300 × 300 formwork, shown in Figure 3.1. In the case of the 190 × 190 prisms boards and wooden spacers were used to reduce the dimensions of the formwork. Stud bolts in combination with spacers were used to keep the formwork together during casting and provided a straight forward method for removal during curing. Prior to casting a thin layer of releasing agent was applied to the concrete contact areas of the formwork to aid its removal. The reinforcing bar was fed through appropriately sized holes in the formwork end boards and fixed in position using jubilee clips. Any remaining gaps after final tightening were filled with a high plasticity clay to limit grout loss during the vibration process.

During casting a vibrating rod was used in order to compact the concrete and minimise the amount of air voids present within the concrete mixture. This also ensured

Figure 3.1: Photograph of 300 × 300 formwork with H50 bar in position ready for casting.

that the concrete was in contact with the reinforcing steel along its entire length and circumference resulting in a more stable bond characteristic. The cubes and cylinders were vibrated using a vibration table. Once set the prism was covered in wet hessian and plastic sheets to enhance the curing process. After 3 days the sides of the formwork, as well as the moulds for the cubes and cylinders, were removed. The specimen was only removed from the formwork base after between 2 and 3 weeks depending on its size to avoid any cracks forming during the lifting process.

3.4 Experimental Apparatus

3.4.1 Tension Testing Rig

In order to apply load to the test specimens use was made of a mechanical loading rig based on a lever arm system to magnify the applied load. The rig used here is similar to those used in the previous investigations [37] but redesigned for use with larger specimens with large bar diameters and higher load levels. A photograph of the rig is shown in Figure 3.2. A mechanical loading system was chosen over hydraulic loading due to the necessity for steady long term loading. Hydraulic systems are subject to pressure losses over long periods of time and are not able to be operated with sufficient consistency for this investigation.

The ends of the reinforcing bars were held in the rig and loaded using a combination of steel collets and wedges. In the case of the H32, H40 and H50 specimens the ribs were machined down in order for the specimens to fit the collets. During installation sufficient space was left for the wires from the internally strain gauged bar to exit the ends of the bar towards the data logger. Figure 3.3 shows a photograph of a pair of collets with associated wedges.

In order to apply the maximum load of 450 kN the rig makes use of a double lever

Figure 3.2: Photograph of the tension testing rig with H50 specimen under load.

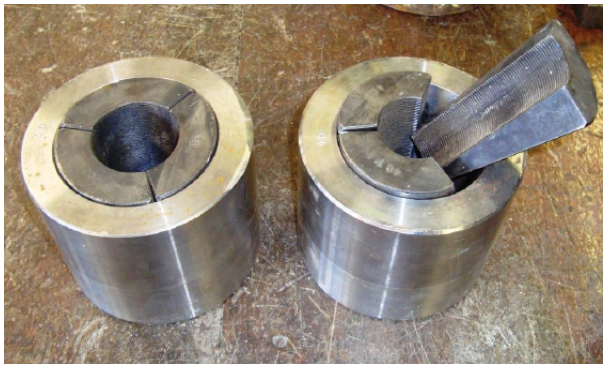

Figure 3.3: Photograph of a pair of collets with wedges.

arm system. Figure 3.4 shows a side view drawing of the rig used. The top lever arm is a class 1 lever arm and results in a magnification ratio of $3:1$. The lower lever arm is a class 2 lever arm and has a magnification ratio of $6\frac{2}{3}:1$. The overall magnification ratio of the rig is approximately 20:1. Each 20 kg weight thus applied approximately 4 kN of force on the specimen. Due to the rotation of the lever arms during the loading process the ratio of the weights to applied load changed throughout the test. For this reason a load cell was fitted between the upper collet and the top lever arm to provide an accurate reading of the applied load. This reading was taken by the same data logger used for the measurement of the strains within the gauged reinforcing bars. A counter weight was used for balancing the lever arms prior to loading. In this way only the dedicated loading weights resulted in load being applied to the specimen. This is particularly important in the unloaded stages when the specimen remained in the rig,

but no load was allowed to be present.

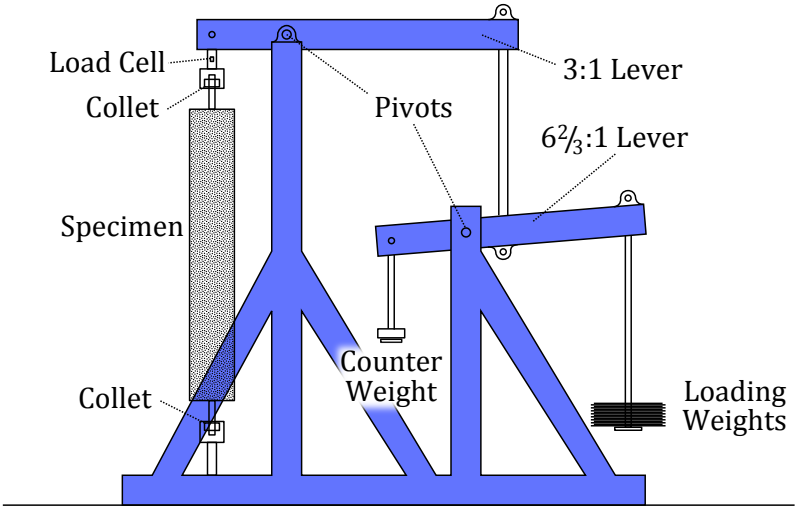

Figure 3.4: The tension testing rig used for testing large diameter bars (not to scale).

3.5 Data Collection

3.5.1 Internal Bar Strains

A large proportion of the experimental strain data collected in this investigation originates from a set of internally gauged deformed reinforcing bars. These were manufactured specifically for use in this investigation. A number of previous investigations [39, 51, 15] have made effective use of this method. In the past, however, these have been limited to a diameter of 25 mm. This investigation made use of significantly larger bars.

Two gauges were placed at 250 mm from the bar end to provide an indication of pure steel strains. The remaining 81 gauges were placed at 15 mm intervals along the central 1.2 metres of the specimen. Figure 3.6 shows the layout of the electronic strain gauges along a bar. The central gauges were staggered along the bar to aid in the detection of bending and provide a more effective use of the space available.

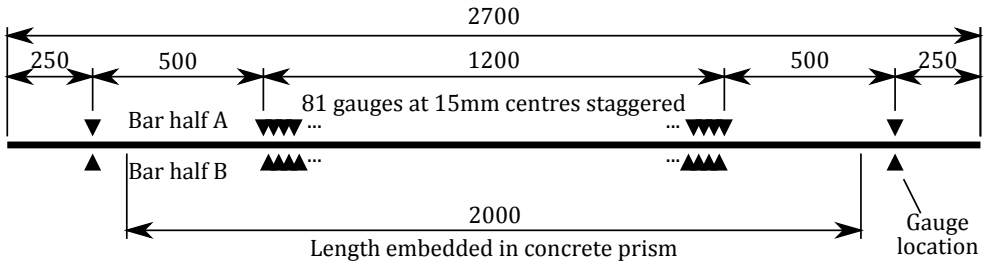

Figure 3.5: Layout of electronic strain gauges along the reinforcing bars (lengths in mm).

For the creation of a single 2.7 metre specimen two bars of approximately 3 metres in length were machined down by exactly half their diameter. Although this is costly it is significantly more accurate and controlled than cutting a single bar through its centroid. In the case of using a single bar, as the Mains method [15] did, there would always be an amount of material lost in the cutting process, which is avoided by machining down two individual bars. A duct was machined down the centre of the specimen 4 mm in width and 2 mm deep to accommodate the strain gauges as well as the associated wires. The loss in cross-sectional area due to this duct is thus 16 mm^2, which was taken into account during data processing and calculation. The proportion of cross-sectional area lost ranges from 3.3% to 0.8% for a H25 bar to H50 bar respectively. Figure 3.6 shows a schematic cross-section of a gauged reinforcing bar.

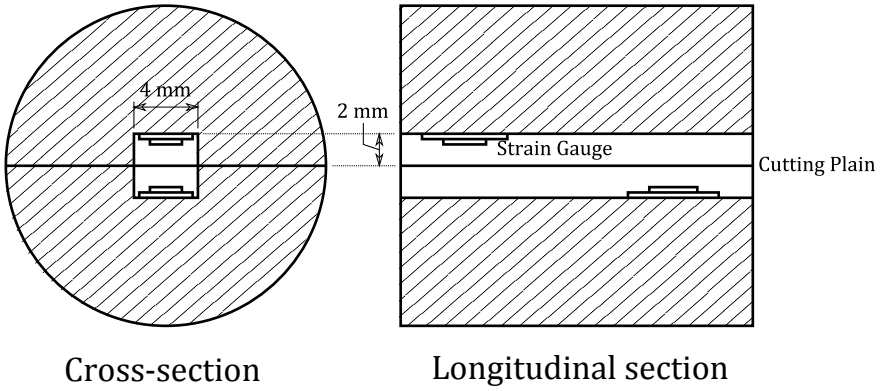

Figure 3.6: Sections of a gauged reinforcing bar (not to scale).

The gauges were bonded to the bar using a cyanoacrylate adhesive. Once the adhesive had hardened a set of three copper wires were soldered onto the contacts of each gauge. One contact was fitted with a single wire, while the other was fitted with two. This allowed the gauges to function as quarter bridges in combination with a dummy gauge. This layout is described in more detail in Section 3.5.3. The wires exited the bar at both ends via the machined duct. In this way the surface of the bar was affected as little as possible in order to preserve the steel-concrete bonding properties. Figure 3.7 shows a photograph of a section of a gauged and wired half bar. At this stage, once all electrical connections had been checked, the two half bars were joined together using a two component epoxy adhesive. Once hardened any spare adhesive was scraped off the steel, once again to preserve the bonding properties. Finally the wires were wrapped in self amalgamating tape for protection during transport and casting.

3.5.2 Average Surface Strains

In order to measure the strains present on the surface of the concrete prisms Demec studs were used in combination with a Demec strain measurement gauge. Before loading a number of studs are placed at regular intervals, in this case 200 mm, along the specimen. The Demec gauge allows the difference in distance between each set of studs

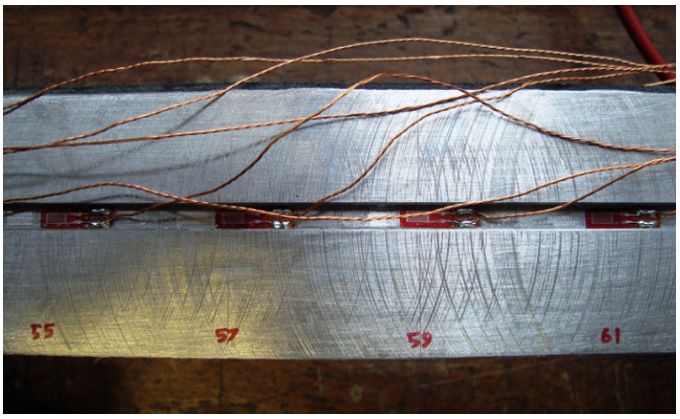

Figure 3.7: Photograph of a gauged and wired half bar (H40).

to be measured. An initial reading is taken before loading. This is then subtracted from each subsequent reading to determine the amount by which the distance between the studs has changed. The number of dial divisions by which this has changed is then multiplied by the gauge factor to provide the strain reading in microstrain. This proved a simple but effective method for the measurement of the average surface strains across the specimens. Figure 3.8 shows the layout of the Demec studs. Measurements were taken on two opposite sides of the prism. This allowed the detection of bending, as well as providing a representative sample for the calculation of average surface strain.

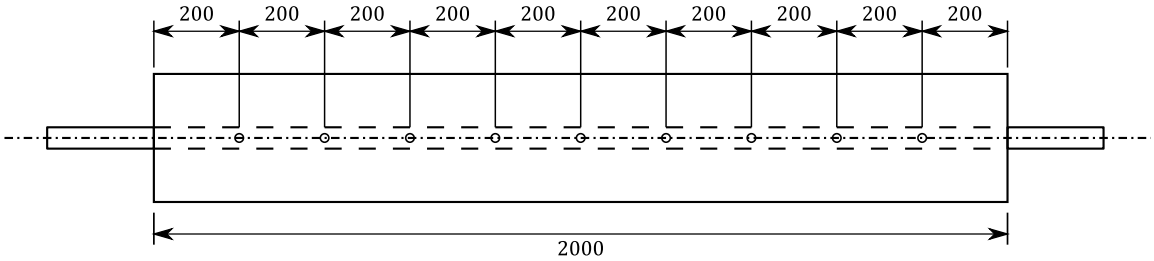

Figure 3.8: Position of DEMEC studs on surface of the concrete prism (lengths in mm).

3.5.3 Instrumentation

Due to the large amount of electronic strain gauges (85) present within each bar a digital data logger was used for the logging of the steel strains. The data logger used in this case was the *Spectra-node Data Acquisition and Control System*. This can not only read the gauges at a high rate, but also be set to take readings at constant intervals. This allowed a very high density of readings to be taken in the first hours after each load stage, the period in which the loss of tension stiffening was expected to be greatest. A schematic representation of the set-up is shown in Figure 3.9.

The wiring harness consists of a large number of 1 to 1 soldering connections providing a convenient method for connecting the gauge wires to the data logger cards. The data logger provides the energising current to allow the reading of the strain gauges

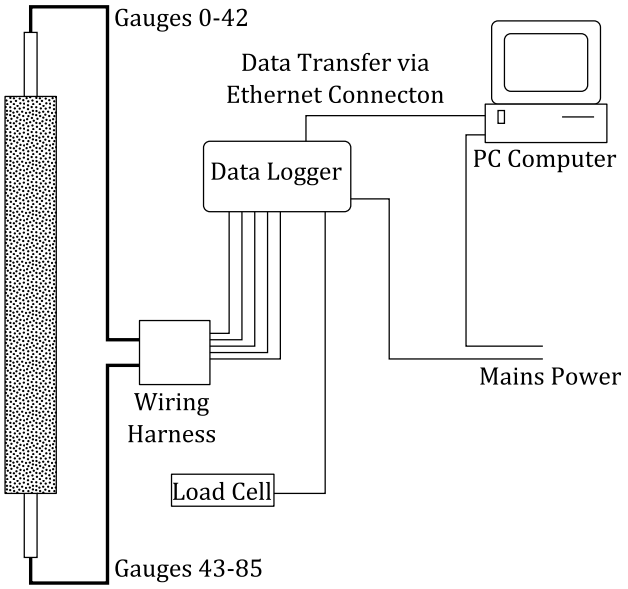

Figure 3.9: Schematic of instrumentation set-up for tension tests.

and transfers the measured data to a PC computer. The software on the computer then uses this data to compute the strains based on the gauge factors and resistances. The load cell was also read by the data logger and was calibrated to provide a reading in kN. This was achieved through a computed artificial gauge factor of -7.11 which took into account the loading bar cross-sectional area and elasticity. The load cell consisted of a half bridge set-up using six strain gauges while each internal bar gauge acts as a quarter bridge with a single gauge. Figure 3.10 shows the connections for each of these gauge set-ups. Every bar gauge was fitted with a pair of wires at one terminal. This was done to allow the resistance of the wires to be measured which results in a more accurate computation of the strains. In the case of the quarter bridge a single dummy gauge was mounted on the card to act as a reference for all connections on that card. This provided a cost effective method for increasing the accuracy of the readings.

3.5.4 Crack Recording

Crack recording was achieved via visual inspections and monitoring of the internal reinforcement strains. Before loading commenced the specimen was painted white in order to make cracks more obvious. Once detected, the cracks were marked using a marker pen and the load was noted at each end. In order to distinguish between the various cracks they were numbered in order of their occurrence. The crack ends were marked with a perpendicular line. As a crack progressed this was marked and the new load was noted at the new ending point. If the load had not changed the number of days the load had been applied was noted. In this way the progression of the crack was clearly recorded. After each test each side of the specimen was photographed and converted into a cracking diagram to provide a record of the cracking history. This

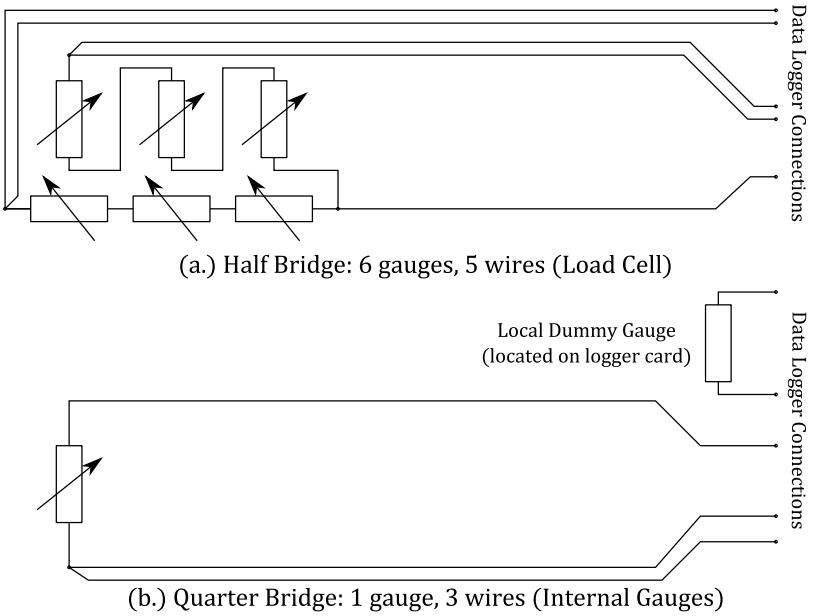

Figure 3.10: Schematic of gauge wiring and data logger connections.

was particularly useful for the geometrical definitions of the finite element model, and justification for the internal strain measurements. Figure 3.11 shows an example of this type of crack recording.

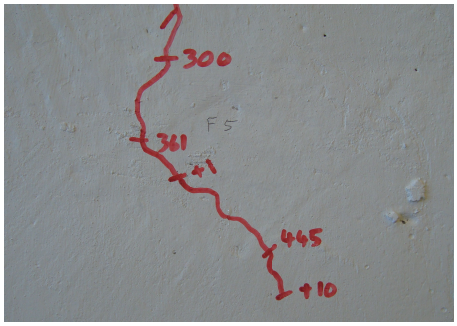

Figure 3.11: Recording of crack propagation.

3.6 Experimental Procedure

The experimental procedure consisted of the application of three loading stages followed by a final zero load stage. After each load stage was applied the specimen was monitored until the strains within the specimen had stabilised. A flow chart representing the experimental procedure is shown in Figure 3.12. Stabilisation often occurred within 1 week resulting in loading stages being held for between 8 and 14 days depending on weekends and other lab activities.

As the flow chart in Figure 3.12 shows, after loading was completed the data logger was set to scan at intervals. The length of these intervals differed according to how long

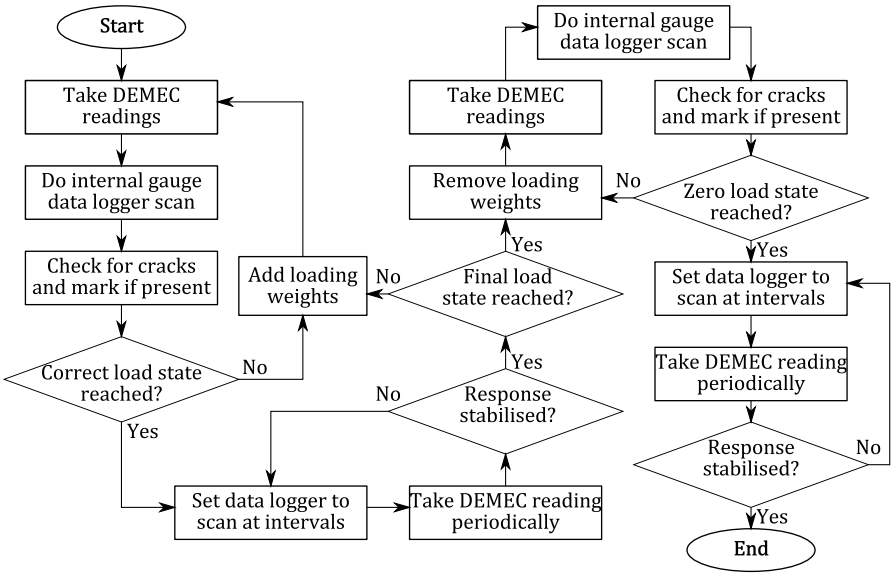

Figure 3.12: Flow chart showing the experimental procedure followed.

the load stage had been applied. For the first 4 hours a scan frequency of 5 minutes was maintained while during the next 4 days a frequency of 30 minutes was used. After this a frequency of 60 minutes was used until the next load stage was applied. During loading a scan was done after each 20kg weight was placed (equivalent to a load step of 4 kN).

Demec readings were taken every morning and evening during the first 4 days of the response, after which readings were taken every morning. Due to the high rate of stabilisation it was not deemed necessary to take readings during weekends. During loading readings were taken just before loading commenced and at intervals of approximately 10 to 20 kN of applied load depending on the target load. Additionally, readings were also taken immediately after crack formation. The combination of internal strain measurement and surface strain measurement provided a comprehensive set of data. This, in combination with marking of cracks and noting of any additional observations, enabled a complete record of the specimen response to be compiled.

Chapter 4

Experimental Results and Discussion

Each of the test specimens was successfully loaded and the response documented. Due to a delay in the manufacturing process the specimens were tested in the following order: H32, H40, H50, H25. The three load stages, as shown in Table 3.1, were applied to each specimen except for the H25 specimen. Due to high peak strains at crack locations the third load stage was not applied in order to avoid yielding of the reinforcing steel. This decision was taken after yielding was detected during the third load stage of the H40 specimen. Analysis of the results showed that this small amount of yield did not affect the member response with respect to time dependent cracking or tension stiffening decay.

4.1 Specimen Properties

As the results from the various specimens were being compared and related to previous results knowledge of the concrete properties was important. A pair of basic strength tests were conducted for each specimen in order to determine the concrete quality, and allow estimation of the Young's modulus for concrete. These were the cube compression test and the cylinder splitting test. The cube test provided a direct indication of the compressive strength of the concrete while the results from the cylinder test were used with Equation 4.1 to determine the concrete tensile strength [52].

$$f_t = \frac{2P}{\pi D_c L_c} \tag{4.1}$$

where:

f_t = indirect tensile strength
P = load at splitting
D_c = diameter of the cylinder (150mm)
L_c = length of the test cylinder (300mm)

Three cube tests and two cylinder tests were performed just before loading commenced as well as just after the end of the testing period. This provided an indication of the stability of the concrete strength throughout the testing period. The average strengths from these tests for each specimen are shown in Table 4.1.

		Specimen			
		H25	H32	H40	H50
Concrete Age at Start	[days]	32	32	32	34
Compressive Cube Strength (f_{cu})	[MPa]	31.0	26.2	41.8	33.5
Indirect Tensile Strength (f_t)	[MPa]	2.56	1.87	2.81	2.47

Table 4.1: Strength testing results for each specimen.

The H32 specimen showed a surprisingly low cube and indirect tensile strength. This was determined to be due to the aggregates being wet before casting. The resulting water/cement ratio for this specimen was significantly higher than for other specimens.

Figure 4.1 shows photographs of the four reinforcing bars used in the specimens. Although from the same supplier, the rib patterns and heights differed significantly between the different diameter bars. This prompted the investigation of how this affects the bond strengths and cracking behaviour. This is discussed in more detail in Section 4.5.

(a) H25

(b) H32

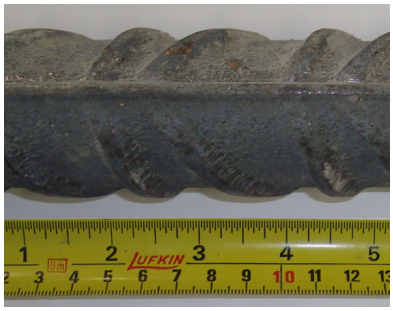

(c) H40

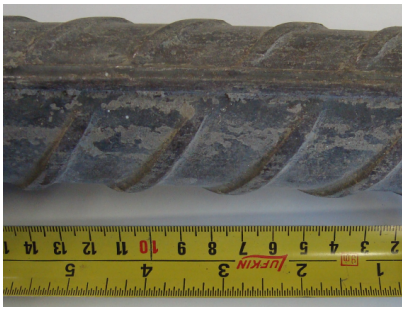

(d) H50

Figure 4.1: Photographs of the four reinforcing bars used in the testing program.

4.2 Load Response

Figure 4.2 shows a typical plot of reinforcement strain along the length of the gauged section of the reinforcing bar for a number of loads with an associated number of cracks. Where cracks formed the concrete was no longer able to carry tensile stress. This stress is transferred to the reinforcement resulting in the measured peaks of strain. This plot can be compared with the cracks on the crack diagram in Appendix A for the H32 specimen. The vertical dashed lines coincide with those on the crack diagrams. The sawtooth effect, which is most prominent at crack locations is a result of local bending. As the gauges are staggered along the length of the bar one side will record greater strain levels than the other when there is bending present. This is further investigated in Section 4.6.

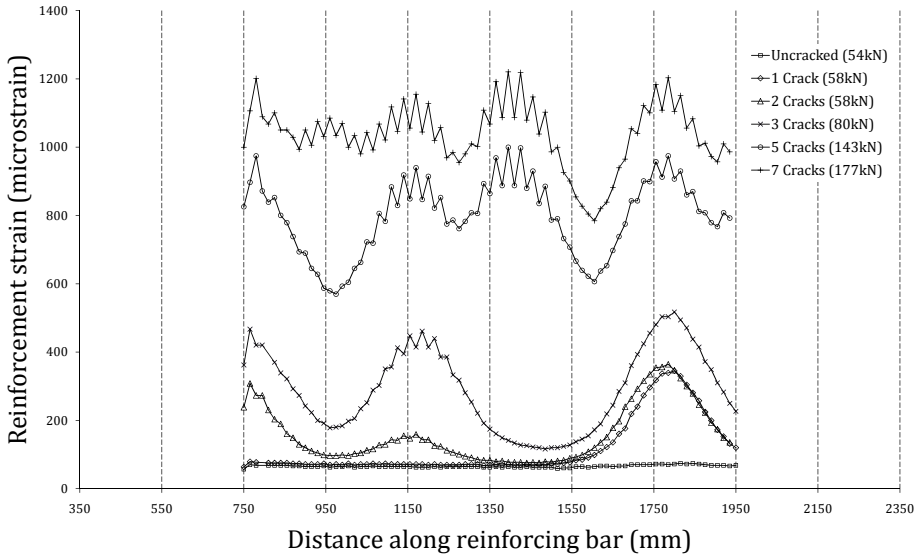

Figure 4.2: Plot of reinforcing strains in H32 specimen at a load of 80 kN.

In order to aid interpretation of the bar strains these were plotted as a three dimensional surface. This allowed the strain variation along the bar to be plotted against load. As an example the H32 results have been plotted in Figure 4.3. It is clear that the cracking of the specimen behaves according to the mechanism described by Beeby [27] up to the second load stage. After the formation of the fifth crack the transfer zones cover the entire length of the specimen. As described in Section 2.2 no further primary cracks can form at this point. Comparison of Figure 4.3 with the crack diagram in Appendix A for the H32 specimen provides a clear record of the cracking mechanisms present in this specimen.

Cracks 6 and 7 have been able to form within the transfer zones either as secondary cracks, which have propagated to the surface, or as late primary cracks. These are caused by the concrete stress peaks (as shown in Figure 2.5(d)) exceeding the concrete tensile strength at high load levels. The concrete stress, calculated from the bar strains

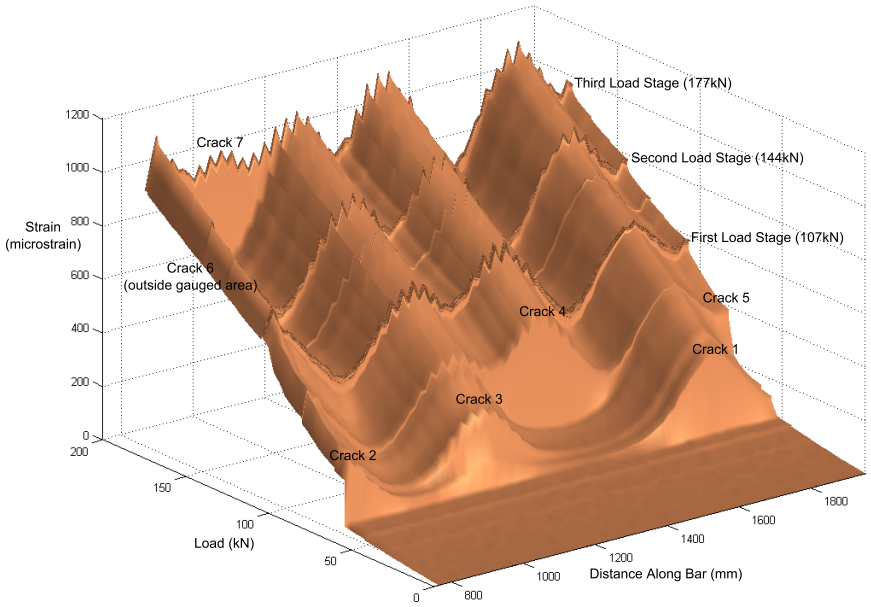

Figure 4.3: Surface plot of bar strains in H32 specimen along the bar against load.

and applied load, at the location of Crack 7 just before cracking was 1.99 MPa. This exceeds the tensile strength calculated from the cylinder tests, 1.87 MPa, and it is thus safe to assume that this is a late primary crack.

There is one unusual observation which can be made from Figure 4.3. All cracking in previous testing has resulted in instantaneous local increases in bar strain. Crack 3, however, shows a steady increase in strain between 57 kN and 70 kN. Finite element analysis has shown that a likely explanation is that an internal crack formed which swiftly propagated to the surface as load was increased. This special case and the associated finite element analysis is discussed in detail in Section 6.2.3.

Figure 4.4 shows the surface plots of strain distribution against load for the remaining three specimens. The basic cracking mechanism is similar for all the specimens. In the H40 specimen all three cracks occurred simultaneously while in the H25 and H50 specimen there was a significant delay between the formation of subsequent cracks. Cracks will naturally form at the location where the local concrete tensile strength is lowest. This instantaneous formation of all three cracks indicates that the concrete tensile strength was more uniform in the H40 specimen than in other specimens.

It is clear from the surface plots that the transfer lengths for each specimen differed significantly which affected the number of cracks which formed in each specimen. This observation is related to the bond strength between the reinforcement and the surrounding concrete and is investigated in detail in Section 4.5.

The average bar strains in the reinforcement were plotted against the load for each

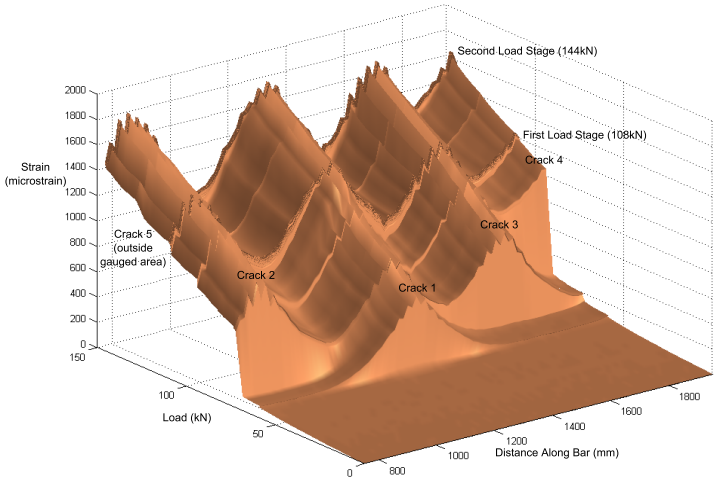

(a) H25

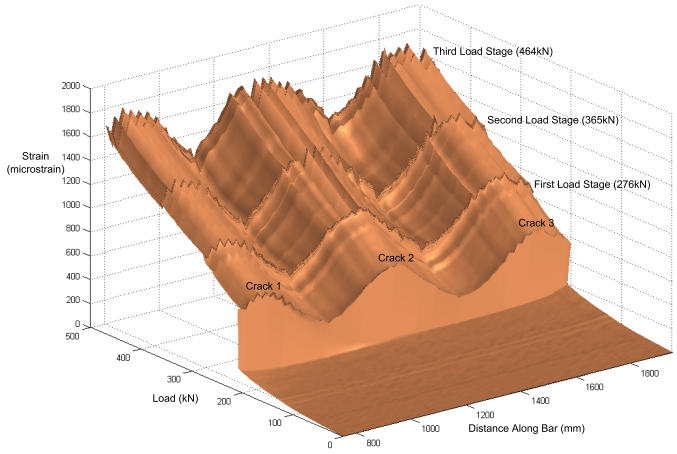

(b) H40

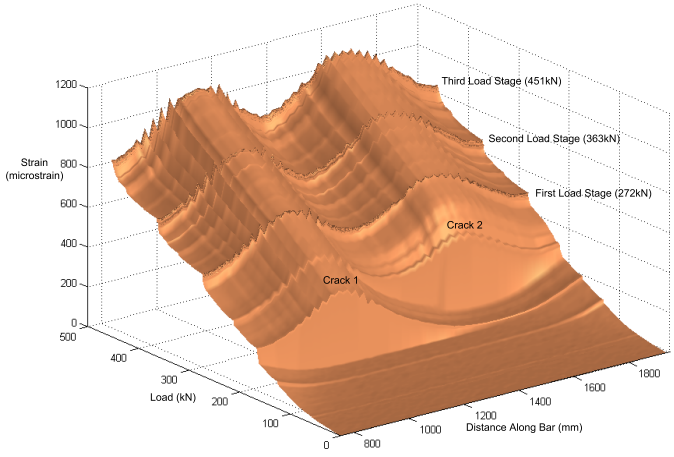

(c) H50

Figure 4.4: Surface plot of bar strains in specimens along the bar against load.

specimen as shown in Figure 4.5. These plots can be compared to Figure 2.3 in Section 2.1.3. As can be seen each occurrence of a crack resulted in a horizontal discontinuity on the load against bar strain plot. At these points in time there was an instantaneous increase in average bar stress while the load remained constant. This is a direct result of the loss of stress in the concrete at the crack location. This stress is transferred to the steel resulting in the measured strain increase. When multiple cracks occurred simultaneously, such as in the H40 specimen, see Figure 4.4(b), this resulted in a single discontinuity.

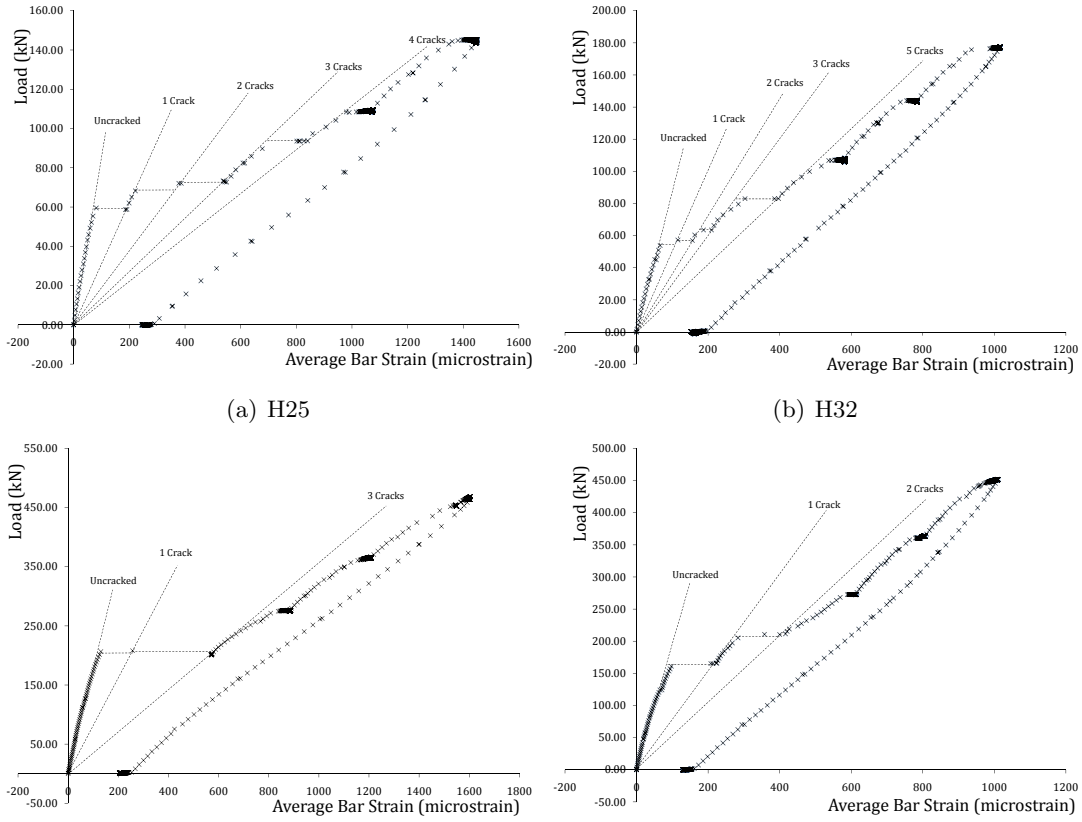

(a) H25

(b) H32

(c) H40

(d) H50

Figure 4.5: Plots of average bar strains in specimens against load.

The constant load stages can be identified as the small horizontal zones with high data density. This small increase in strain over time is due to a combination of tension stiffening decay and creep. The unloading response after the final load stage is also shown. In each case the final zero load stage results in a measurement of residual strain in the specimen. This residual strain is the result of the total creep which occurred during the experiment and cracks not fully closing. This residual strain was found to be greater for the two specimens with high stress levels (H25 and H40) which indicates the possibility of a limited amount of yield having occurred.

4.3 Lateral Cracks

Each of the large diameter tests has resulted in a number of lateral cracks forming perpendicular to the primary cracks. These have been recorded on the crack diagrams in Appendix A. Particularly the H40 specimen showed significant lateral cracking with a maximum distance of 200 mm in the direction perpendicular to the primary crack. A number of lateral cracks also formed at the prism ends. This result was unexpected as the previous small diameter tests showed almost no lateral cracking.

The most plausible explanation for the occurrence of these cracks is the wedging effect of the reinforcing ribs. In comparison with the smaller diameters from the previous investigation the rib heights were significantly greater in this investigation. The H50 specimen was an exception, however. The crack diagram for the H50 specimen shows that there were very few lateral cracks present in this specimen after loading. This supports the theory that there is a relation between rib height and the degree of lateral cracking, although further investigation is required to confirm this.

The presence of lateral cracks indicates that there is a significant zone of de-bonding present adjacent to each crack. This is supported by the constant high stress which is present in the reinforcement at crack locations as can be seen on the strain distributions.

4.4 Transfer Lengths

As described in Section 2.2, Beeby and Scott [39] developed a method for the estimation of the average section strain using the transfer length and average crack spacing. Equation 2.2 shows this relation. For the tests performed in this investigation the transfer lengths were measured for the first few primary cracks. It was not possible to measure the transfer length for later cracks as interference occured between the cracks. The final crack pattern was used to obtain the average crack spacing. The ends of the prism were treated as primary cracks. Because in each case the average crack spacing S_{rm} was less than twice the transfer length S_0, the second part of Equation 2.2 was used, shown here as Equation 4.2. The final load stage was used to calculate the reinforcement strain ε_{s2} as the average crack spacing was based on the final crack pattern. Table 4.2 shows the measured variables for each specimen and the result provided by Equation 4.2. The calculated average strain estimate is compared to the actual average bar strains measured in each specimen.

$$\varepsilon_{av} = \frac{\varepsilon_{s2}(1 + \alpha_e\rho - S_{rm}/(4S_0))}{1 + \alpha_e\rho} \tag{4.2}$$

It is clear that Equation 4.2 provides a good estimate for the average strain in a tension member. This method does, however, appear to provide an underestimate in each case. It should also be noted that the measurement of the transfer length is

		Specimen			
		H25	H32	H40	H50
Reinforcement ratio ρ		0.013	0.022	0.014	0.022
Modular ratio α_e		9.52	9.29	8.00	9.29
Pure bar strain ε_{s2}	$[10^{-6}]$	1529	1125	1472	1159
Transfer length S_0	[mm]	352.5	285	450	620
Ave. crack spacing S_{rm}	[mm]	400.0	347.9	491.3	666.7
Calculated ave. strain ε_{av}	$[10^{-6}]$	1144	840.9	1110	900.5
Measured ave. strain	$[10^{-6}]$	1449	1016	1208	1008
Error		21.0%	17.2 %	8.1 %	10.7 %

Table 4.2: Strain estimates using transfer length and crack spacing.

extremely subjective as there is no one definite point at which the transfer of stresses starts. The transfer length can also be related to the bond strength of the interface between the concrete and the reinforcement and hence the rib pattern.

4.5 Bond Strength

The H50 specimen produced a surprisingly small number of cracks. Only two cracks formed in the entire two metre concrete section. Although a small increase in transfer length was expected as the reinforcement diameter increased, the recorded lengths were significantly above any reasonable estimates. A visual comparison of the H50 bar to the other smaller reinforcing bars revealed that the surface of the H50 bar was significantly less rough and had smaller relative rib dimensions. This can be seen in the bar photographs in Figure 4.1. This indicates that a lower bond strength between the concrete and the reinforcing steel could have been the source of this sparse cracking pattern.

The bond strength can be calculated using the gradient of the bar strains in the vicinity of a crack [7]. This is shown in Equation 4.3.

$$\sigma_b = \frac{\delta\sigma}{\delta l}\frac{D_b}{4} \tag{4.3}$$

where:

σ_b = bond stress

$\frac{\delta\sigma}{\delta l}$ = gradient of the stress distribution along the bar

D_b = bar diameter

The gradient of the strain distribution ($\delta\varepsilon/\delta l$) can be found using the linear sections of the distribution adjacent to cracks. This can then be multiplied by the elastic modulus of steel (E_s) to provide the change in stress along the bar ($\delta\sigma/\delta l$). Figure 4.6 shows an example of a strain distribution for the H40 specimen and one of the gradients

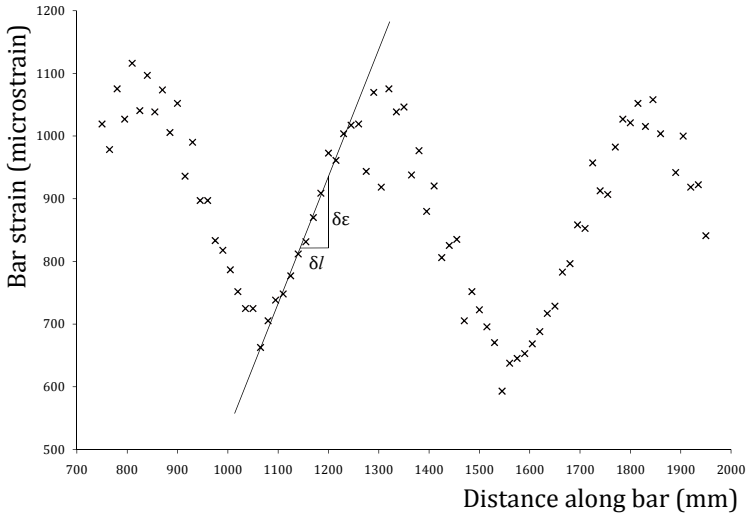

Figure 4.6: Example of a gradient of strain distribution used for bond stress calculation using the first load stage (107 kN) of the H40 specimen.

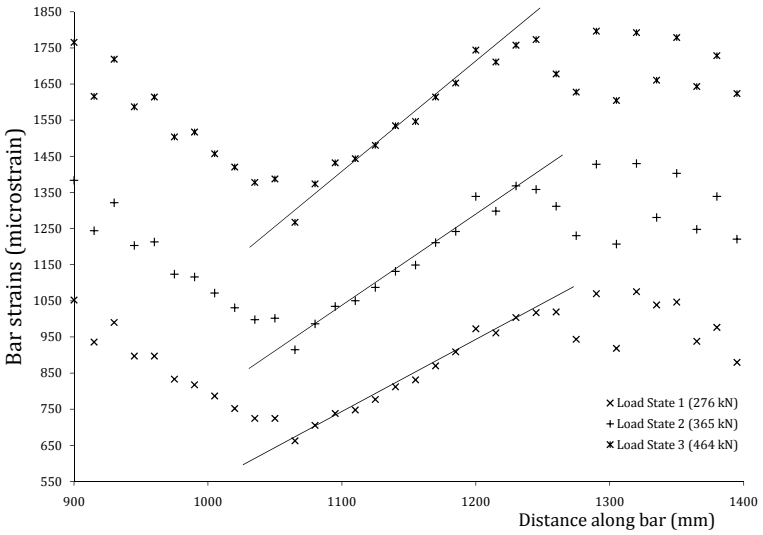

Figure 4.7: Detail of strain distribution at each load stage for the H40 specimen.

used for the calculation of bond strength.

The constant bond strength along the zones adjacent to a crack could indicate that bond strength has reached a maximum and is behaving plastically. This is not the case, however, as the bond stresses increase when the load on the specimen is increased. This is observed as an increase in the gradient of the strain distribution. This same effect was observed by Scott and Gill [34]. An example of this is shown in Figure 4.7 for the H40 test. The calculated average bond stresses for each specimen are tabulated in Table 4.3.

If the bond behaviour is elastic the increase in bond stress should be proportional

	Bond Stresses [MPa]			
	H25	H32	H40	H50
Loading Stage 1	4.84	2.95	3.98	1.98
Loading Stage 2	6.16	3.55	4.60	2.35
Loading Stage 3	-	4.08	5.02	2.64

Table 4.3: Calculated bond stresses.

to the increase in loading. This can be confirmed by plotting bond stress against load for each specimen using the various load stages. These plots are shown in Figure 4.8 for each of the specimens tested in this investigation.

The bond stress plots indicate that the concrete steel interface is acting elastically, although the H40 specimen does show some slight deviation from the purely elastic response. It was observed that the constant strain gradient is not present along the entire bar length. Figure 4.7 shows that around a crack, in this case at 1310 mm from the bar end for example, there was a decrease in strain gradient and thus bond stress. This implies that the bond was not behaving elastically. Figure 4.7 shows that this damage zone around the crack increased in length as loading increased. Directly

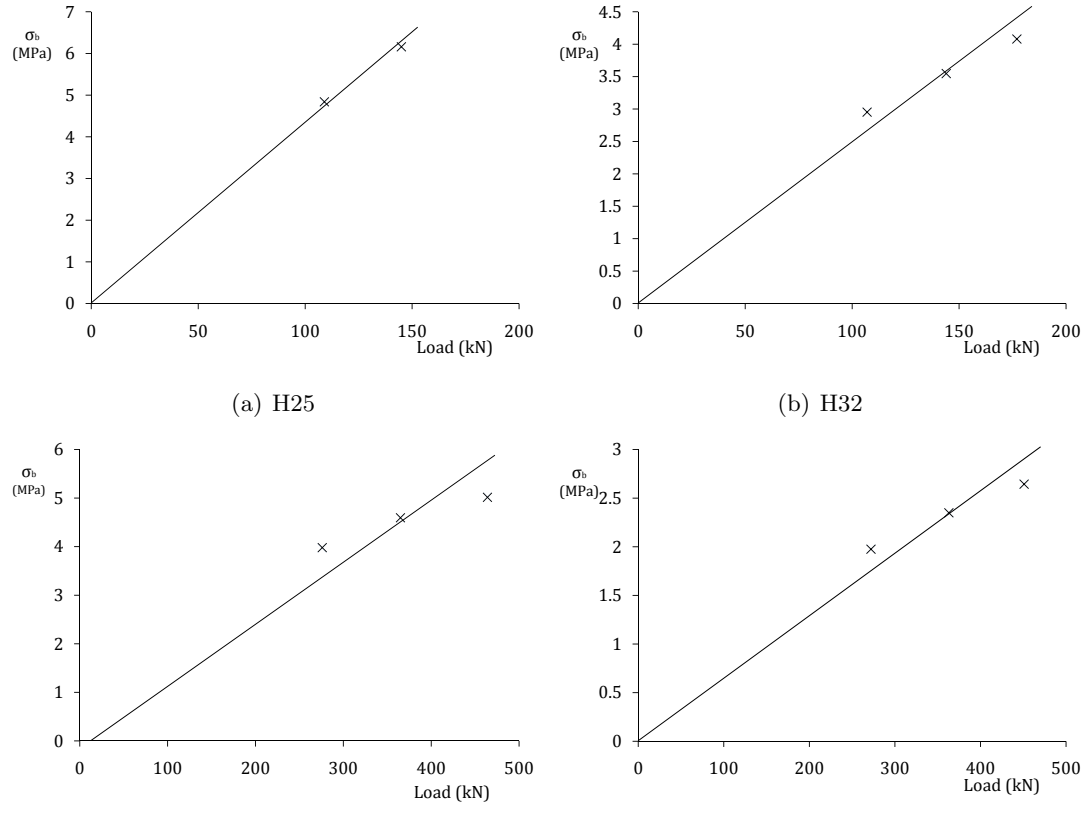

(a) H25

(b) H32

(c) H40

(d) H50

Figure 4.8: Bond stresses at each load stage for the investigated specimens.

adjacent to the crack the strain distribution can be considered constant, indicating no bond stress. Where this is the case at high tensile stresses this indicates the bond between the concrete and the reinforcement was fully degraded and slip was possible.

The response of bond stress over time under sustained loading was observed to be mostly constant. At approximately a quarter of the crack locations very slight decreases in the strain distribution gradient were observed indicating a decrease in bond stress. The total decrease measured was generally no more than 5% and in each case remained well within the variance in measured bond stresses for a single load stage. A possible explanation for a decrease in bond stress is that as the stresses in the steel increase during the loss of tension stiffening, as is described in detail in Section 4.7, less stress is transferred between the concrete and the steel. The fact that this effect did not occur consistently and the relative variances in bond strength limits the definition of a trend. Further investigation under longer sustained loading would be required before any conclusions can be drawn regarding the response of bond stress over time.

Table 4.3 shows that the H50 specimen did indeed show significantly lower bond strengths. Comparison with the rib pattern photographs in Figure 4.1 indicates that the more severe rib patterns result in a higher bond stress. This explains the low number of cracks which occurred in the H50 test and the associated long transfer lengths. Comparison with results from an experimental comparison between plain and deformed bars in tension specimens by Sawada [53] in 2004 shows that the H50 specimen was still following a typical deformed bar response. Plain bars showed a constant bond strength under varying load levels, which is not the case here. Although the low bond strength was not desirable this appears not to have affected the member response significantly.

4.6 Bending

The saw tooth effect which is most clear on the peak of the centre crack in Figure 4.2 occurred due to bending in the reinforcement. As the strain gauges were staggered across the channel, as shown in Figure 3.6, the presence of bending will result in the gauges on one side providing higher readings than those on the other. This phenomenon was particularly large at higher levels of loading. There are two possible sources for this bending. The bar may have not been perfectly straight during casting either due to bending under self weight, in the case of smaller diameters, or simply faulty manufacturing. For example, smaller diameter bars are often stored as coils and straightened before use which can result in slight deformations. Where this is the case loading the specimen causes the bar to straighten, significantly affecting the surface strains. Alternatively, if a crack has not propagated around the full circumference of the specimen this can cause local bending at a crack as shown in Figure 4.9. In order to fully understand the mechanisms acting in a specimen it is important to be able to determine the type and degree of bending.

The strains computed from the Demec gauge readings can provide an insight into

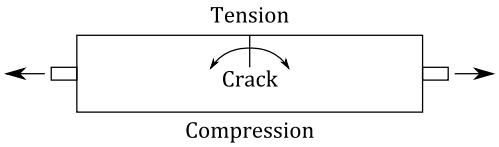

Figure 4.9: Local bending causing tension and compression in a tension member.

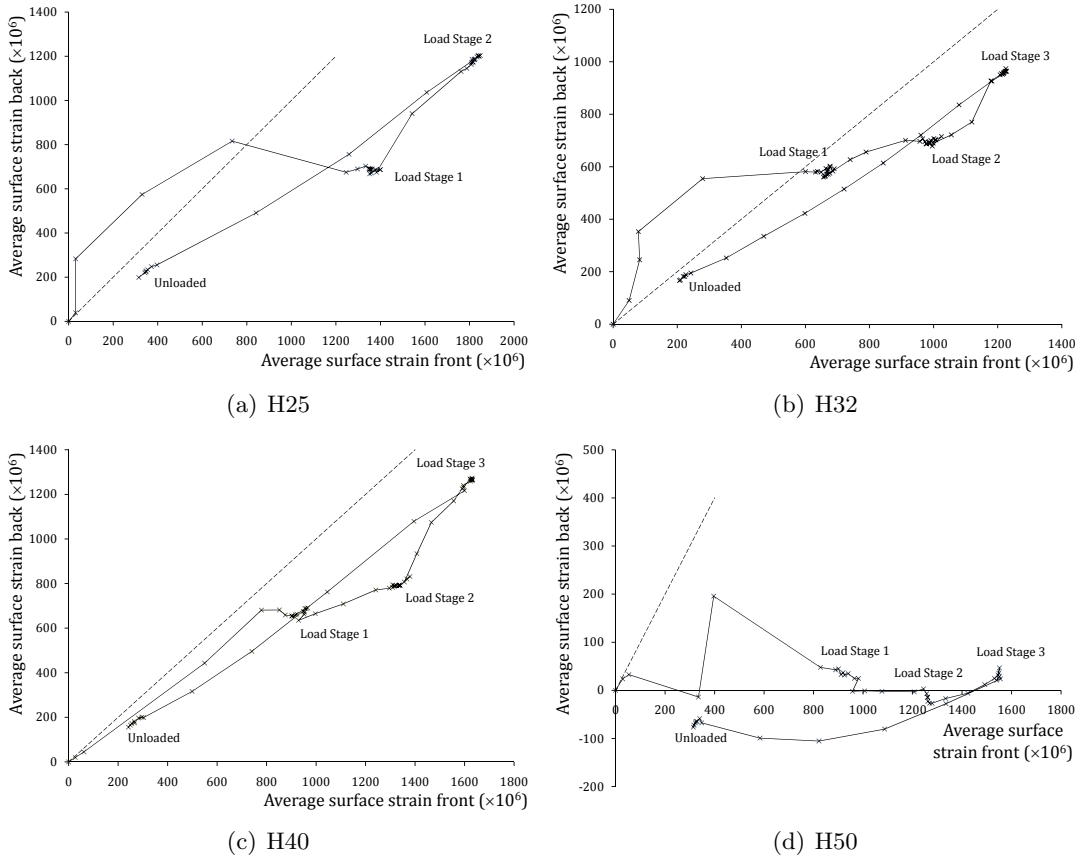

(a) H25

(b) H32

(c) H40

(d) H50

Figure 4.10: Comparison of front and back surface strains.

the bending history of a specimen during loading. The surface strains were computed using the gauge factor and averaged across the front and back of the specimen. These were then be plotted against each other, as shown in Figure 4.10. On each plot a line of gradient one is shown which reflects the ideal case where average surface strains on both sides of the prism are equal. If there was overall bending present, this is the case when local bending cases do not cancel each other out, this will be reflected as a significant deviation from this line. In earlier stages, when the first cracks form, it is expected that there is significant deviation. When the final cracking pattern is reached, however, this deviation should reduce to a limited amount.

As can be seen all specimens showed approximately linear responses except for the H50 specimen. The strains appeared only to increase on the front surface. This is in line with the observations made at the time with both cracks forming on the same side,

as shown on the crack diagram. Although at low load levels comparison with the crack diagram could provide an indication of the type of bending, at high load levels with a large number of cracks further data analysis was required.

A method for analysing the strain distribution for bending was developed. A typical example is presented in Figure 4.11 based on the final load stage (144 kN) of the H25 specimen. The final bending plots for the H32, H40 and H50 specimens are shown in Figure 4.12.

First a running average was calculated between each pair of readings as shown in Figure 4.11(a). The variation between this and the actual data points was then

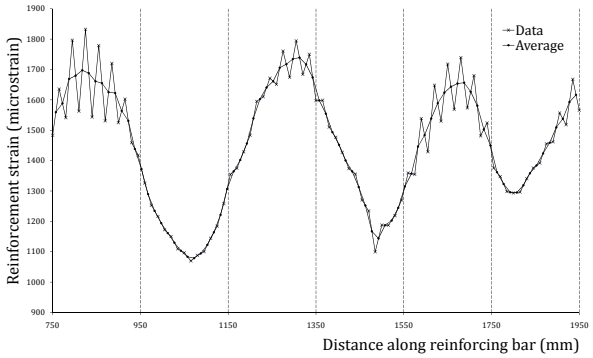

(a) Original data and average

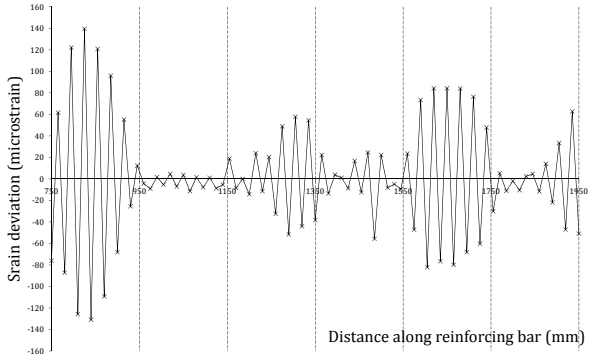

(b) Deviation from average

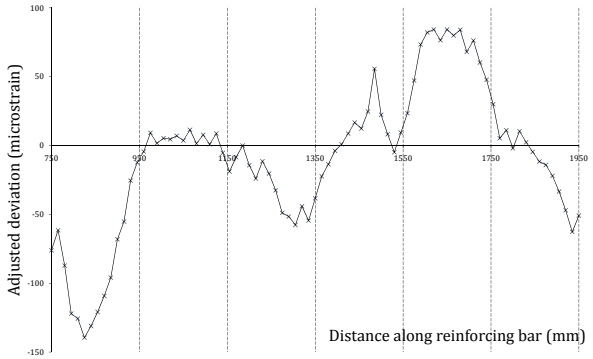

(c) Adjusted deviation

Figure 4.11: Bending analysis for H25 specimen at a load of 144 kN (final load stage).

calculated. This is shown in Figure 4.11(b). Finally the sign of every second value is changed in order to take into account the staggering of the strain gauges. When plotted, this results in a single line indicating which direction the prism was bending in, as shown in Figure 4.11(c). If this line remains constant and remains either positive or negative bending was continuous and present along the entire specimen. This would indicate that the bar was not straight during casting. If, on the other hand, the line crosses the horizontal axis in a number of locations there were various magnitudes and directions of bending present. This indicates that the source of bending is local and usually a direct result of cracking. In the case of the H25 specimen the bending was

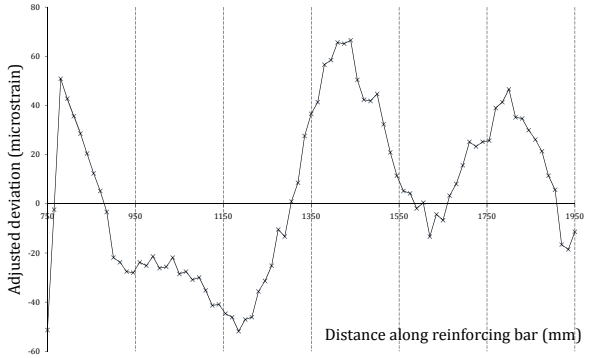

(a) H32

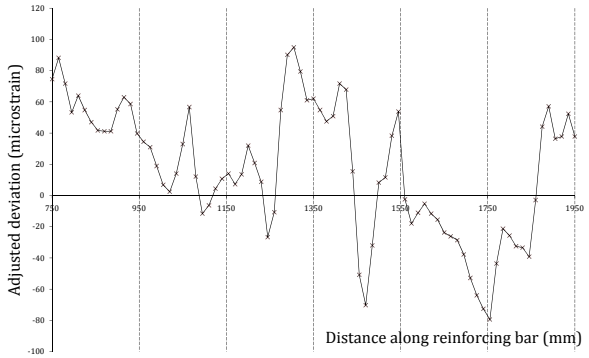

(b) H40

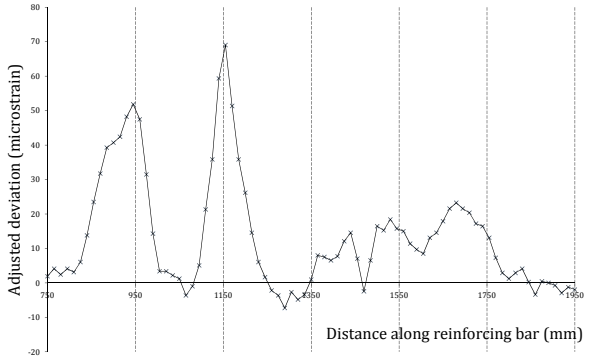

(c) H50

Figure 4.12: Bending analysis results for the remaining specimens.

local and in different directions and could hence be considered a result of cracking.

Figure 4.12(c) shows the adjusted deviation plot for the H50 specimen. In this case almost all deviations are positive, indicating that all bending in the specimen is such that there is tension on the front face, and compression on the back face. This is supported by the crack formation pattern. A possible explanation could be a slightly curved reinforcing bar. The plot, however, also shows that although all bending is in the same direction it is still local and not uniform along the specimen. If the bar was bent a more uniform response would be expected, with peaks at crack locations. Another possibility is that the concrete strength on the back half of the specimen was lower than the front. This could be due to a difference in compaction through vibration as the bottom (back) half of the specimen is less accessible. The rest of the tested specimens show local bending in various directions depending on which sides cracks formed as expected.

4.7 Tension Stiffening Decay

The main aim of this testing program was to determine the rate of decay of tension stiffening. This can be detected as an increase in bar stress, and hence strain, after the application of load while the load is held constant. As an example Figure 4.13 shows the average bar strain plotted over time for the H32 specimen. The origin represents the moment at which the first loading was initiated. A detailed plot of the bar strains over the first 24 hours after loading is shown in Figure 4.14. An increase in strain under sustained loading can be a result of a combination of creep and tension stiffening decay. The increase in bar strains shown in Figure 4.14, however, is too rapid to be attributed to creep and is thus a direct result of the loss of tension stiffness in the concrete.

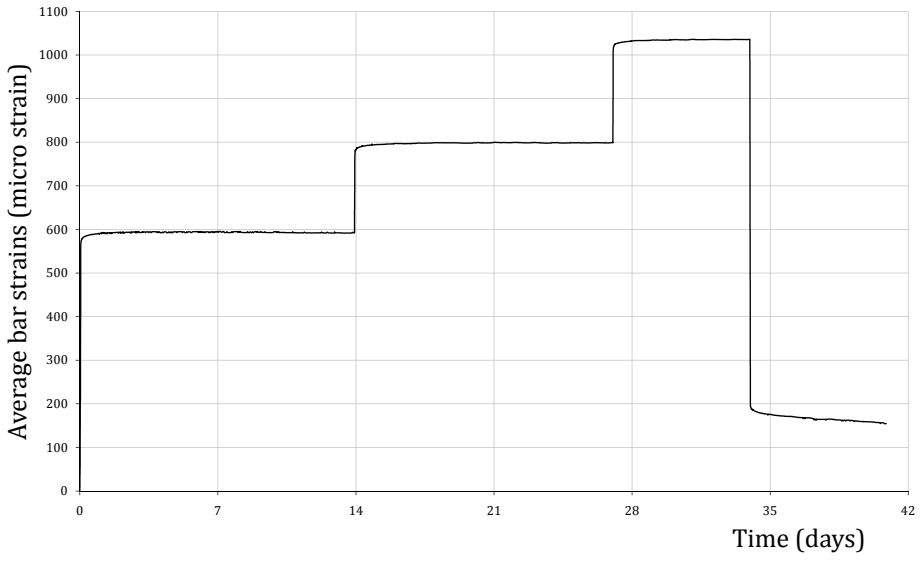

Figure 4.13: Plot of average bar stress in H32 specimen over time from first loading.

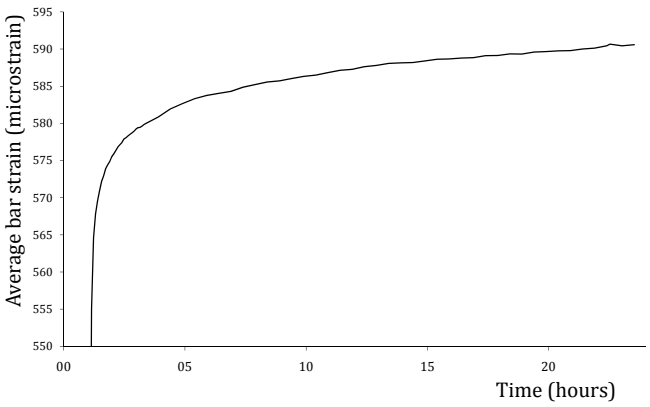

Figure 4.14: Detail of average bar stress in H32 specimen over time from first loading.

Tension stiffening can be quantified as the loss in concrete stress occurring directly after loading while the load is held constant. Using the load readings from the load cell and internal bar strain readings in combination with the prism and bar dimensions the average concrete stress could be calculated. This was done using Equation 4.4.

$$\sigma_c = \frac{F - E_s \varepsilon_s A_s}{A_c} \tag{4.4}$$

where:

σ_c = stress in concrete
F = total tensile force
E_s = elastic modulus of steel
ε_s = average steel strain
A_s = cross-sectional area of steel
A_c = cross-sectional area of concrete

This average concrete stress could be plotted over time for each load stage. In each case this resulted in a plot showing a decay to a final constant value of concrete stress. An example of such a plot is shown in Figure 4.15. Due to the varying rate of decay it was not possible to determine an exact time at which this decay ends and stability is achieved using this plot. By plotting the stress against a logarithmic time scale, however, the exact location at which stability occurred could be identified. The resulting plot for the given example is shown in Figure 4.16. Stability occurs at the change in gradient from negative to horizontal. The slight fluctuations past the point of stability are a result of temperature and humidity changes in the lab. In this case it is clear that the concrete stress reached a constant value after four days.

This operation was performed separately for each of the load stages in this investigation. Figure 4.17 shows the resulting plots for the four tested specimens. In order to allow all load stages for a specimen to be plotted on a single pair of axis the

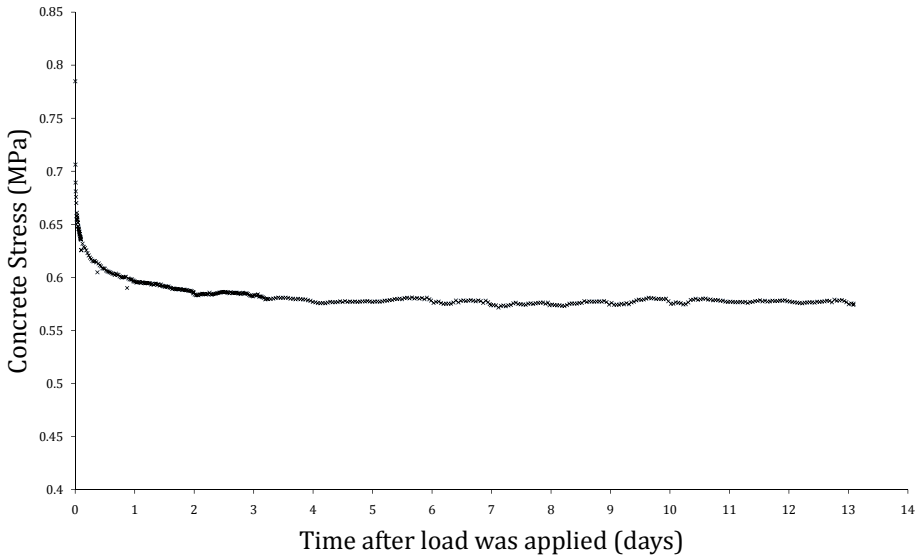

Figure 4.15: Plot of average concrete stress against the time passed after loading for the second load stage of the H32 specimen.

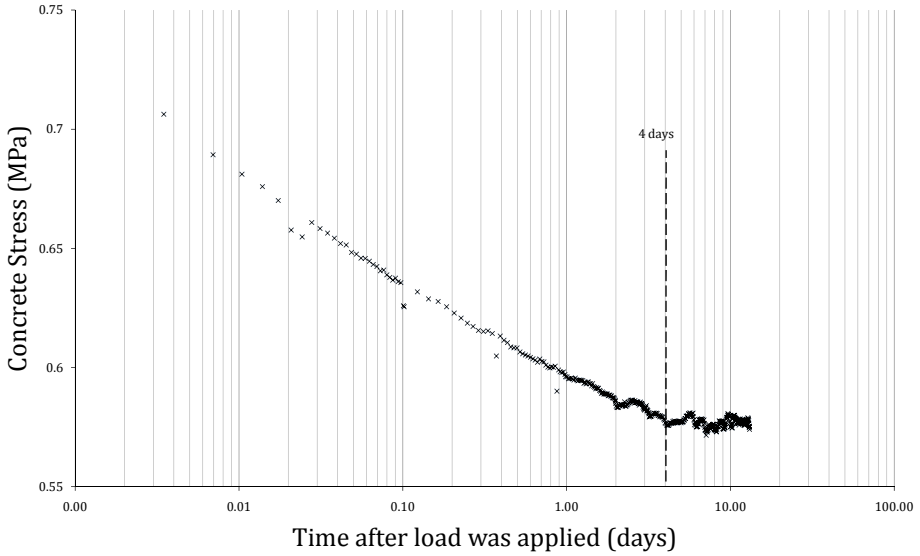

Figure 4.16: Plot of average concrete stress against the time passed using a log scale.

concrete stresses were normalised by the initial concrete stress just after the respective load stage was applied. Plots of each individual load stage with the point of stabilisation marked can be found in Appendix B.

There were a number of unexpected results present which require explanation. The first is the jumps in concrete stress present in the third load stage of the H40 specimen, as can be seen in Figure 4.17(c). After the third load stage was reached it was noticed that the loading weights were in contact with a set of wooden spacers which were kept under the loading weights. These were present so that in the event of the collets or wedges slipping the load could only fall a limited distance. These were removed which

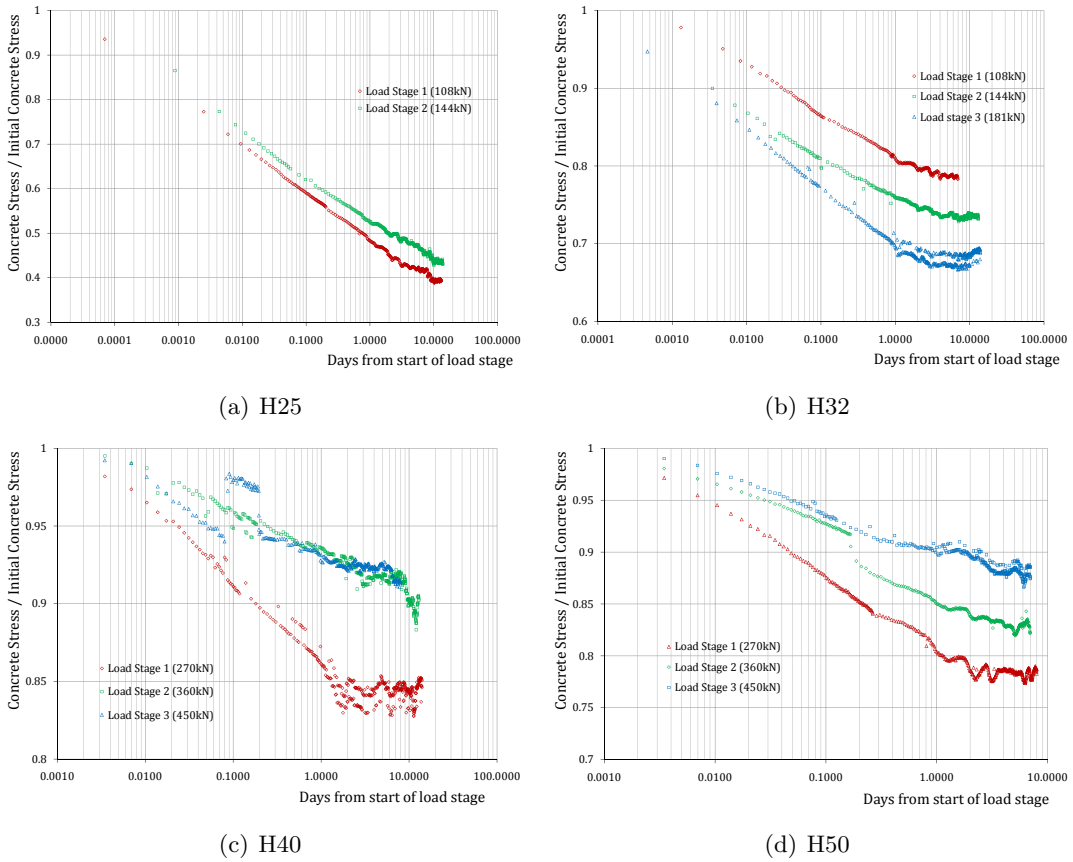

(a) H25

(b) H32

(c) H40

(d) H50

Figure 4.17: Plots of concrete stress against time passed for the tested specimens.

resulted in an increase in load due to the lever arms rotating, causing the observed instantaneous stress increase. Due to this additional load increase there was an onset of yield in the reinforcement. Load was then removed again in order to bring the specimen back to a stable state, resulting in the instantaneous stress decrease. This whole process occurred over 3 hours. The member response was carefully monitored over the following days. This unfortunate event appears not to have affected the rate of tension stiffening decay or caused additional cracking.

A second observation is the drop in concrete stress in the second load stage of the H50 specimen, as can be seen in Figure 4.17(d). This was caused by the opening up of Crack 2 as the crack propagated through the entire cross-section. Previously the crack had only been present on a single side of the specimen. Once again this occurrence was determined not to have had an effect on the specimen response for the load stage in question.

A final observation relates to the final stress achieved after stability occurred. It is widely assumed that long term tension stiffening decays to approximately half its original value [4]. This holds in the case for the H25 specimen. The other three tests, on the other hand, showed stabilised values of between 0.68 and 0.92 times the initial concrete stress. Although there is a significant amount of scatter, there appears to be a

trend that as bar diameter increases the proportion of tension stiffening lost decreases.

The concrete stress plots provided multiple values for the tension stiffening decay period for each specimen tested. Not only did this provide a large data set for comparison of bar diameters, it also allowed an estimate to be made into the effect of stress levels on tension stiffening decay. Table 4.4 shows the decay times determined using the concrete stress plots for each of the specimens tested in this investigation.

Specimen	Decay Time [days]		
	Load Stage		
	1	2	3
H25	9	10	
H32	3	4	4
H40	2	3	2
H50	1.2	3	3

Table 4.4: Decay times for specimens investigated.

In order to extend the data set to include the diameters investigated in previous work the results from previously investigated specimens were also considered. The same analysis described above was applied to the data from the documented tests carried out by Scott and Beeby [4, 3] using T12, T16 and T20 reinforcing bars. This expanded the considered data set to 7 bar diameters which were used to determine the existence of a relation between bar diameter and decay time. The newly computed decay times using the raw data from the previous Durham tests are shown in Table 4.5.

Specimen	Decay Time [days]		
	Load Stage		
	1	2	3
t12b1		23	
t12r1	20	22	
t16b1			6
t16r1	7	5	11
t16b2			15
t16r2	14	14	21
t16b3			19
t16r3		6	33
t20b1			10
t20r1	9	9	11
t20b2			4
t20r2	2	5	6
t20b3			13
t20r3	7	6	12

Table 4.5: Decay times for Durham (2005) tests.

Not all members were subjected to all load stages, hence the blank fields in Table 4.5. It should be noted that in the computation of decay times there is a significant amount of visual estimation involved, especially for specimens with a significant amount of scatter. Additionally the T12 tests resulted in the reinforcement yielding at the second load stage which may have affected the decay of tension stiffening.

A small data set from the Leeds tests was also available and is shown in Table 4.6. Both the Durham and Leeds tests were conducted using 120 × 120 × 1200 mm prisms and similar load stages. In the case of the Leeds test the first number of the specimen name refers to the concrete strength and the second to the reinforcement diameter.

Specimen	Load	Decay Time [days]
30-12	43	18
30-20	43	3
70-16	58	6
70-20	58	30
115-16	72	10
115-20	72	3

Table 4.6: Decay times for Leeds (2005) tests.

The tabulated values do not indicate a relation between concrete strength and tension stiffening decay, nor one between stress level and decay time. In addition, the differences in bond strength between the concrete and steel also do not appear to have had a significant effect on the decay times. For certainty additional investigation is required, however, as the effects of differing bond strengths will only have varied with the bar diameters.

In order to determine whether a relation between bar diameter and tension stiffening decay exists a plot of decay times and bar diameters was assembled. This plot is shown in Figure 4.18 and incorporates both the new large diameter reinforcement results as well as the previously tested small diameter results.

There is a significant amount of scatter in the plot which hinders the formation of a relation between the tension stiffening decay time and bar diameter. Although it is not possible to determine an exact relationship, a clear trend can be observed. As the reinforcing bar diameter increases the decay time decreases. For the larger diameters over 32 mm this decay time reduces to less than one week.

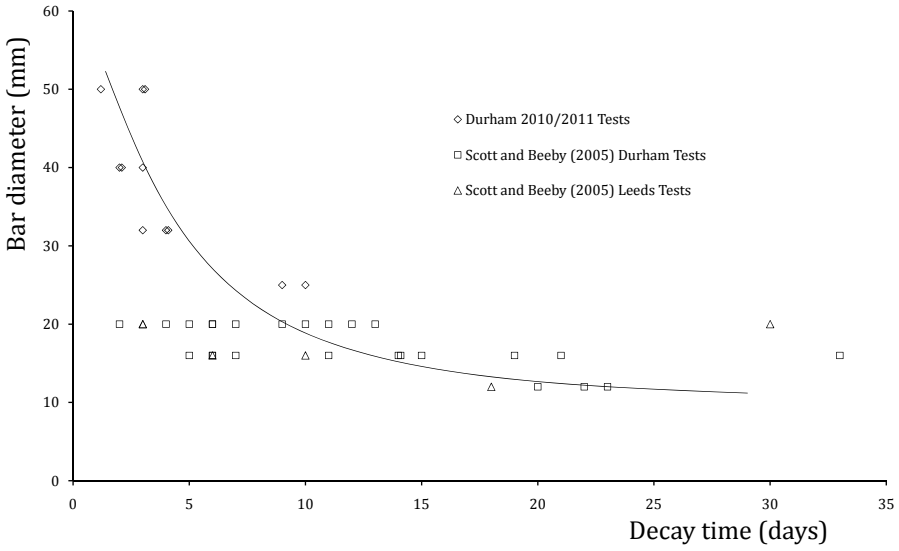

Figure 4.18: Plot of tension stiffening decay times for various bar diameters using data from this and previous investigations.

Chapter 5

Finite Element Modelling

The first published application of finite element models (FEM) to reinforced concrete was presented in 1967 by Ngo and Scordelis [22]. Simply supported beams were analysed by representing the concrete and steel as separate sets of elements. In 1968 Nilson [24] applied non-linear bond-slip properties to his reinforced concrete FEM. Since then a large amount of research has been dedicated to developing finite element models, including Hillerborg, Moléer and Petersson investigating crack propagation in 1976 and Floegl and Mang [33] using FEM for the modelling of tension stiffening in 1982. More recently there has been a large increase in the use of FEM as personal computers and FEM codes have become more readily available. In 2008 Stramandinoli and Rovere [54] developed a tension stiffening model using the ANALEST software package. Wu and Gilbert [41] investigated tension stiffening in 2009 using the RECAP 2D finite element software. These are just a few examples of the vast amount of research available regarding finite elements.

Although the potential for finite element analysis is clear only an estimated 10% of deflection calculations are carried out using FEM [1]. Many research projects develop very specific models for analysing a single case. A wide variety of software is used resulting in no simple method for the application of developed models in practical situations. ABAQUS [50] is one of the most widely used and available software packages for FEM. Its ability to be applied in a wide range of situations makes it ideal for the development of a general use reinforced concrete model.

Focus is placed on the implementation of a steel concrete bond interface model which can be applied using the existing interface definitions in ABAQUS. Four models are presented and their implementation into ABAQUS described. These are then evaluated based on the results from the experimental investigation.

5.1 Cohesive Interface Model

ABAQUS has a number of models for the definition of interactions between surfaces ranging from mechanical contact models to thermal contact models [50]. The most

appropriate in this case is the cohesive surface interaction which is a mechanical model based on traction-separation behaviour. This allows the bond between two surfaces to be expressed as a linear elastic relationship between traction (bond stress) and separation (slip). Additionally damage can be modelled by defining the maximum allowable stress or displacement allowed in the bond. Damage is the term given to the interface behaviour when it stops acting elastically. After the initiation of damage, the evolution of damage can be defined in order to model the behaviour of the bond after the loss of elasticity. This method of modelling is described in detail below.

5.1.1 Elastic Model

Prior to damage initiation the bond stiffness is defined using an elastic constitutive matrix **K** as a relation between the interface tractions and separations. Tractions are the stresses acting on the material surfaces across the interface. Equation 5.1 shows the nature of the linear relationship [55].

$$\mathbf{t} = \mathbf{K}\boldsymbol{\delta} \tag{5.1}$$

where:

$\mathbf{t}$	=	traction stress vector
$\mathbf{K}$	=	elastic constitutive matrix
$\boldsymbol{\delta}$	=	separation vector

The traction stress vector is made up of the normal tractions t_n and the shear tractions t_s and t_t for three dimensions. For two dimensional models there is only a single shear traction t_s. The model is described here for three dimensions, but is equally applicable to two dimensional modelling. The separation vector is built up out of the corresponding contact separations. Contact separations are the relative displacements between nodes on the slave surface and their corresponding projections on the master surface. The master surface is defined as the surface under load, in this case the steel, while the slave surface is the reacting surface, in this case the concrete. Equation 5.2 shows the full constitutive stiffness relationship for defining the stiffness of the bond in matrix form.

$$\begin{Bmatrix} t_n \\ t_s \\ t_t \end{Bmatrix} = \begin{bmatrix} K_{nn} & K_{ns} & K_{nt} \\ K_{ns} & K_{ss} & K_{st} \\ K_{nt} & K_{st} & K_{tt} \end{bmatrix} \begin{Bmatrix} \delta_n \\ \delta_s \\ \delta_t \end{Bmatrix} \tag{5.2}$$

The behaviour of the bond can take two main forms. The first is an uncoupled response. In this case the non diagonal terms are set to zero ($K_{ns} = K_{nt} = K_{st} = 0$). This implies that separation occurring in the tangential direction has no influence on the normal traction stress. Similarly separation normal to the bond surface does not affect the tractions in the tangential shear plain. The second behaviour form is a coupled response. In this case there are relationships between the tractions and separations

acting in different directions. This implies that one or more of the previously mentioned constants in this case have non zero values.

In order to determine the values within the elastic constitutive matrix it is important to understand its origin in terms of material properties. The best way to gain this understanding is by making a comparison between this bond stiffness and a material with a linear stress strain relationship. For such a material we define the Young's modulus (E) as the stress (σ) divided by the strain (ε). Thus stress can be calculated as shown in Equation 5.3.

$$\sigma = E\varepsilon \tag{5.3}$$

In terms of a beam or truss member strain is defined as change in length (dl) over the original length (L) of the member. Figure 5.1 shows this simple case. Replacing strain in Equation 5.3 with this definition allows stress to be defined in terms of displacement.

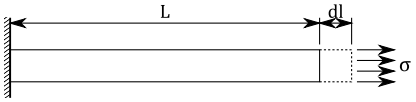

Figure 5.1: Simple case of a beam under tensile load.

$$\sigma = E\frac{dl}{L} \tag{5.4}$$

A comparison between Equations 5.1 and 5.4 provides a material understanding of what the elastic constitutive matrix represents. Effectively it defines the linear stress strain relationship for the interaction between the surfaces. The uncoupled interaction behaviour in the normal direction can be modelled as a truss element with a length equal to the thickness of the cohesive layer (T) as shown in Figure 5.2. This leads to the following definition of K_{nn}.

$$K_{nn} = \frac{E_{nn}}{T} \tag{5.5}$$

E_{nn} represents the Young's modulus of the bonding layer in the direction normal to the bond surface. The units of the constants within the **K** matrix are thus [Force/Length^3] and represent the stiffness, equivalent to Young's modulus, in a homogeneous material.

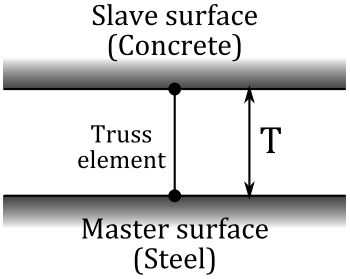

Figure 5.2: Approximation of the cohesive interface in the normal direction.

It is important, however, to understand that the constitutive stiffness matrix does not define a material property but the interface behaviour. The tractions represent the stress between the surfaces and have the associated units of [Force/Length^2]. The separation is equivalent to the change in length and clearly has the units of [Length]. The challenge behind this elastic model is filling the **K** matrix with appropriate values which reflect the steel-concrete bond.

5.1.2 Damage Initiation

ABAQUS models damage, the loss of elasticity, in two stages. The first is damage initiation, the second is damage evolution. In the damage initiation stage the user defines maximum stresses (t_n^o, t_s^o and t_t^o) or maximum displacements (δ_n^o, δ_s^o and δ_t^o) which can be allowed without damage occurring. For this investigation stress is used to define the damage initiation point and hence only the stress criteria are presented here. These are, however, identical for displacements. There are two main types of criteria: the maximum normal stress criterion and the quadratic stress criterion.

The maximum normal stress criterion simply assumes that damage initiates when any one of the three normal stresses exceeds a maximum permitted value. As the expression in Equation 5.6 is equal to one when this is the case ABAQUS uses this to determine whether the point of damage initiation has been reached.

$$\max\left\{\frac{\langle t_n\rangle}{t_n^o}, \frac{t_s}{t_s^o}, \frac{t_t}{t_t^o}\right\} = 1 \tag{5.6}$$

The normal stress, t_n, in Equation 5.6 has been placed within Macaulay brackets. This is to avoid a compressive stress ($t_n < 0$) resulting in damage initiation. Although this is a suitable criterion to define bond damage, a criterion which takes into account all three normal stresses in the definition is preferred as there can be stresses in multiple directions present at the concrete-steel interface.

The quadratic stress criterion defines the initiation of damage using a quadratic interaction function. Similarly to the maximum normal stress criterion, damage initiation takes place when the following statement is equal to one.

$$\left(\frac{\langle t_n\rangle}{t_n^o}\right)^2 + \left(\frac{t_s}{t_s^o}\right)^2 + \left(\frac{t_t}{t_t^o}\right)^2 = 1 \tag{5.7}$$

Equation 5.7 shows that in this case the stresses in each direction now contribute to the definition of damage initiation. The Macaulay brackets once again avoid compressive normal stresses contributing to damage initiation. As with the constitutive stiffness matrix the challenge is defining the values for these maximum normal and tangential stresses.

5.1.3 Damage Evolution

Damage evolution describes the way in which the interface stiffness degrades once the damage initiation criterion is met. This is done by defining the separation at which the bond is fully degraded or the energy required to fully degrade the bond. In order to specify separation as a single variable an effective separation (δ_m) is defined in Equation 5.8.

$$\delta_m = \sqrt{\langle \delta_n \rangle^2 + \delta_s^2 + \delta_t^2} \tag{5.8}$$

Figure 5.3 shows the full bond behaviour characteristic. The effective separation at damage initiation (point A) is represented by δ_m^o while δ_m' represents the effective separation at full degradation (point B). The area under the line (OAM) represents the energy required for full degradation. Damage evolution defines the behaviour between point A and point B. There is a choice of a linear, exponential, or user defined response.

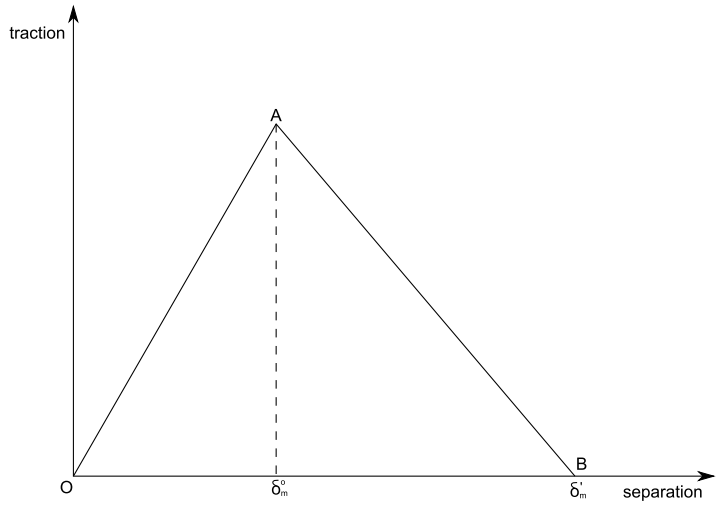

Figure 5.3: Bond traction separation characteristic with linear damage evolution.

Damage evolution based on the traction separation curve is defined using the following relationships.

$$t_n = \begin{cases} (1-D)\bar{t}_n & \bar{t}_n \geq 0 \\ \bar{t}_n & \text{otherwise} \end{cases} \tag{5.9}$$

$$t_s = (1-D)\bar{t}_s \tag{5.10}$$

$$t_t = (1-D)\bar{t}_t \tag{5.11}$$

Equations 5.9 through 5.11 determine the damage tractions (t_n, t_s and t_t) by using a scalar damage variable (D) and the theoretical tractions ($\bar{t}_n$, $\bar{t}_s$ and $\bar{t}_t$) as calculated using the constitutive stiffness matrix in Equation 5.2. The scalar damage coefficient

varies from 0 at initiation of damage (Point A on Figure 5.3) to 1 at full degradation (Point B). As the member is subject only to tension forces it is the bonding in the shear direction which is of greatest significance. The characteristic form of the damage evolution part of the curve (Point A to B in Figure 5.3) can be derived from pull out test results. The traction-separation plot should be adapted to fit the stress-slip relations from experimental tests.

ABAQUS allows the definition of the failure mode mix using a variety of methods including the Power Law [56] and the Benzeggagh-Kenane form [57]. Both are based on the fracture energies in the normal and shear directions. In the uni-axial tension tests considered in this investigation, however, failure occurs primarily in the shear direction. The failure mode is thus known and as a result the mode mix does not need to be defined. For other tests, particularly those including bending, the mode mix does require defining.

It is clear that the accuracy of the analysis is largely dependent on the choice of parameters to describe the traction-separation plot in the interface model.

5.2 Concrete-Steel Interface

There are various models available for modelling the concrete-steel interface. Three models are presented here. Firstly the FIB model is presented, as described in the FIB Model Code 2010 [47], including a suggested alteration by Huang, Engstrom and Magnusson [58]. Secondly a more recent model is described as suggested by Soh, Chiew and Dong [59], and finally one by Cox and Herrmann [60]. In all cases the model is applicable to tangential slip which is the main factor in the uni-axial tension tests.

5.2.1 FIB Model

The FIB stress slip model is based on a simplified bond stress-slip (traction-separation) relationship developed by Eligehausen, Popov and Bertero in 1983 [61]. The model assumes the use of ribbed steel reinforcing bars and neglects the effects of concrete compaction and curing. The form of this relationship is shown in Figure 5.4(a). Equation 5.12 is used to define this curve for monotonic loading.

$$t = \begin{cases} t^m(\delta/\delta_1)^\alpha & \text{for } 0 \leq \delta \leq \delta_1 \\ t^m & \text{for } \delta_1 < \delta \leq \delta_2 \\ t^m - (t^m - t^u)\dfrac{\delta - \delta_2}{\delta_3 - \delta_2} & \text{for } \delta_2 < \delta \leq \delta_3 \\ t^u & \text{for } \delta_3 < \delta \end{cases} \tag{5.12}$$

where:

t^m	=	maximum traction
t^u	=	ultimate traction
δ	=	separation
$\delta_{1,2,3}$	=	separations related to the traction separation plot, defined in Table 5.1
α	=	constant

The code provides values for ribbed reinforcing bars under various conditions including restrained or unrestrained and good or poor bonding. For this investigation the concrete can be considered unconfined with good bond conditions. The suggested values presented by the Model Code are summarised in Table 5.1. Provided the concrete characteristic compressive cylinder strength (f_{ck}) is known these can be used directly in Equation 5.12 to determine the response of the interface.

Parameter	Units	FIB (2010)	Huang *et al.* (1996)
δ_1	[mm]	1.0	1.0
δ_2	[mm]	2.0	3.0
δ_3	[mm]	clear rib spacing	clear rib spacing
δ_4	[mm]		3(rib spacing)
α		0.4	0.4
t^m	[MPa]	$2.5\sqrt{f_{ck}}$	$0.36 f_{ck}$
t^u	[MPa]	$0.40 t_{max}$	$0.40 t_{max}$

Table 5.1: Values of parameters for defining the traction separation curves. [47, 62]

Huang, Engstrom and Magnusson [58] have suggested an updated version of this model, shown in Figure 5.4(b). It has been recognised that the original model is over conservative [62]. Additionally the updated model presents a curve for reinforcement in the plastic range. This is not shown, however, as all reinforcement in this investigation remained in the elastic range. The expressions in Equation 5.12 still hold for the new model with the exception that for $\delta > \delta_3$ a linear reduction to zero applies as shown in Equation 5.13. Table 5.1 shows the adjusted factors applicable to this updated model.

$$t = t^u - t^u \frac{\delta - \delta_3}{\delta_4 - \delta_3} \quad \text{for } \delta_3 < \delta \leq \delta_4 \tag{5.13}$$

In order to implement the above models into ABAQUS a definition of the damage factor is required. Firstly an elastic response for the interface must be defined based on an elastic modulus for the interface. For consistency a modulus of 55.19 MPa is used. This has been derived from an experimental investigation by Malvar [63] which is used in the Soh, Chiew and Dong model. Secondly the damage factor can then be defined according to Equation 5.10 for each point on the traction separation curve. The resulting curves are plotted and compared in Figure 5.8.

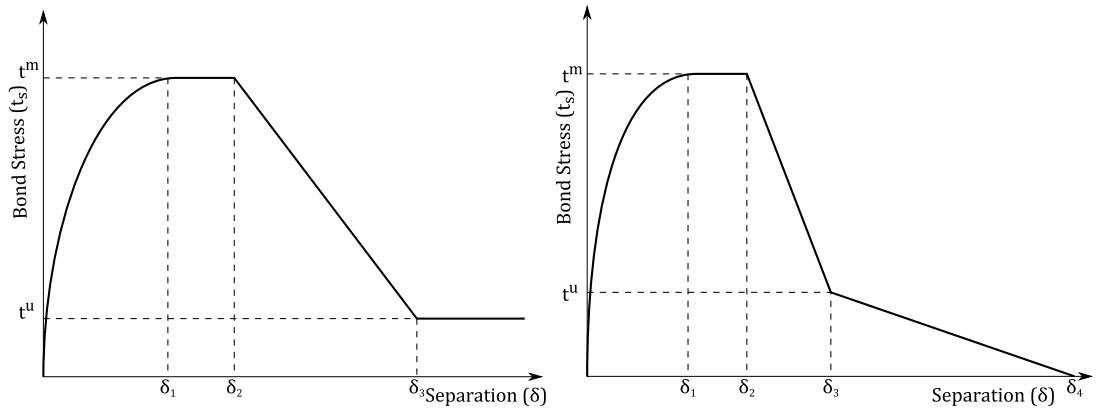

(a) FIB (2010) (b) Huang, Engstrom and Magnusson (1996)

Figure 5.4: The FIB [47] and Huang, Engstrom and Magnusson [58] traction separation model for the tangential slip direction.

5.2.2 Soh, Chiew and Dong Model

A damage model for the concrete steel interface has been suggested by Soh, Chiew and Dong [59]. This model describes the damage model for the interface using traction separation curves, similar to that in Figure 5.3. Two curves are provided, one for the normal traction-opening relationship, and one for the tangential traction-slip relationship. These are shown in Figure 5.5.

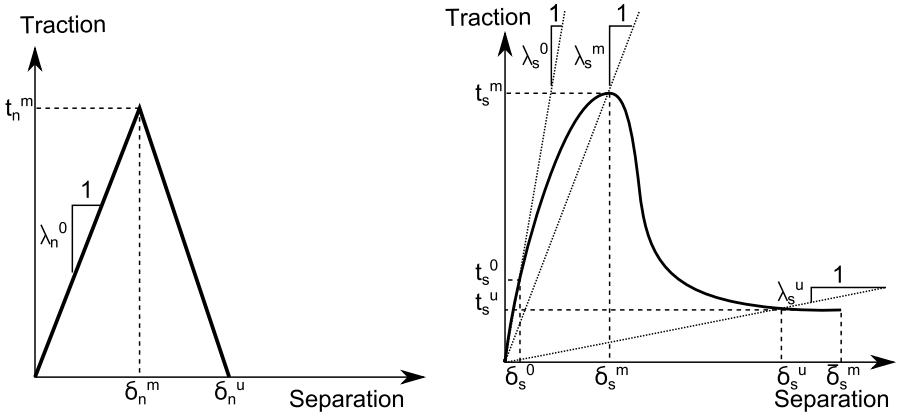

(a) Normal traction opening (b) Tangential traction slip

Figure 5.5: The two traction separation curves for the steel-concrete interface. [59]

The damage factor (D_n) associated with the normal traction-opening curve can be described using the following equation.

$$D_n = \begin{cases} 0 & \text{for } \delta_n \leq \delta_n^0 \\ 1 - \dfrac{1}{a_n x_n} + b_n & \text{for } \delta_n^0 < \delta_n < \delta_n^u \\ 1 & \text{for } \delta_n \geq \delta_n^u \end{cases} \tag{5.14}$$

where:

x_n = ratio of displacement to peak normal traction opening displacement (δ_n/δ_n^m)

a_n = factor $(= (r_u - 1)/r_u)$

b_n = factor $(= 1/(r_u - 1))$

r_u = ratio of limit opening displacement to peak normal traction opening displacement (δ_n^u/δ_n^m)

There is very little experimental data available for the calculation of the normal traction separation curve and associated parameters. This is, however, not of great consequence as in the uni-axial tension tests it is the tangential direction in which the stress transfer between the concrete and steel occurs.

Defining the damage factor for tangential traction-slip is significantly more complicated. From Figure 5.5 the following damage evolution equation is assumed.

$$D_s = \begin{cases} 0 & \text{for } \delta_s \leq \delta_s^0 \\ 1 - \dfrac{1}{a_s x_s^3 + b_s x_s^2 + c_s x_s + d_s} & \text{for } \delta_s^m < \delta_s < \bar{\delta}_s^u \\ 1 & \text{for } u_s \geq \bar{\delta}_s^u \end{cases} \tag{5.15}$$

where:

D_s = damage factor for tangential (shear) direction

x_s = factor $(= \delta_s/\delta_s^m)$

δ_s^m = peak tangential traction slip

δ_s^0 = threshold slip for tangential damage

$\bar{\delta}_s^u$ = limit slip at which the bond can be regarded as totally broken

Figure 5.5(b) can be used to determine the definitions of the factors in the denominator of Equation 5.15. At the point where δ_s is equal to δ_s^0 which is equal to $\beta_0 \delta_s^m$ (where $\beta_0 = \delta_s^0/\delta_s^m$) D_s is equal to 0. From this d_s can be defined as shown in Equation 5.16. Substituting this into Equation 5.15 results in the damage evolution equation shown in Equation 5.17.

$$d_s = 1 - a_s \beta_0^3 - b_s \beta_0^2 - c_s \beta_0 \tag{5.16}$$

$$D_s = \begin{cases} 0 & \text{for } \delta_s \leq \delta_s^0 \\ 1 - \dfrac{1}{a_s(x_s^3 - \beta_0^3) + b_s(x_s^2 - \beta_0^2) + c_s(x_s - \beta_0) + 1} & \text{for } \delta_s^m < \delta_s < \bar{\delta}_s^u \\ 1 & \text{for } u_s \geq \bar{\delta}_s^u \end{cases} \tag{5.17}$$

Three more observations can be made based on Figure 5.5(b). Firstly, when $\delta_s = \delta_s^m$, $x_s = 1$ and $dt_s/d\delta_s = 0$. Secondly, when $\delta_s = \delta_s^m$, $x_s = 1$ and $t_s = t_s^m = \lambda_s^m \delta_s^m$. Finally, when $\delta_s = \delta_s^u$, $x_s = \delta_s^m/\delta_s^m = \beta_u$ and $t_s = t_s^u = \lambda_s^u \delta_s^u$. This results in a series of simultaneous equations (shown in matrix form in Equation 5.18) which can be solved to determine the factors a_s, b_s and c_s.

$$\begin{bmatrix} 2+\beta_0^3 & 1+\beta_0^2 & \beta_0 \\ 1-\beta_0^3 & 1-\beta_0^2 & 1-\beta_0 \\ \beta_u^3-\beta_0^3 & \beta_u^2-\beta_0^2 & \beta_u-\beta_0 \end{bmatrix} \begin{Bmatrix} a_s \\ b_s \\ c_s \end{Bmatrix} = \begin{Bmatrix} 1 \\ \gamma_m - 1 \\ \gamma_u - 1 \end{Bmatrix} \tag{5.18}$$

The various curve characteristics as shown in Figure 5.5(b) are defined as follows: $\beta_0 = u_s^0/u_s^m$, $\beta_u = \delta_s^u/\delta_s^m$, $\gamma_m = \lambda_s^0/\lambda_s^m$, $\gamma_u = \lambda_s^0/\lambda_s^u$, $\lambda_s^0 = t_s^0/\delta_s^0$, $\lambda_s^m = t_s^m/\delta_s^m$ and $\lambda_s^u = t_s^u/\delta_s^u$.

In order to implement this complicated definition for damage evolution for the steel-concrete bond into ABAQUS the tabular input function is used. This allows a curve of any shape to be defined by providing coordinate data. By manually computing a number of points on the traction separation curves these can be implemented into ABAQUS. In this way an accurate behaviour of the steel bond interface is achieved. Numerical data for the above factors was derived for both a concrete-steel plate interface as well as a concrete-steel reinforcement interface, based on experimental data collected by Chiew, Dong and Soh [64] and Malvar [63] respectively. Table 5.2 shows the values which were derived for the concrete reinforcement interface in the tangential slip direction.

Parameter	Symbol	Units	Value
Initial tangential stiffness	λ_s^0	[MPa]	55.19
Maximum tangential traction	t_s^m	[MPa]	11.18
Separation at which damage initiates	δ_s^0	[mm]	0.185
Ratio of slip	β_0		0.3
Limit tangential displacement	δ_s^u	[mm]	9.0
Limit tangential traction	t_s^u	[MPa]	2.45

Table 5.2: Values of parameters for defining traction separation curve. [59]

Using the parameters in Table 5.2 the full definition of the damage parameter can be derived, and thus the traction separation curve. Substituting the parameter values into Equation 5.18 results in the coefficients a_s, b_s and c_s having values of 0.04767, 0.06627 and 2.77044 respectively. Figure 5.6(b) shows the evolution of the damage factor as calculated using Equation 5.17. Figure 5.6(a) shows the resulting traction-slip curve which can be implemented directly into the ABAQUS damage evolution module.

5.2.3 Cox and Herrmann Model

The models discussed above all exclude the geometrical effects of bar shape and rib spacing. The FIB model does include rib spacing as a factor for the tension softening section of the curve which is only relevant at displacements greater than 3 mm. It is clear from the Goto cracking model (Figure 2.4) that the effect of ribs and bar geometry affect the bond between concrete and steel from the initiation of loading. The plastic damage model developed by Cox and Herrmann [60] takes these characteristics directly

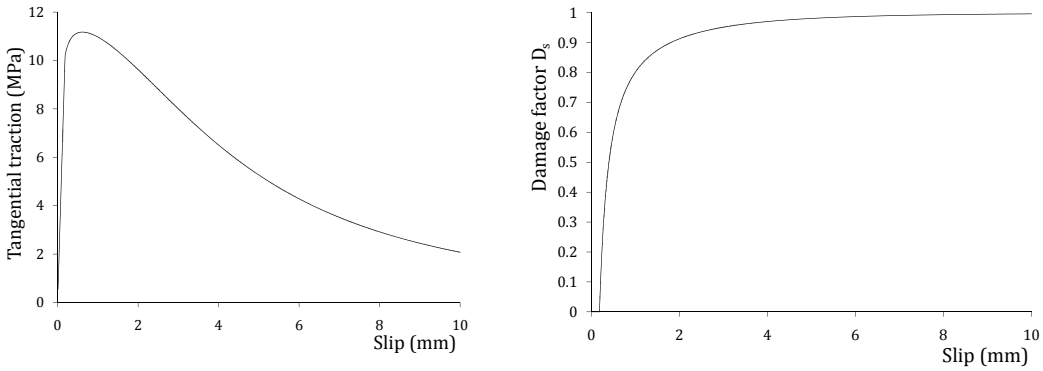

(a) Traction separation response

(b) Damage evolution factor

Figure 5.6: Tangential interface behaviour based on the Soh, Chiew and Dong model. [59]

into account. This model is split into three main parts. The elastic response before damage initiates, the damage response during yield of the interface, and the flow rule model. The latter is used to account for dilation effects, which are not a significant factor in the tension tests being performed in this investigation. This, in combination with a lack of experimental data available for validation of the flow rule [65], has resulted in this section of the model being neglected in the analyses performed here.

The elastic response of the model is similar to that described in Section 5.1.1. Equations 5.19 and 5.20 show how this response is defined. Due to the similarity to Equation 5.1 this can be implemented directly into the ABAQUS interface model.

$$\mathbf{t} = \mathbf{D^e q^e} \tag{5.19}$$

$$\begin{Bmatrix} t_n \\ t_s \end{Bmatrix} = E_c \begin{bmatrix} 0.4 & -0.0012\ \mathrm{sgn}(\delta_t) \\ -0.0012\ \mathrm{sgn}(\delta_t) & 0.1 \end{bmatrix} \frac{1}{D_b} \begin{Bmatrix} \delta_n \\ \delta_s \end{Bmatrix} \tag{5.20}$$

where:

$\mathbf{D^e}$	=	bond elasticity matrix
$\mathbf{q^e}$	=	normalised displacement vector
D_b	=	bar diameter
E_c	=	elasticity of concrete

Thus the $\mathbf{K}$ matrix required for input in ABAQUS (Equation 5.1) is defined as follows.

$$\mathbf{K} = \frac{E_c}{D_b} \begin{bmatrix} 0.4 & -0.0012\ \mathrm{sgn}(\delta_t) \\ -0.0012\ \mathrm{sgn}(\delta_t) & 0.1 \end{bmatrix} \tag{5.21}$$

The damage response is represented in the original model as a yield surface which is based on the bond zone damage as shown in Equation 5.22.

$$d_b = \min\left(\frac{\delta_t^p}{s_r}, 1\right) \tag{5.22}$$

where:

d_b	=	measure of the state of bond zone damage
δ_t^p	=	plastic slip
s_r	=	rib spacing

This implies that once the slip is greater than a single rib spacing the bond is fully degraded and only friction effects remain. The plastic slip (δ_t^p) is defined as the slip which has occurred after the initiation of damage. Equation 5.23 shows the yield criterion which defines the yield surface [66].

$$\left|\frac{t_s}{f_t}\right| = C(d)\{W_e(d)[1 - e^{-\alpha_E(A(d))}] + N(1 - W_e(d))|A(d)|^{\alpha_P}\ \mathrm{sgn}(A(d))\} \tag{5.23}$$

$$A(d) = \frac{-\sigma}{f_t} + \hat{\sigma}(d) \tag{5.24}$$

where:

f_t	=	tensile strength of concrete
$C(d)$	=	function describing isotropic hardening and softening
$W_e(d)$	=	weighting function
α_E	=	calibration parameter (=0.27)
α_P	=	calibration parameter (=0.4)
N	=	calibration parameter (=1.38)
$\hat{\sigma}(d)$	=	function representing kinematic softening

Equation 5.23 contains individual functions describing the various responses of the interface during yield. These include kinematic softening, which is effectively a translation of the yield surface, and isotropic hardening and softening, which represents a change in size of the yield surface [67]. Equation 5.25 defines the function $\hat{\sigma}(d)$ which represents the kinematic softening.

$$\hat{\sigma}(d) = \begin{cases} \hat{\sigma}_0 \left(\dfrac{d_{b2} - d_b}{d_{b2}}\right)^{\beta} & \text{for } 0 \leq d_b < d_{b2} \\ 1 & \text{for } d_{b2} \leq d_b \leq 1 \end{cases} \tag{5.25}$$

where:

$\hat{\sigma}_0$	=	intersect of yield surface with stress axis (=2.25 MPa)
d_{b2}	=	bond zone damage at which kinematic softening stops
β	=	calibration constant (=2.7)

The value of the calibration constant β was based on the Malvar tests [63].

Isotropic hardening and softening is defined by the $C(d)$ function. The initial hardening is a result of concrete crushing in front of ribs and transverse crack growth. As plastic slip increases the mechanisms of fracture and friction become more dominant. This behaviour is represented as an empirically calibrated equation as shown in

Equation 5.26.

$$C(d) = -3.3\exp(-10d_b^{3/5}) + 6\exp(-2.6d_b^{6/5}) + 1.7 \tag{5.26}$$

Finally, the yield criterion effectively consists of two main components: an exponential component and a power component. These are combined using a weighting function $W_e(d)$ which is defined according to Equation 5.27.

$$W_e(d) = \begin{cases} 0 & \text{for } 0 \leq d_b \leq d_{b0} \\ 3\left(\dfrac{d_b - d_{b0}}{d_{b1} - d_{b0}}\right)^2 - 2\left(\dfrac{d_b - d_{b0}}{d_{b1} - d_{b0}}\right)^3 & \text{for } d_{b0} < d_b < d_{b1} \\ 1 & \text{for } d_{b1} \leq d_b \leq 1 \end{cases} \tag{5.27}$$

where:

d_{b0} = Lower limit yield surface interval (=0.38)

d_{b1} = Upper limit yield surface interval (=0.53)

By multiplying Equation 5.23 by the tensile strength of the concrete f_t a relation for the traction-separation curve can be obtained. Using the definition of the damage factor D according to Equation 5.10 the form of the damage curve can be found. This can then be implemented directly into the interface damage evolution model in ABAQUS to complete the model definition. Figure 5.7 shows plots of the resulting traction separation curves for three bar diameters, assuming a rib spacing equal to half the diameter. The evolution of the damage factor D is also shown.

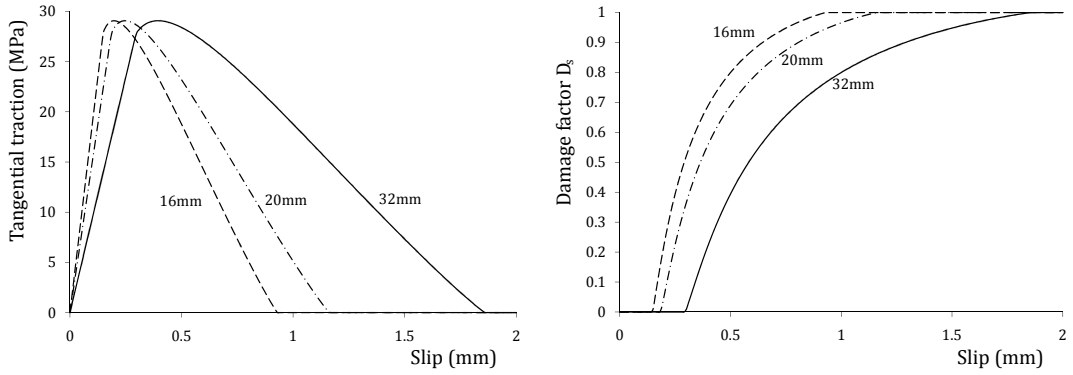

(a) Traction slip response

(b) Damage evolution factor

Figure 5.7: Comparison of traction-slip responses and damage evolution factor for the Cox and Herrmann model using different bar diameters.

5.2.4 Model Comparison

The models described above differ greatly in complexity, response and the various variables used in their definition. Figure 5.8 shows the four discussed models using

the standard suggested values for each on the same plot. The rib spacing is taken as half the bar diameter (in this case a 20 mm bar). Both the FIB based models are simplifications of the experimental traction-slip relationships. The Soh, Chiew and Dong model presents a very smooth alternative with a stiffer initial response. The Cox and Herrmann model, however, presents a significantly different traction separation response. This is due to the discreteness of the model. The other three models are based on pull out tests and thus take into account only the measured slip. The Cox and Herrmann model is based on a yield response at the interface.

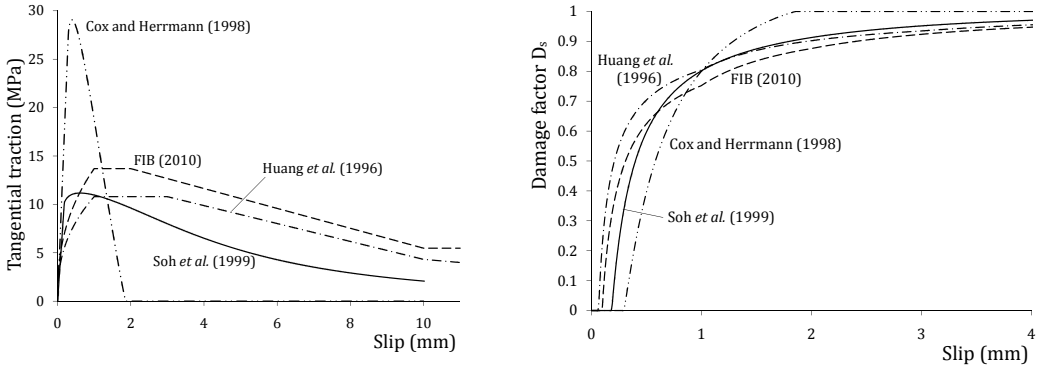

(a) Traction slip response

(b) Damage evolution factor

Figure 5.8: Comparison of traction-slip responses (left) and damage evolution factor (right) for the different interface models.

On the other hand, the damage evolution factor shows a significantly smaller variation between the different models. For consistency the damage evolution factors for each model were based on the same linear elastic response using the elastic modulus of 55.19 MPa except for the Cox and Herrmann model for which the **K** matrix was used as defined in the model. In order to determine the accuracy of each model these were implemented into a FEM representing the experimental tension tests carried out in the experimental program. The analysis results could then be compared to the experimental strain distributions.

Chapter 6

Application of Finite Element Models

The finite element part of this investigation was focused on the development of a method for the analysis of reinforced concrete using the widely available ABAQUS finite element software package. First the various models, as described in Section 5.2, were compared to experimental results in order to determine their accuracy. These were then used to model the various experimental situations which occurred in the testing program in order to identify their limitations. Finally a rib scale model was trialled to determine the potential for modelling rib geometries. Thus three main types of analysis were investigated: a full uncracked specimen, a full cracked specimen and a partial rib model. All analyses presented here were carried out using the ABAQUS 6.9 Student Edition. The cracked and uncracked analyses were performed using two dimensional four node plane stress elements. The use of quadratic elements was trialled, however the software licence did not allow a sufficient mesh density due to a maximum node number restriction. The plane stress approximation is based on the assumption that stresses in the normal direction are negligible.

6.1 Uncracked Analysis

6.1.1 Model Geometry and Properties

In order to be able to provide as high a density of elements as possible as well as computational efficiency the full prism was modelled as a quarter prism in two dimensions. This was done by defining boundary conditions along the lines of symmetry which restricted movement in the direction perpendicular to the plain of symmetry as well as the associated rotations. Figure 6.1 shows a simplified diagram of the geometry of the model. As the interface models evaluated are based on the traction-slip responses for deformed reinforcing bars the ribs were not modelled discreetly as part of the model geometry.

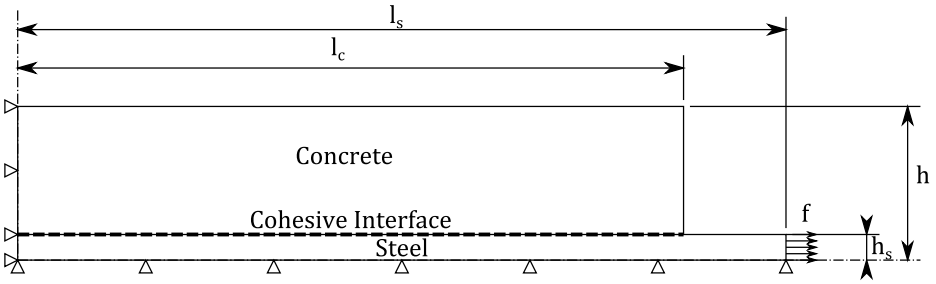

Figure 6.1: Geometry for the uncracked finite element model (not to scale).

There were a number of parameters which required defining. Table 6.1 shows the equations used in the calculation of each parameter and their values for each experimentally tested specimen as well as the T16 and T20 specimens from the previous Durham investigation [4]. In the case of defining the model heights the ratio of steel height to total height was kept equal to the ratio of cross-sectional areas in the actual experimental specimen. This was done to ensure that stress flows remained the same in the two dimensional model as in reality. For the smaller specimens a mesh density of 7.5 mm was used while for the larger specimens a density of 12 mm and 16 mm was used for the 190 × 190 and 300 × 300 prisms respectively. A uniform rectangular mesh layout was chosen. This provided a suitable mesh density while avoiding excessive computation times. A brief validation of these mesh sizes is presented in Section 6.1.3.

Parameter:	l_c [mm]	l_s [mm]	h [mm]	h_s [mm]	f [MPa]
Definition:	$L/2$	$l_c + 100$	$B/2$	hA_s/A	F/A_s
T16	600	700	60	0.838	$F/201.1$
T20	600	700	60	1.309	$F/314.2$
H25	1000	1100	95	1.292	$F/490.9$
H32	1000	1100	95	2.116	$F/804.2$
H40	1000	1100	150	2.094	$F/1256.6$
H50	1000	1100	150	3.272	$F/1963.5$

Table 6.1: Definition and numeric values of model parameters for uncracked FEM model.

In addition to the geometric dimensions of the model the material properties were also required. The loads in this series of tests were kept sufficiently low to allow both the steel and the concrete to be modelled as isotropic elastic materials. An estimation of the Young's modulus and Poisson's ratio were required for both concrete and steel. For reinforcing steel a Young's modulus of 200 GPa and a Poisson's ratio of 0.29 were used. For concrete the FIB Model Code 2010 [47] was used to determine the Young's modulus. This is based on the cube strength as well as which type of aggregates were used. Equation 6.1 shows the equation used.

$$E_c = E_{c0}\alpha_1 \left(\frac{f_{ck} + \Delta f}{10} \right)^{1/3} \tag{6.1}$$

For sandstone aggregates as used in the experimental program E_{c0} is defined as 21.5 GPa while Δf is 8 MPa and α_1 is 0.7. The Model Code suggests the use of 0.2 as the Poisson's ratio for concrete.

The cohesive interface was defined using the damage factor slip responses as shown in Figure 5.8. The definitions for the four cohesive interface models investigated are described in detail in Section 5.2. In each case the interface was defined using the surface definition for the slave surface as the node region definition provided inaccurate results in the preliminary testing.

6.1.2 Interface Model Comparison

For each of the four tested specimens as well as the T16 and T20 specimens from the previous investigation a geometrical model was created according to Table 6.1. The T12 specimen was not used for this comparison as yield took place in the steel which was not being taken into account in this series of models. In each case the maximum load was determined just prior to the first crack formation and this was used to run the finite element tests. These were then plotted over the actual experimental data for that load stage. Figure 6.2 shows such a plot for the H32 specimen.

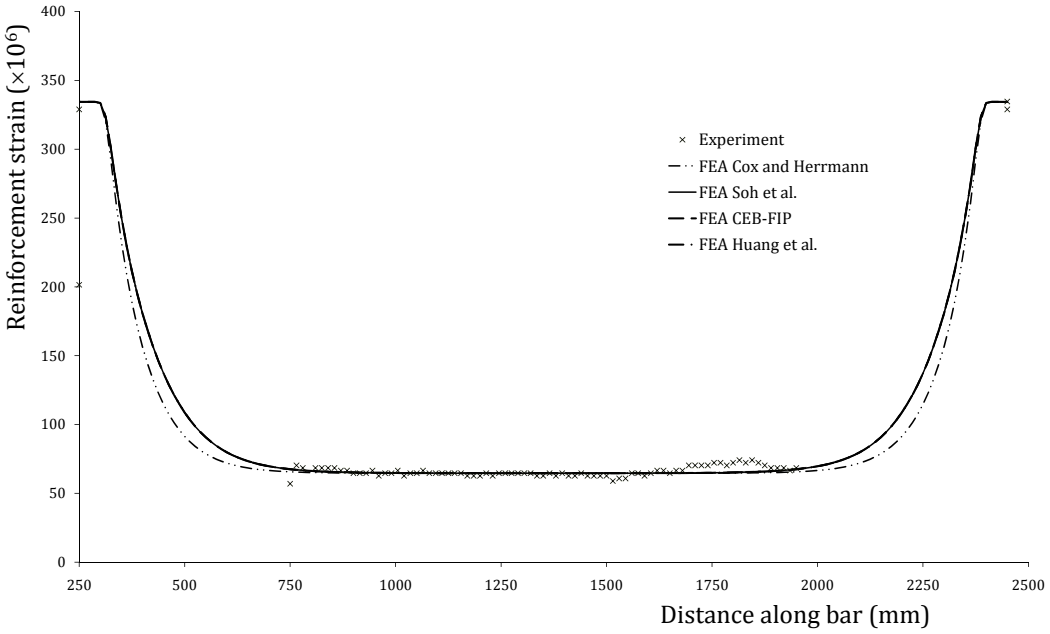

Figure 6.2: Plot of finite element results over H32 Data.

The FIB [47]; Soh, Chiew and Dong [59] and Huang, Engstrom and Magnusson [58] models all result in an almost identical response. The reason for this is the low damage initiation and maximum tensile strength used in these models in comparison to the Cox

and Herrmann [60] model. This can be seen in Figure 5.8 in Section 5.2. The Cox and Herrmann model produces a stiffer bond which can be identified by the lower strains in the concrete near the specimen ends. It is clear from Figure 6.2 and the other plots based on the large diameter bars that the strains in the undamaged central section of the specimen are estimated accurately. Due to the focus of this investigation on tension stiffening there were no gauges in the end zones in which de-bonding occurred. As these are the areas of interest for the interface models the conclusions which can be drawn from the uncracked comparison are limited. The previous small diameter investigation did have gauges in the end zones and thus the uncracked comparison for the T16 and T20 specimens is of interest. The T16 and T20 results are shown in Figure 6.3 and Figure 6.4 respectively.

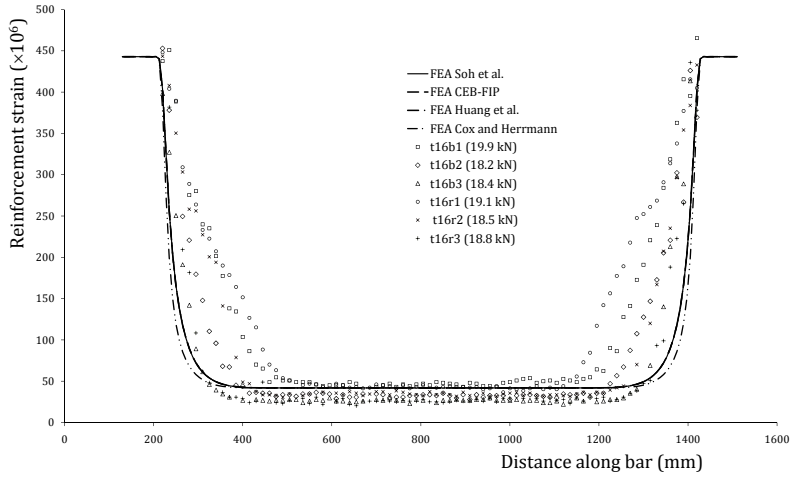

Figure 6.3: Plot of finite element results over T16 Data from [4].

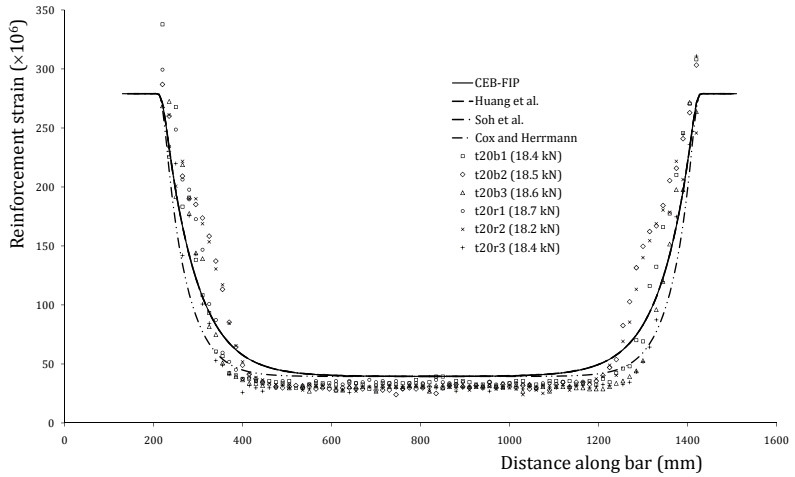

Figure 6.4: Plot of finite element results over T20 Data from [4].

The FIB; Soh, Chiew and Dong and Huang, Engstrom and Magnusson models once again provide an identical response for both the T16 and T20 tests. These models

were all defined using the stiffness derived from the results by Malvar [63], while the Cox and Herrmann model provided its own value. The stresses at which damage initiation was defined to occur varied significantly between the models, as well as damage evolution. This indicated that the stiffness of the interface, represented by the **K** matrix, is the defining factor for interface behaviour in this type of simulation. For all the following simulations only the Cox and Herrmann and Soh, Chiew and Dong models are considered as these have a defined stiffness. The stiffness used in the FIB and Huang, Engstrom and Magnusson models was based on the Soh, Chiew and Dong recommendations and will thus follow this model's response.

As can be seen, all models underestimate the strains around the bonding zones significantly for the T16 experiments while the estimates for the T20 tests appear more accurate. The normalised root mean square deviation has been calculated in order to quantify the model accuracy. These results are shown in Table 6.2. These results indicate a trend that as bar diameter increases the accuracy of the finite element model increases. This was investigated using the cracked analysis for which the results from the large diameter reinforcement investigation could be used.

	Cox and Herrmann	Soh, Chiew and Dong
T16 model	18.5 %	16.1%
T20 model	9.7%	6.9%

Table 6.2: Normalised root mean square deviations for uncracked FEM model.

6.1.3 Mesh Effects

In the analysis described above a global mesh size of 7.5 mm and 12 mm was used for the small and large prisms respectively. In order to validate these results a brief mesh investigation was performed. Figure 6.5 shows the plots for the Soh, Chiew and Dong model as well as the Cox and Herrmann model for a small and large specimen. The results for the FIB and Huang, Engstrom and Magnusson model are not presented as these were similar to the Soh, Chiew and Dong model.

Figure 6.5 shows that the analysis results are stable for both models. The larger specimen size appears to result in better stability in terms of mesh size. The Cox and Herrmann model shows a significantly lower mesh dependency than the Soh, Chiew and Dong model, particularly for the larger specimen size.

6.2 Cracked Analysis

As is clear from the results presented above, limiting the comparison of the interface models to the uncracked stage only allowed model comparison at very low stresses. By modelling the cracked sections the interface models could be compared at significantly higher stress states. In addition, the larger specimen results could be taken into account.

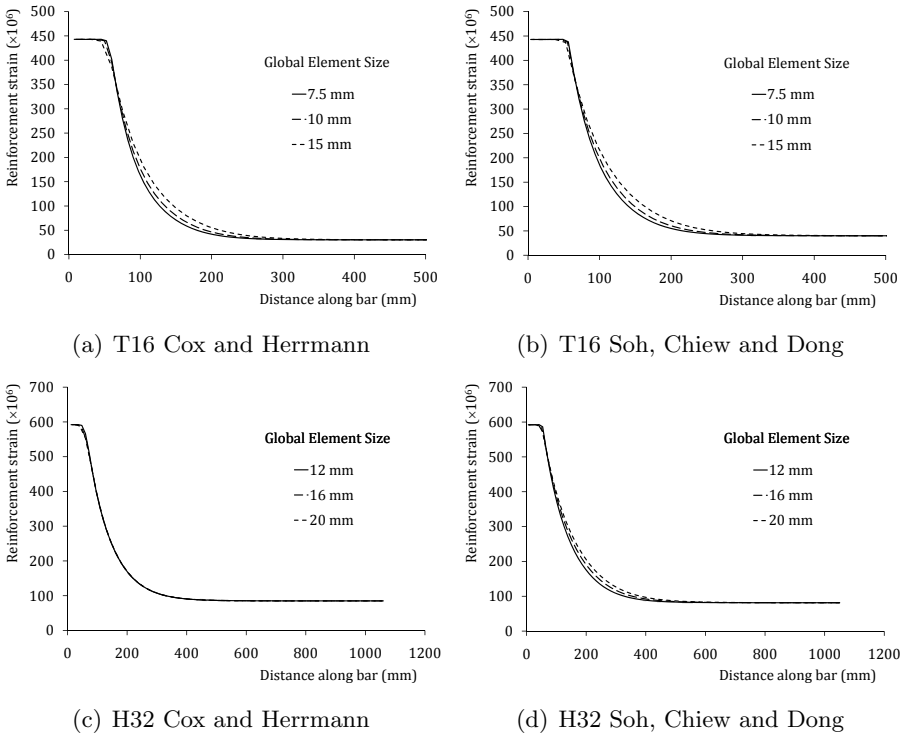

(a) T16 Cox and Herrmann

(b) T16 Soh, Chiew and Dong

(c) H32 Cox and Herrmann

(d) H32 Soh, Chiew and Dong

Figure 6.5: Results from mesh validation analysis.

This was done by modelling the concrete as a number of separate parts with their edges lining up with the location of cracks in the tested sections according to the crack diagrams in Appendix A. A number of load states were selected for each specimen across a range of stresses and crack densities. The full results for each comparison are shown in Appendix C.

6.2.1 Model Geometry

The model geometry for the cracked analyses was similar to that used in the uncracked analysis. Two analyses were used to model each cracked prism. A line of symmetry was drawn through the middle of the central uncracked section in order to provide boundary conditions for each model. Figure 6.6 shows a representation of such a layout.

All model definitions were the same as in the uncracked model, with the exception of the concrete lengths which corresponded to the spacing between cracks, or in the case of the part adjacent to the boundary, half the crack spacing. The ends of the concrete specimen behave identically to crack locations.

6.2.2 Interface Model Comparison

Figure 6.7 shows a typical result for a cracked analysis, in this case the H32 specimen with three cracks at a load of 80 kN. As was the case in the uncracked and low stress analysis the Cox and Herrmann model provides an under estimation of the experimental

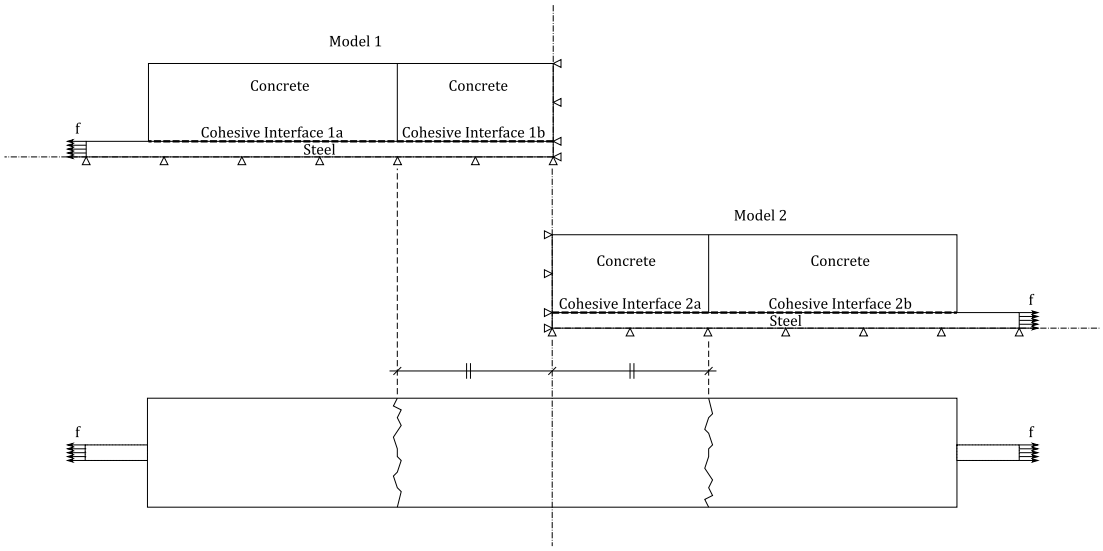

Figure 6.6: Geometry for the cracked finite element model (not to scale).

results. The Soh, Chiew and Dong model provides a more accurate estimation which follows the experimental results better. The normalised root mean square deviations for the interface models are 20.5% and 14.3% respectively. Both models underestimate the peak at 1760 mm. This could be due to there having been more local de-bonding and internal crack development in the specimen. Possible sources for this could be the arrangement of large aggregates or just imperfections which occurred during casting. This is a good example of the difficulty of accurately modelling a non homogeneous material such as concrete using finite elements.

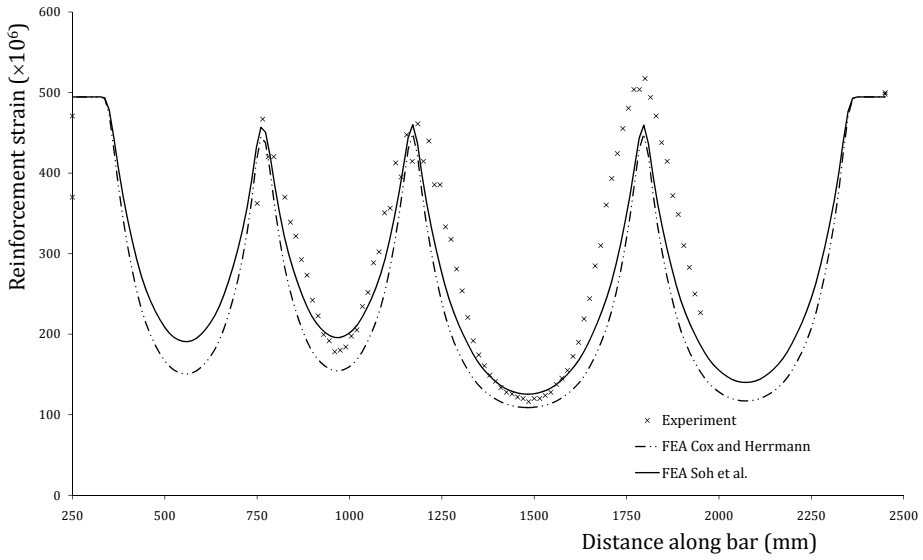

Figure 6.7: FEM results for H32 specimen with 3 cracks at a load of 80 kN.

As the load on the H32 specimen increased more cracks occurred. Figure 6.8 shows the FEM results plotted over the experimental results for the final load stage of 177

kN. It is clear that both interface models significantly underestimate the experimental strains in the specimen between the cracks. The normalised root mean squared deviations are now 84.5% and 65.5% for the Cox and Herrmann and Soh, Chiew and Dong interface models respectively. The most reasonable explanation for these large deviations is the lack of internal cracking, such as that described by Goto [25], in the finite element model. In order to attempt to model this a damage model for the concrete is required which is still the subject of ongoing research [40]. The scope of this investigation was limited to the applications and evaluation of steel-concrete interface models.

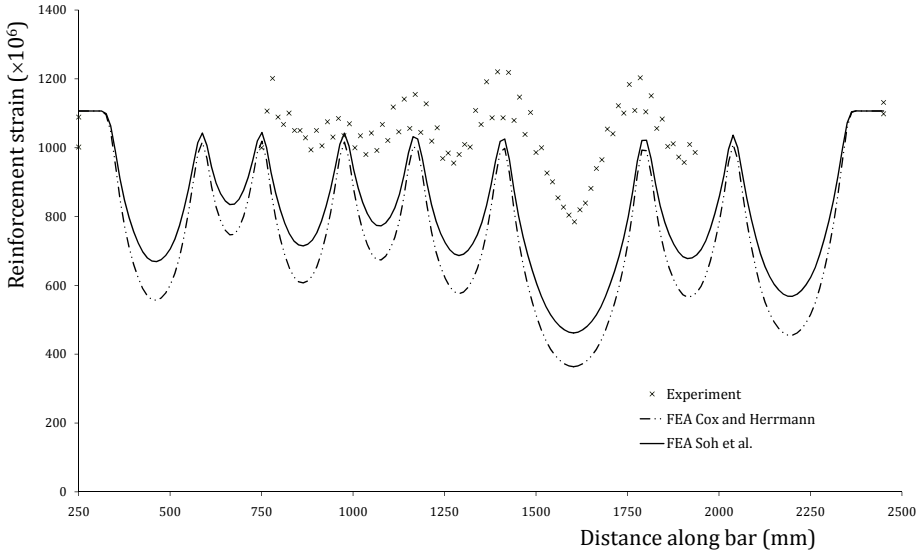

Figure 6.8: FEM results for H32 specimen with 7 cracks at a load of 177 kN.

The lack of internal cracking in the models does not explain the under estimation of strains at the crack locations. There are two main factors which attribute to this. The first is the roughness of the reinforcement mesh compared to the crack density. This is visible in Figure 6.8 as the lack of sharp tips in the strain distribution peaks at crack locations. Increasing the density of the mesh at these locations can limit this effect should computational limitations allow. Secondly local bending was present in the experimental specimen. As described in Section 4.6 this will result in a non uniform distribution of strain particularly where there is local bending at a crack. This, added to the strains arising from the crack, will result in the measurement of larger strains than a model with no flexure would predict.

For both the H40 and H50 specimens the FEM results for all models provide a significant under estimation. Figure 6.9 shows the FEM results plotted over the experimental results for the H50 specimen. Once again the model significantly underestimates the experimental strains. The resulting normalised root mean square deviation for the Cox and Herrmann model is 28.5 % while that for the Soh, Chiew and Dong model is 28.3%. At these relatively low stress levels it would be expected

that the model provides a better approximation. The H50 specimen, however, had a significantly lower bond strength than the other specimens. This resulted in a longer transfer zone which is not reflected in the FEM models. In addition, the H50 specimen was identified to have de-bonding occurring in the transfer zones, which is also not reflected in the interface models.

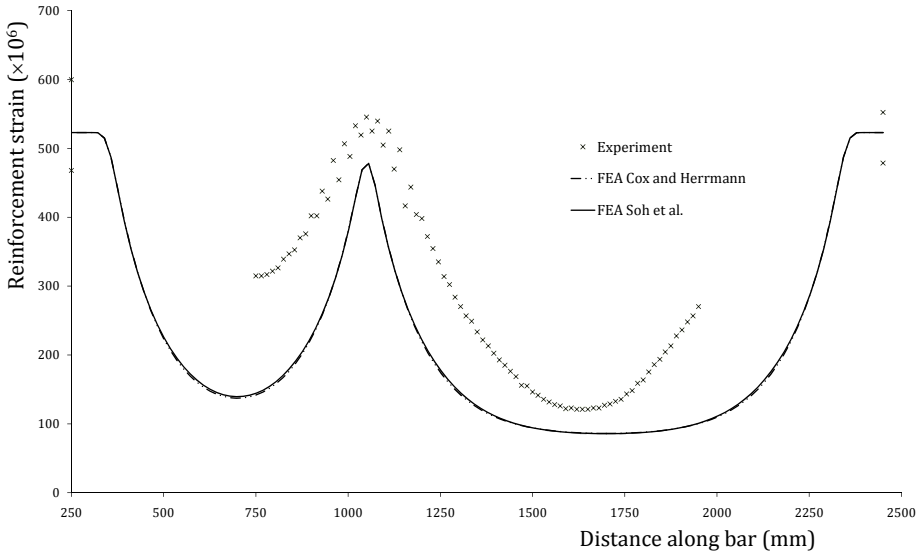

Figure 6.9: FEM results for H50 specimen with 1 crack at a load of 205 kN.

The full set of finite element results for each specimen can be found in Appendix C. The comparisons between finite element results and experimental data have shown that the application of using these simplified models should be limited to low stresses. As the crack density increases the models significantly underestimate strains and stresses in the specimen. The Cox and Herrmann model has the benefit of being able to take bar diameter into account in the calculation of stiffness and damage interactions. The Soh, Chiew and Dong model lacks this ability, but appears to perform similarly to the Cox and Herrmann model none the less and often provides a closer approximation. The mesh analysis indicated that the Cox and Herrmann model has a lower mesh dependency than the other models.

These observations appear to indicate that the discrete interface behaviour is not sensitive to the specimen dimensions. Any effect of the dimensions on results appears to be a purely geometrical effect of the cross-sectional area to bar perimeter ratio. The H50 test indicates that the bond strength is a significant factor in interface behaviour and should be taken into account in the definition of an interface model. This could be achieved through an estimation based on rib height and density. Finally, full de-bonding adjacent to a crack at high stresses should be allowed for an accurate estimation of the strain distribution.

6.2.3 Partial Cracking

As mentioned in Section 4.2 an unusual observation was made during the loading of the H32 specimen. The strains at the third crack location gradually increased until the crack formed, instead of the instantaneous strain increase which was expected. A possible explanation is that an internal crack occurred which propagated to the surface as the load was increased. This partial crack could be modelled using the finite element model. A cut was introduced in the concrete part at the same location as crack three occurred starting at the steel, but ending before reaching the surface. Figure 6.10 shows how such a partial crack is modelled. There is no contact interface along the length of the partial crack.

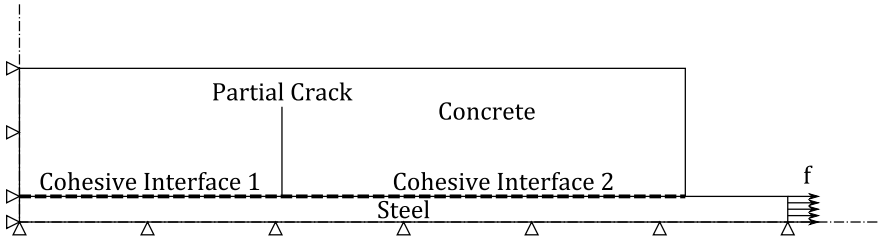

Figure 6.10: FEM model for H32 specimen with partial third crack (not to scale).

The analysis was carried out using the Cox and Herrmann interface model. The results of this analysis are shown in Figure 6.11. It can be seen that the partial crack results in a local increase in strain very similar to that which occurred in the experimental test. The resulting normalised root mean square deviation is 14.1%. The explanation that this gradual increase in bar strains was the result of a propagating internal crack is thus supported by the finite element results.

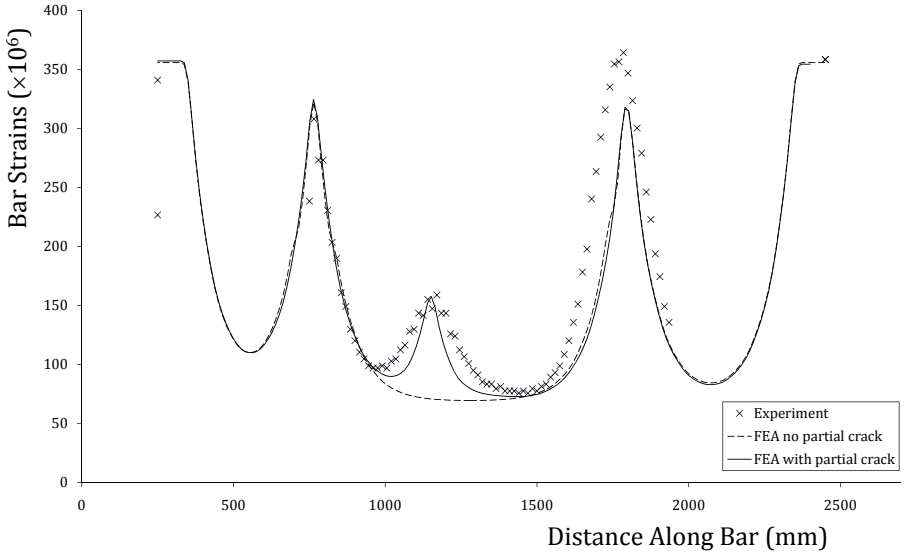

Figure 6.11: FEM results for H32 specimen with partial third crack.

6.3 Rib Scale Model

In order to test whether the concrete-steel interface could be modelled discreetly and to get a better insight into stress paths a small scale model was developed. The main aim of this model was to demonstrate the ability to apply FEM in crack prediction. The ribs were modelled as part of the model geometry instead of being taken into account in the interface model. As a result a different traction-separation response was required which didn't include the rib effects. In this case the Soh, Chiew and Dong model for a concrete-plain steel plate interface was used as described in Section 5.2.2. Figure 6.12 shows the geometry of the model and where loading was applied. The rib height of a 20 mm reinforcing bar was measured and taken as 1.25 mm. The values for the loads were derived from the T20 bar analysis with 0 cracks. In effect, the end of the bar is being modelled. This is equivalent to a single crack face. This model was constructed using 4-node bilinear axisymmetric quadrilateral elements. An axisymmetric set-up was chosen in order to allow the ribs to be modelled without the need for scaling their dimensions as was the case in the previous full specimen analyses.

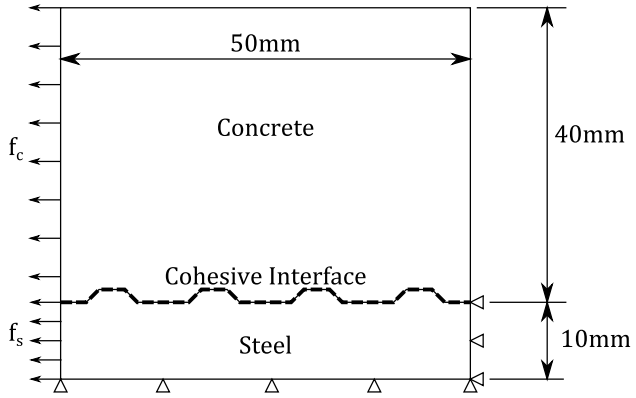

Figure 6.12: FEM model geometry for rib scale analysis.

Figure 6.13 shows the resulting maximum principal strains which occur in the rib model under loading. There is stress transfer between the concrete and strain until the concrete and steel strains are similar. This occurs throughout the entire interface but intensifies at the ribs. If the assumption that cracks form perpendicular to the principal stress directions is applied, a good estimation of the cracking pattern can be made. Figure 6.14 shows a plot of the predicted crack directions at each integration point. There is a great similarity with the experimental observations made by Goto as shown in Figure 2.4. The Goto cracking model is thus supported by the results of this finite element model.

The limitations and roughness of this model should, however, also be noted. Only a very limited section of the specimen is modelled. This influences the stress patterns as all loads were applied in the horizontal direction. Ideally the full extent of the transfer zone should be modelled in order to achieve an accurate stress distribution. As the

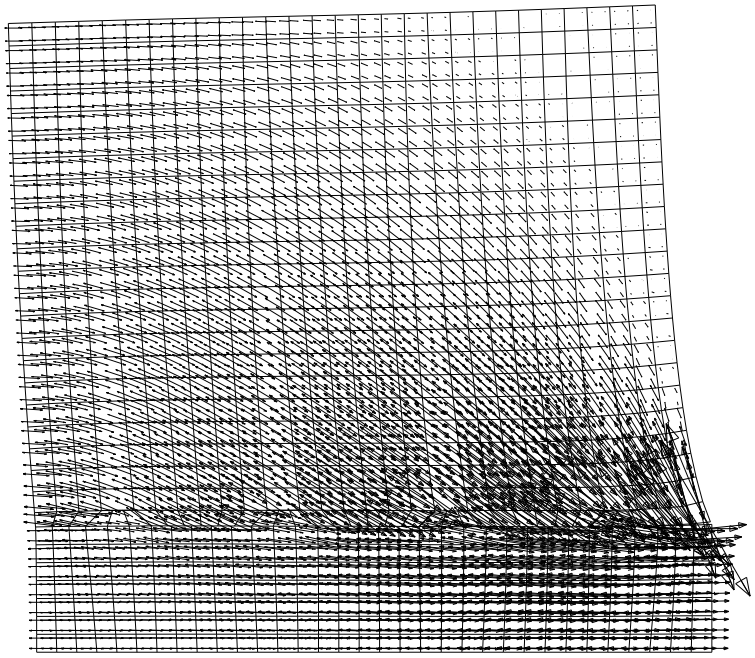

Figure 6.13: Plot of maximum principal strains over deformed rib scale model (deformation scale factor: 400).

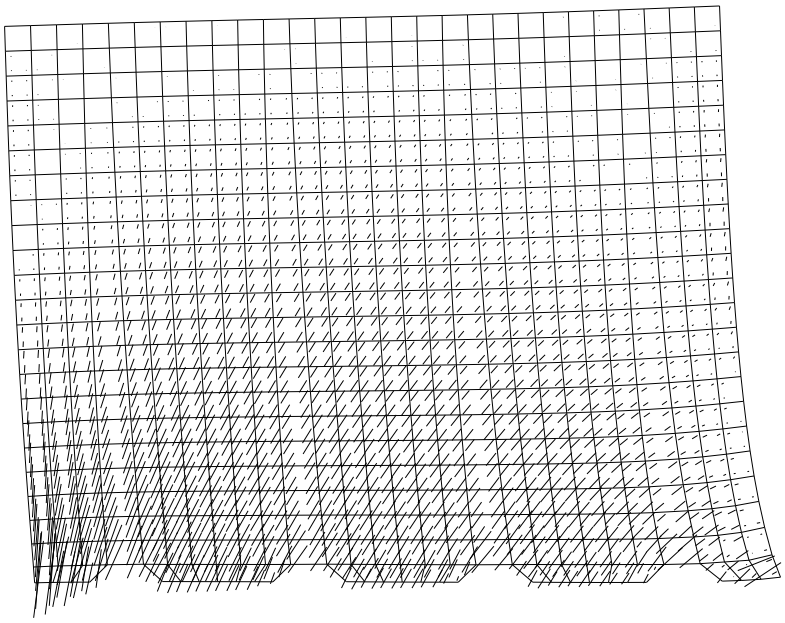

Figure 6.14: Plot of crack directions over deformed concrete model (deformation scale factor: 400).

transfer zones in each case cover at least 200 mm the number of elements required to still allow the discreet modelling of the ribs is significant. This limited analysis does, however, show that using principal stress vectors a prediction of crack paths can be made.

Chapter 7

Conclusions

In this investigation four concrete specimens were tested with large diameter reinforcement. The four specimens each contained a single H25, H32, H40 or H50 reinforcing bar. The main aim of this investigation was to provide data for large diameter specimens and compare these with previous small diameter tension stiffening investigations [3, 4]. In addition, a finite element model (FEM) investigation was conducted in order to asses the implementation of bond models into a widely available FEM software package, in this case ABAQUS.

7.1 Experimental Work

In preparation for the project the four strain gauged bars were assembled. These were then cast in concrete specimens with a target strength of 30MPa. Only the H32 specimen failed to meet the target strength. After a curing time of at least 28 days each specimen was tested at three load stages, with the exception of the H25 specimen which approached yield too rapidly. As a result each specimen provided multiple data sets. In this way a number of theories and concepts could be analysed, the most important of which was the time over which the decay of tension stiffening occurred.

The recorded data and observations support the cracking mechanism as described by Beeby [27]. Each of the specimens followed the guidelines set out in the mechanism and a strain distribution similar to that predicted was recorded. For each specimen the crack spacings and transfer length were measured. An estimate of average bar strain could then be made according to the equations suggested by Beeby and Scott [39]. These proved similar to the average of the bar strains measured within the gauged bars. These equations are thus also supported for large bar diameters by the results of this investigation.

The H50 specimen was determined to have an abnormally low bond strength in comparison with the other tested specimens. As a result the crack density in this specimen was very low with only two cracks observed. This was due to the lower bond strength resulting in a longer transfer length. The low bond strength has been

attributed to the sparse rib pattern and low rib height. Despite this abnormality the tension stiffening response was as expected and the computed average bar strain was accurate.

A final observation relating to cracking is the amount of lateral cracking observed in the loaded specimens. During the small diameter investigation almost no lateral cracking was observed. In this large diameter investigation lateral cracking was abundant. The maximum lengths of these lateral cracks exceeded the prism width. It is believed that these cracks could be the result of wedging action of the large diameter reinforcement. With the limited data set, however, this suggestion can not be confirmed and further study is required in order to understand this phenomenon.

After faults in a preliminary experiment were attributed to bending being present in the tension specimen a method was developed for the analysis of bending. By plotting the final strain readings and making use of the knowledge that these gauges were staggered along the bar the type of bending could be identified. In addition the Demec readings for the front and back of the bar could be plotted. Only the H50 specimen showed a single direction of bending. This was determined to be local bending due to cracking and not to have a significant effect on its response.

The main aim of the experimental program was to identify the tension stiffening response in prisms with large diameter bars. Tension stiffening was determined to stabilise to a constant value of between 0.4 and 0.92 times the initial concrete stress. This occurred within 10 days of the application of load for bar diameters of 25 mm and greater. This is considerably less than indicated by small diameter tests. In most cases the decay time was significantly less, with a minimum of just over one day. The results for the smaller diameters from the previous investigation were also taken into consideration which resulted in the identification of a trend that as bar diameter increases the decay time decreases. There is, however, a very large amount of scatter and the formulation of an exact relation is impossible. More data is required should the development of such a relation be attempted. The code alterations regarding tension stiffening recommended by Beeby, Scott and Jones [38] are thus supported by these experimental results. For BS8110 this involved using only the long term value of 0.55 MPa for tension stiffening (f^*) and using a value of 0.5 for β_2 in Eurocode 2. The decay of tension stiffening in tension members is a short term effect which occurs particularly rapidly in large diameter specimens.

7.2 Finite Element Modelling

In order to demonstrate the ability of using widely available existing finite element software for the analysis of reinforced concrete a simple two dimensional model was developed using the ABAQUS software package. This was based on concrete and steel parts linked using a cohesive interface model. Cracks were modelled by splitting the concrete into separate parts without applying contact at the concrete-concrete

interface. For each stage in the experimental response a model was created and the results compared to the experimental data. A comparison of results for different mesh densities was performed in order to validate the models.

Four interface models were introduced and their implementation into ABAQUS described. These were the FIB [47]; Huang Engstrom and Magnusson [58]; Soh, Chiew and Dong [59] and Cox and Herrmann [60] models. The different interface models were compared to each other and the experimental data. The defining factor for the ABAQUS contact surface was identified as the interface stiffness. As only the Soh, Chiew and Dong and Cox and Herrmann models provided a value for the interface stiffness these models became the focus of the investigation.

The Soh, Chiew and Dong interface provided the better approximation to the experimental results despite the Cox and Herrmann interface allowing more model factors, such as dimensions, to be taken into account. This indicates that the difference in response between the various specimens is largely dominated by the geometrical and material properties of the model. For all interface models, however, the accuracy of the estimated strain distribution diminished at high loads and crack densities. This is due to the inability of these models to allow for internal cracking and slip.

The H50 specimen provided a useful insight into the possibility of model improvement. The long transfer lengths present in the experimental results were not reflected in the FEM results. It is suggested that the inclusion of bond strength in the interface models would greatly improve the accuracy of this analysis. This could be achieved by incorporating rib height, pattern and spacing into the definition of the interface stiffness.

In addition to the standard tension member two additional cases were modelled. The first was the occurrence of a partial crack in order to achieve the response identified in the H32 specimen at the third crack location. The partial crack FEM model resulted in a strain response similar to that recorded in the experiment. The theory that this abnormality was the result of a partial crack was thus supported. The second model was a small scale model of the bar-concrete interface where the ribs were modelled discretely. This resulted in a principal stress plot which supports the cracking scheme identified by Goto [25].

Overall the FEM investigation has shown that even a greatly simplified model can produce a good indication of the strain distribution in a reinforced concrete member. Although there is much potential for future research, the ability to implement cohesive interface models for the analysis of reinforced concrete in a widely available finite element software package such as ABAQUS has been identified.

Chapter 8

Further Work

8.1 Experimental

Although with the multiple load stages per specimen the data set of 11 load stages is significant, a more reliable data set could be achieved if more specimens were tested. This could be done at little expense as the gauged reinforcing bars were recovered after each experiment. Such an extension would provide a valuable insight into the consistency of the results, particularly as the tension stiffening decay time showed a large amount of scatter in this investigation. With a larger data set an indication of statistical certainty in terms of standard deviation could be made. Should the data set be less scattered an attempt could be made at relating the tension stiffening decay time to the specimen geometry.

The low bond strength of the H50 specimen and its unique response has also led to possible theories about links between bond strength, cracking patterns and rib pattern. Sawada [53] has investigated these effects for instantaneous loading, but the response under sustained loading would be equally interesting. This could be investigated by applying sustained loading to a number of specimens using plain reinforcing bars and bars with various rib patterns. It is expected that the plain bars have a low bond strength, and hence a long transfer length and low crack density. The tension stiffening decay times could then also be compared. The H50 specimen in this investigation would indicate that the decay time is not significantly affected by the bond strength.

The recent observations regarding tension stiffening in slabs published by Vollum and Afshar [44] showed tension stiffening to decay at a lower rate than observed in tension members. As a result the use of a tension member for the approximation of the tension zone in a concrete flexural member should be analysed. Beeby and Scott [12] identified that the crack spacing in the constant moment zone of an equivalent slab specimen was less than half that of the tension specimen. Further investigation is required to determine the relation between tension stiffening decay in tension members and flexural members.

8.2 Finite Elements

The finite element investigation in this project was limited to looking at the applicability of finite elements for the prediction of strain distributions and crack patterns using a widely available FEM software suite. The models trialled were limited to the concrete-steel interface and performed reasonably well. The experimental results indicate, however, that the inclusion of the bond strength between steel and concrete could lead to considerably more accurate estimates. A bond model which focuses on the interface stiffness, rather than the damage separation scheme, and takes the discrete bar geometry into account could be developed. Using this in a full ABAQUS finite element suite with quadratic elements would allow accurate modelling of a reinforced concrete member to be achieved.

Finally there is a significant lack of models which allow for the modelling of crack development in concrete. This is challenging due to concrete being a non homogeneous material. A number of methods have been suggested including using a statistical distribution to assign concrete element strengths [40]. There is, however, no easily available method for applying this in a standard finite element suite, such as ABAQUS, which is hindering the use of finite elements as a common analysis tool for concrete members in this respect. The development of such a method or material definition would greatly improve the attractiveness of finite elements for such analyses.

References

[1] Chana, P., Clarke, J., Goodchild, C., Vollum, R. Webster, M. and Webster, R. *Technical Report No. 58: Deflections in concrete slabs and beams.* The Concrete Society, Camberley, 2005.

[2] CEN. *Eurocode 2: Design of Concrete Structures - General rules and rules for buildings.* European Committee for Standardisation, Brussels, 1992.

[3] Beeby, A.W. and Scott, R.H. Mechanisms for long-term decay of tension stiffening. *Magazine of Concrete Research*, 58(5): pages 255–266, 2006.

[4] Scott, R.H. and Beeby, A.W. Long-term tension-stiffening effects in concrete. *ACI Structural Journal*, 102(1): pages 31–39, 2005.

[5] British Standards Institution. *Structural use of reinforced concrete in buildings. CP114.* BSI, London, 1948.

[6] Neville, A.M. *Properties of Concrete, Fourth Edition.* John Wiley & Sons, 1996.

[7] Wilby, C.B. *Concrete Materials and Structures.* University Press, 1991.

[8] Gilbert, R. and Ranzi, G. *Time-dependent behaviour of concrete structures.* Spon Press, 2010.

[9] Holt, E.E. and Leivo, M.T. Methods of reducing early-age shrinkage. In *PRO 17: International RILEM Workshop on Shrinkage of Concrete*, volume 17, page 435. RILEM Publications, 2000.

[10] Subramanian, S., Mallikarjun, V., Rao, B.N., Manohar, S. and Srinivasan, N. Use of admixtures for reducing autogenous shrinkage of concrete. In *Innovations and developments in concrete materials and construction: proceedings of the International Conference held at the University of Dundee, Scotland, UK on 9-11 September 2002*, volume 1, page 235. Thomas Telford, 2002.

[11] Whittle, R. and Jones, T. *Technical Report No. 59: Influence of tension stiffening on deflection of reinforced concrete structures.* The Concrete Society, Camberley, 2004.

[12] Beeby, A.W. and Scott, R.H. Tension stiffening of concrete, behaviour of tension zones in reinforced concrete including time dependent effects. *Supplementary Information TR59*, 2004.

[13] Gilbert, R.I. Deflection calculation for reinforced concrete structureswhy we sometimes get it wrong. *ACI Structural Journal*, 96(6), 1999.

[14] Vollum, R.L. Influences of shrinkage and construction loading on loss of tension stiffening in slabs. *Magazine of Concrete Research*, 54(4): pages 273–282, 2002.

[15] Mains, R.M. Measurement of the distribution of tensile and bond stresses along reinforcing bars. *ACI Journal Proceedings*, 48(11): pages 225–252, 1951.

[16] Yu, W. and Winter, G. Instantaneous and long-time deflections of reinforced concrete beams under working loads. *Journal of the American Concrete Institute*, 57(2): pages 29–50, 1960.

[17] Hajnal-Konyi, K. Tests on beams with sustained loading. *Magazine of Concrete Research*, 15(43-45): pages 3–14, 1963.

[18] Comité Européenl du Béton-Federation Internationale de la Precontrainte. *Recommandations pratiques a l'usage des constructeurs.* CEB, Luxembourg, 1962.

[19] Branson, D.E. *Instantaneous and time-dependant deflections of simple and reinforced concrete beams.* Auburn University, Auburn, USA, 1963.

[20] ACI committee 435. Deflections of Reinforced Concrete Flexural Members. *Journal of the American concrete institute*, June: pages 637–673, 1966.

[21] ACI Committee 318. *318-08: Building Code Requirements for Structural Concrete and Commentary.* American Concrete Institute, Farmington Hills, USA, 2008.

[22] Ngo, D. and Scordelis, A. Finite element analysis of reinforced concrete beams. In *ACI Journal Proceedings*, volume 64. ACI, 1967.

[23] Beeby, A.W. *Short term deformations of reinforced concrete members.* Technical Report 42.408. Cement and Concrete Association, 1968.

[24] Nilson, A.H. Nonlinear analysis of reinforced concrete by the finite element method. In *ACI Journal Proceedings*, volume 65. ACI, 1968.

[25] Goto, Y. Cracks formed in concrete around deformed tension bars. *ACI Journal*, 68(4): pages 244–251, 1971.

[26] Illston, J.M. and Stevens, R.F. Long-term cracking in reinforced concrete beams. *Proceedings of the ICE*, 53(2): pages 445–459, 1972.

[27] Beeby, A.W. A study of cracking in reinforced concrete members subjected to pure tension. *Cement and Concrete Association*, Report 42.468: pages 593–601, 1972.

[28] Rao, P.S. and Subrahmanyam, B. Trisegmental moment-curvature relations for reinforced concrete members. In *ACI Journal Proceedings*, volume 70. ACI, 1973.

[29] Clark, L.A. and Speirs, D.M. *Tension stiffening in reinforced concrete beams and slabs under short-term load*, volume 42. Cement and Concrete Association, 1978.

[30] Clark, L.A. and Cranston, W.B. The influence of bar spacing on tension stiffening in reinforced concrete slabs. In *Proceedings, International Conference on Concrete Slabs, Dundee*, pages 118–128. 1979.

[31] Comite Euro-International du Beton-Federation Internationale de la Precontrainte. *Model Code for Structural Concrete*. CEB-FIP, London, 1978.

[32] British Standards Institution. *Structural use of concrete. Part 1: design materials and workmanship. CP110 Part: 1*. BSI, London, 1972.

[33] Floegl, H. and Mang, H.A. Tension stiffening concept based on bond slip. *Journal of the Structural Division*, 108(12): pages 2681–2701, 1982.

[34] Scott, R.H. and Gill, P.A.T. Short-term distributions of strain and bond stress along tension reinforcement. *The Structural Engineer*, 65(2): pages 39–43, 1987.

[35] Vollum, R.L., Moss, R.M. and Hossain, T.R. Slab deflections in the cardington in-situ concrete frame building. *Magazine of Concrete Research*, 54(1): pages 23–34, 2002.

[36] Comite Euro-International du Beton. *CEB/FIP model code (design code) 1990*. Thomas Telford Ltd., London, 1993.

[37] Scott, R.H. and Beeby, A.W. Test rigs for long-term tension tests. *Strain*, 41: pages 151–155, 2005.

[38] Beeby, A.W., Scott, R.H. and Jones, A.E.K. Revised code provisions for long-term deflection calculations. *Proceedings of Institution of Civil Engineers - Structures and buildings*, 158(1): pages 71–75, 2005.

[39] Beeby, A.W. and Scott, R.H. Cracking and deformation of axially reinforced members subjected to pure tension. *Magazine of Concrete Research*, 57(10): pages 611–621, 2005.

[40] Beeby, A.W. and Scott, R.H. Insights into the cracking and tension stiffening behaviour of reinforced concrete tension members revealed by computer modelling. *Magazine of Concrete Research*, 56(3): pages 179–190, 2004.

[41] Wu, H.Q. and Gilbert, R.I. Modelling short-term tension stiffening in reinforced concrete prisms using a continuum-based finite element model. *Engineering Structures*, 31: pages 2380–2391, 2009.

[42] Bischoff, P.H. Reevaluation of deflection prediction for concrete beams reinforced with steel and fiber reinforced polymer bars. *Journal of Structural Engineering (ASCE)*, 131(5): pages 752–767, 2005.

[43] Gilbert, R.I. Discussion of "reevaluation of deflection prediction for concrete beams reinforced with steel and fiber reinforced polymer bars". *Journal of Structural Engineering (ASCE)*, 132(8): pages 1328–1330, 2006.

[44] Vollum, R.L. and Afshar, N. Influence of construction loading on deflections in reinforced concrete slabs. *Magazine of Concrete Research*, 61(1): pages 3–14, 2009.

[45] British Standards Institution. *Structural use of concrete. Code of practice for design and construction.* BSI, Milton Keynes, 1997.

[46] Scott, R.H. Uk code requirements for deflection control. In *Code provisions for deflection control in concrete structures*, volume SP-203. ACI, 2001.

[47] Fédération internationale du béton. *Model code 2010: first complete draft, Volume 1.* FIB, 2010.

[48] ACI Committee 435. *Control of Deflection in Concrete Structures.* American Concrete Institute, Farmington Hills, USA, 2003.

[49] Branson, D.E. Design procedures for computing deflections. *Journal of the American Concrete Institute*, 65(9): pages 730–742, 1968.

[50] Hibbitt, Karlsson and Sorensen. *ABAQUS/CEA Users Manual.* Dassault Systmes, 2009.

[51] Nilson, A.H. Bond stress-slip relations in reinforced concrete. *Report 345*, 1971.

[52] Chen, W.F. *Plasticity in reinforced concrete.* J. Ross Publishing, 2007.

[53] Sawada, S. *The differences in the effect of bond on service behaviour between plain and deformed bars.* University of Leeds, 2004. MSc(Eng) Dissertation.

[54] Stramandinoli, R. and La Rovere, H. An efficient tension-stiffening model for nonlinear analysis of reinforced concrete members. *Engineering Structures*, 30(7): pages 2069–2080, 2008.

[55] Hibbitt, Karlsson and Sorensen. *ABAQUS Analysis Users Manual*, chapter 32.1.10. Dassault Systmes, 2009.

[56] Reeder, J.R. 3d mixed-mode delamination fracture criteria-an experimentalist's perspective. *NASA/TM-1992-104210*, pages 1–49, 1996.

[57] Benzeggagh, M.L. and Kenane, M. Measurement of mixed-mode delamination fracture toughness of unidirectional glass/epoxy composites with mixed-mode bending apparatus. *Composites Science and Technology*, 56: pages 439–449, 1996.

[58] Huang, Z., Engstrm, B. and Magnusson, J. Experimental and analytical studies of the bond behaviour of deformed bars in high strength concrete. *4th International Symposium on Utilization of High Strength-High Performance Concrete*, 3: pages 1115–1124, 1996.

[59] Soh, C.K., Chiew, S.P. and Dong, Y.X. Damage model for concrete-steel interface. *Journal of Engineering Mechanics*, 125(8): pages 979–983, 1999.

[60] Cox, J.V. and Herrmann, L.R. Development of a plasticity bond model for steel reinforcement. *Mechanics of cohesive-frictional materials*, 3(2): pages 155–180, 1998.

[61] Eligehausen, R., Popov, E. and Bertero, V. Local bond stress-slip relationships of deformed bars under generalized excitations. *University of California; Report no. UCB/EERC-83/23 of the National Science Foundation*, 1983.

[62] Federation Internationale du Beton. *Bond of Reinforcement in Concrete: state of the art report*. Sprint-Druck, Stuttgart, 2000.

[63] Malvar, L.J. Bond of reinforcement under controlled confinement. *ACI Materials Journal*, 89(6): pages 593–601, 1992.

[64] Chiew, S.P., Dong, Y.X. and Soh, C.K. Concrete-steel plate interface characteristics for composite construction. In B. Toppling, editor, *Proc., 7th international conference on civil and structural engineering computing*. Civil Comp., 1999.

[65] Cox, J.V. and Herrmann, L.R. Validation of a plasticity bond model for steel reinforcement. *Mechanics of Cohesive-frictional Materials*, 4(4): pages 361–389, 1999.

[66] Guo, J. and Cox, J.V. Implementation of a plasticity bond model for reinforced concrete. *Computers & Structures*, 77(1): pages 65–82, 2000.

[67] Suresh, S. *Fatigue of materials*. Cambridge University Press, 1998.

Appendix A

Crack diagrams

A.1 H25

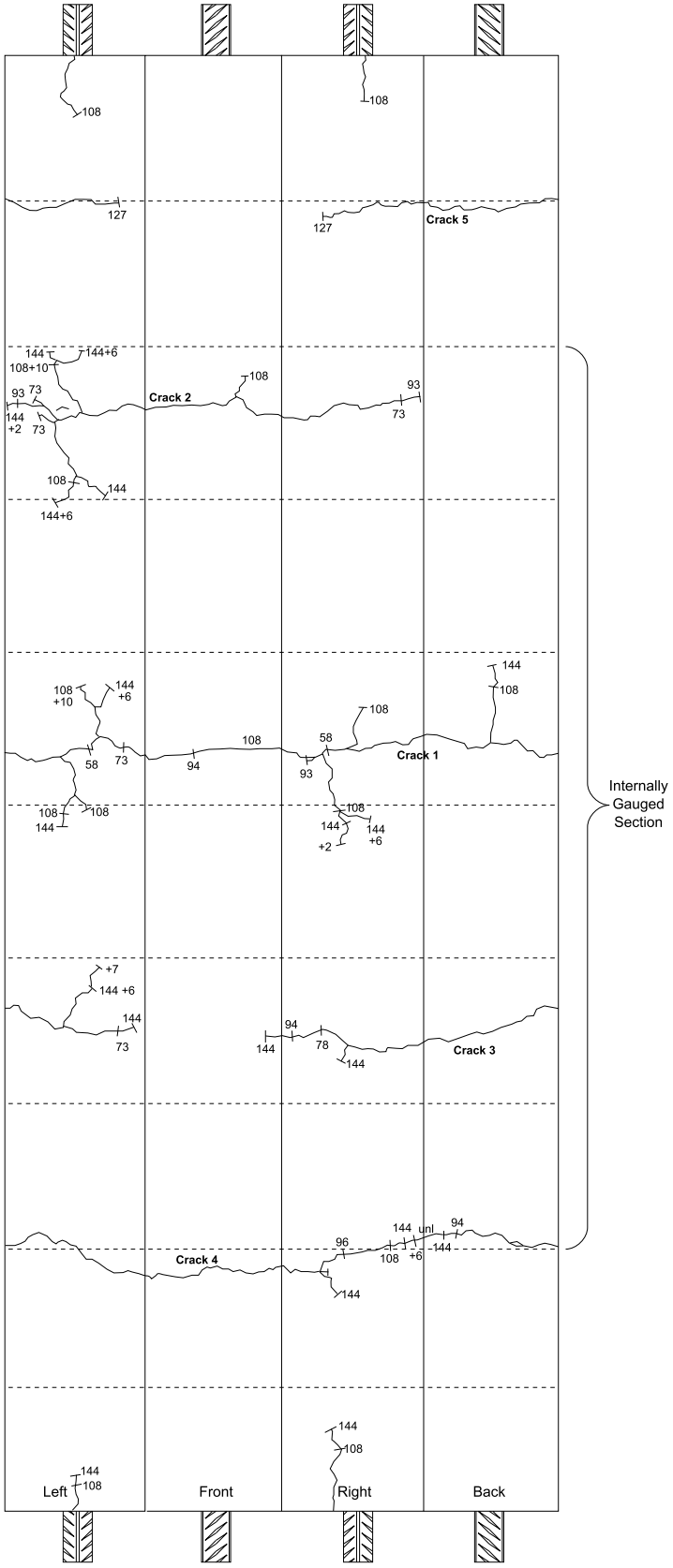

Figure A.1: H25 Final Crack Diagram.

A.2 H32

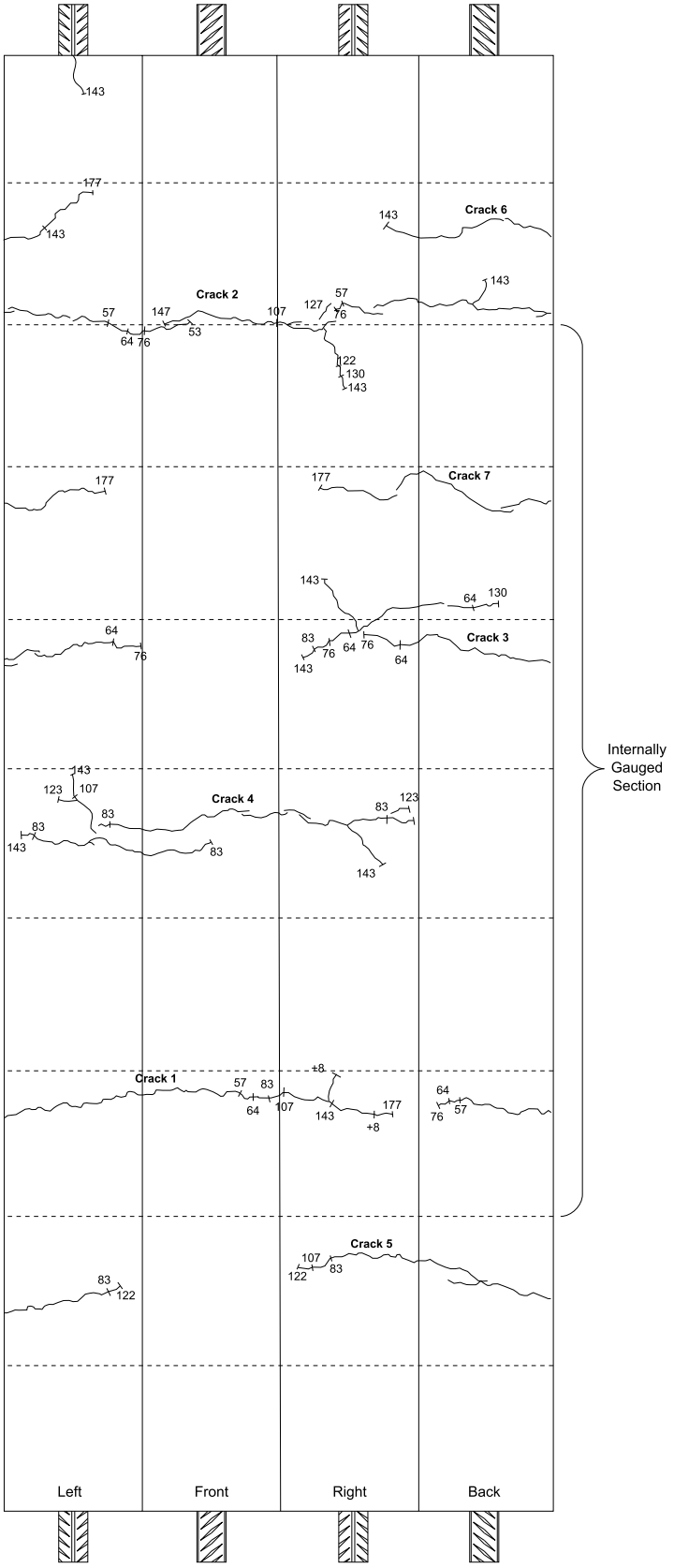

Figure A.2: H32 Final Crack Diagram.

A.3 H40

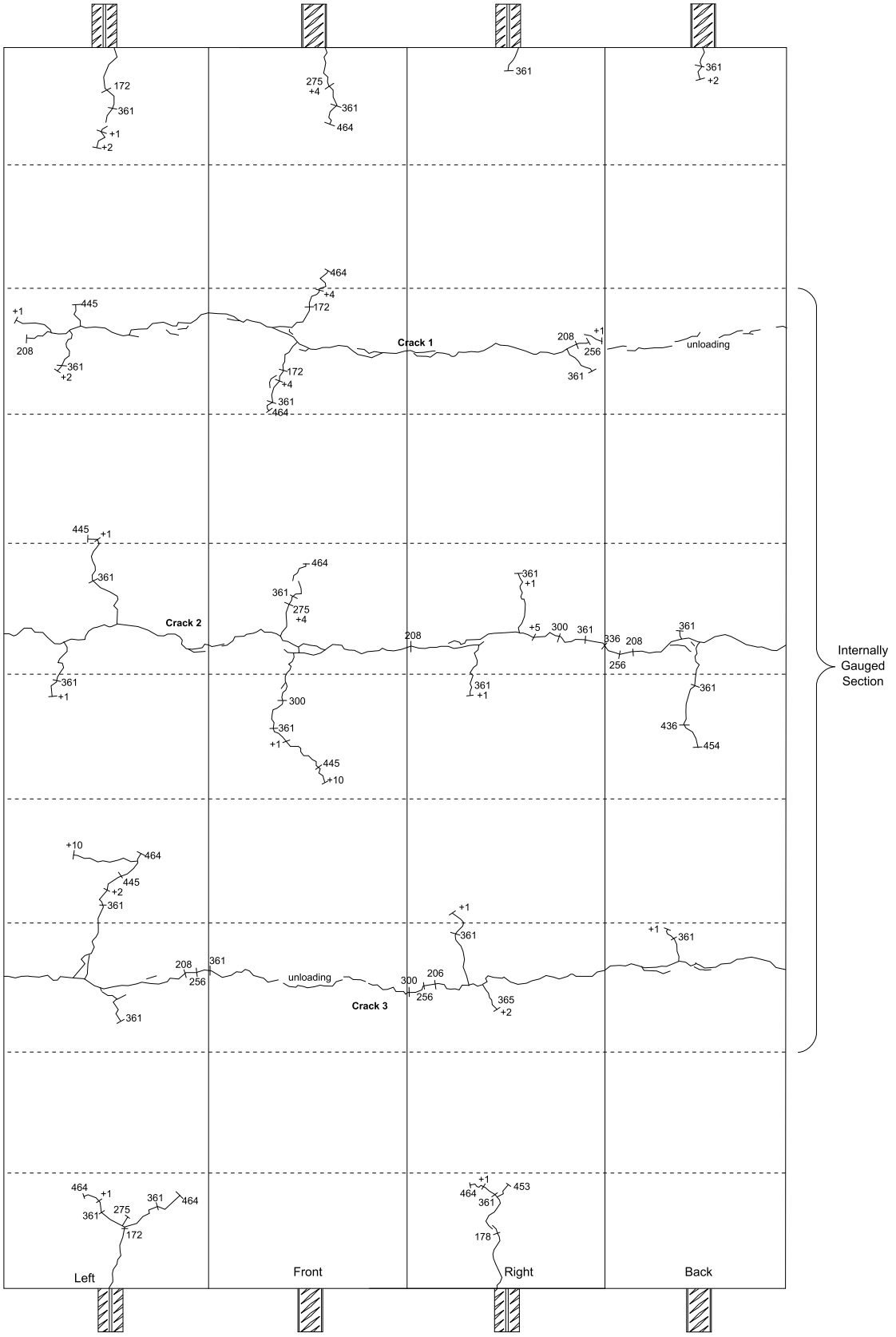

Figure A.3: H40 Final Crack Diagram.

A.4 H50

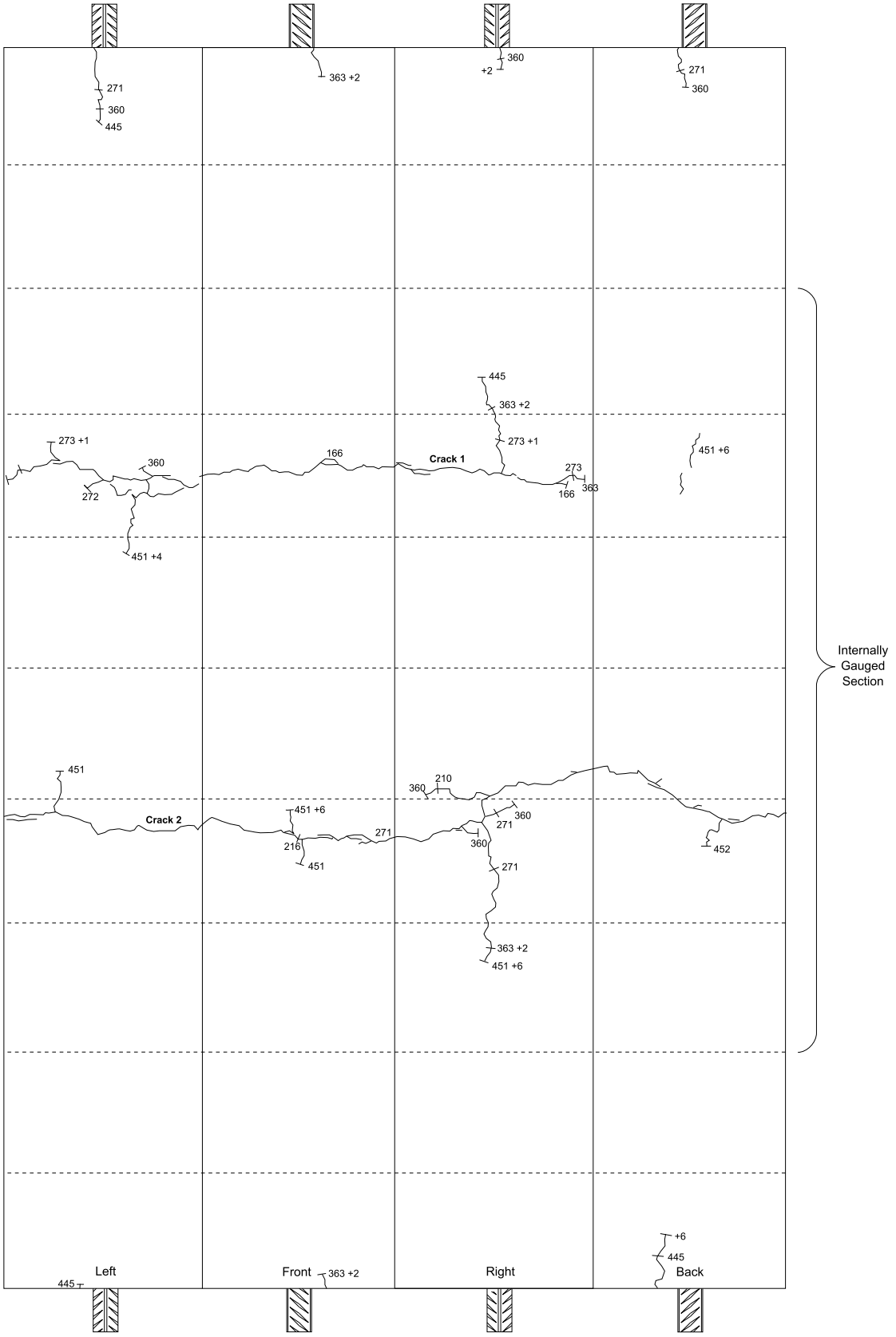

Figure A.4: H50 Final Crack Diagram.

Appendix B

Tension Stiffening Decay Plots

B.1 H25

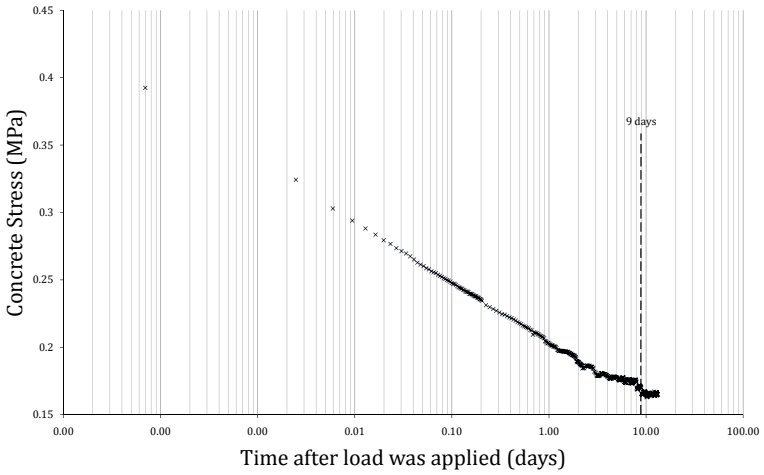

(a) Load Stage 1 (108 kN)

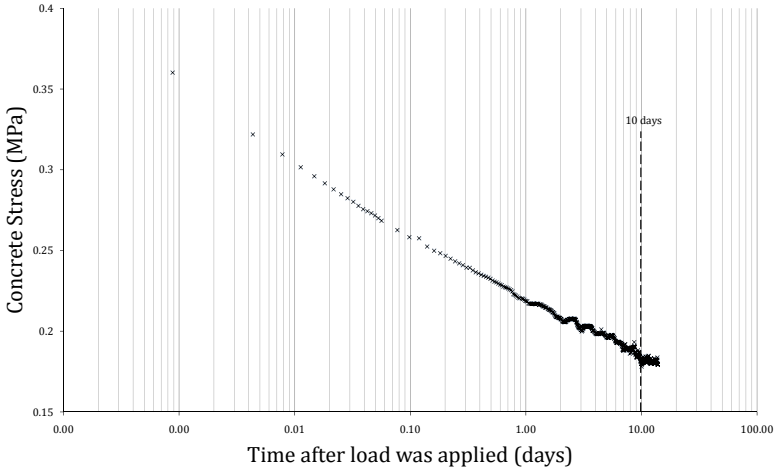

(b) Load Stage 2 (144 kN)

Figure B.1: Logarithmic plots of concrete stress against time with tension stiffening decay time indicated for H25 tests.

B.2 H32

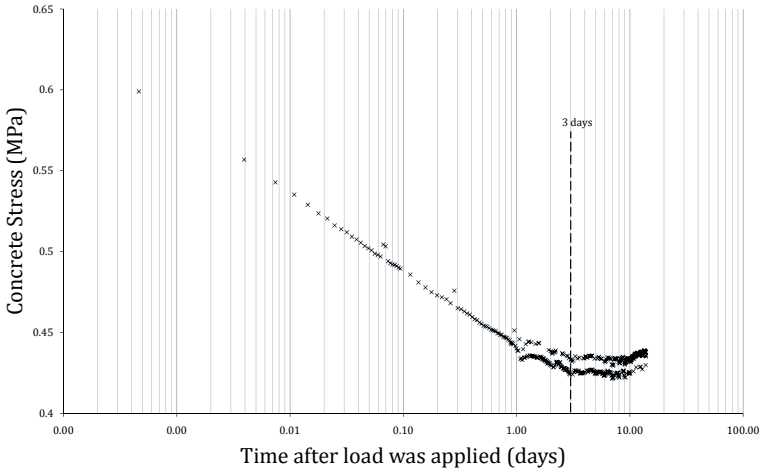

(a) Load Stage 1 (108 kN)

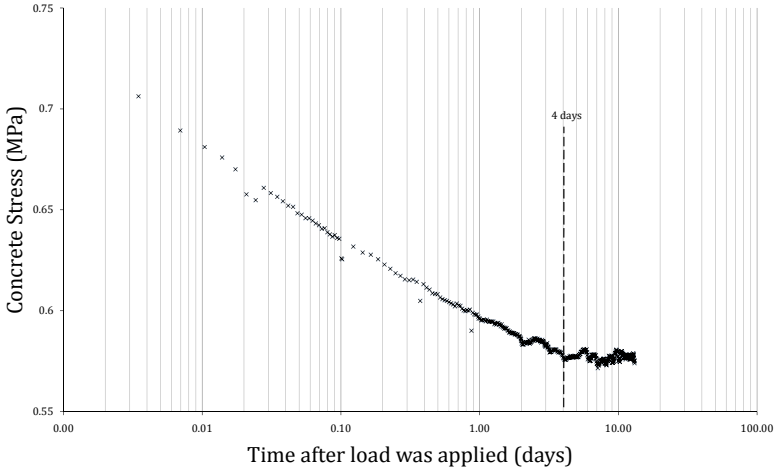

(b) Load Stage 2 (144 kN)

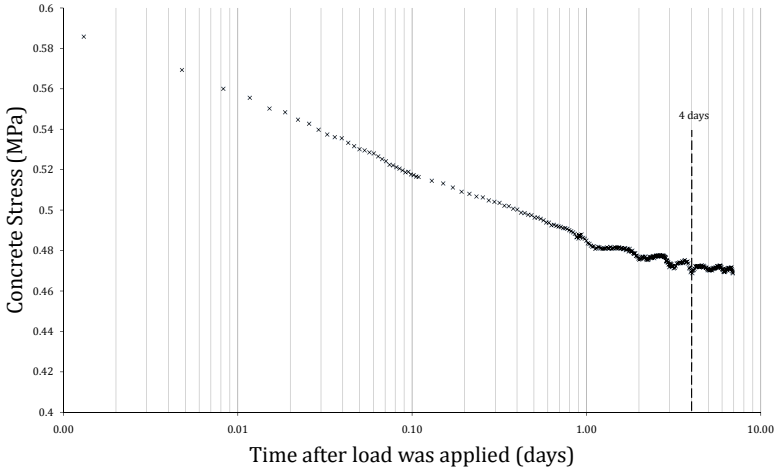

(c) Load Stage 3 (181 kN)

Figure B.2: Logarithmic plots of concrete stress against time with tension stiffening decay time indicated for H32 tests.

B.3 H40

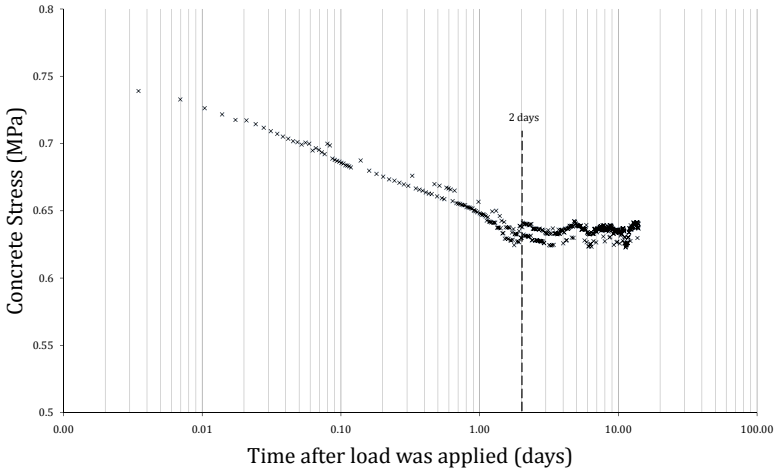

(a) Load Stage 1 (270 kN)

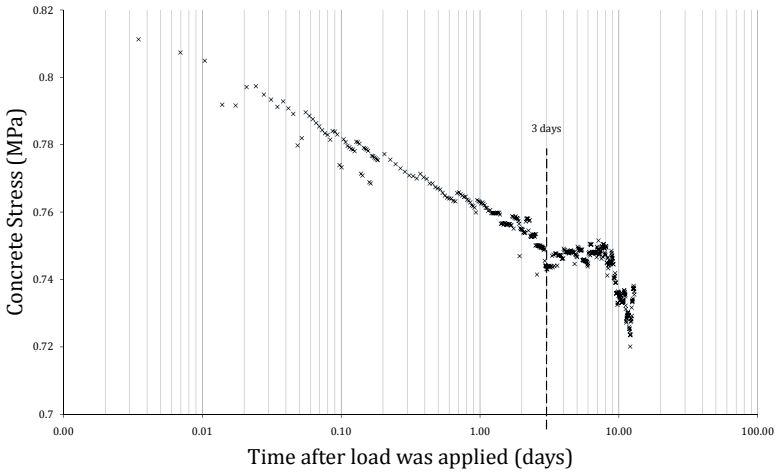

(b) Load Stage 2 (360 kN)

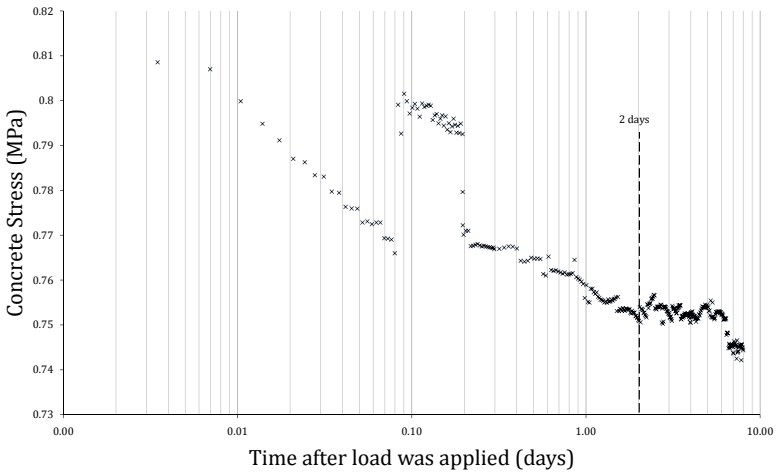

(c) Load Stage 3 (450 kN)

Figure B.3: Logarithmic plots of concrete stress against time with tension stiffening decay time indicated for H40 tests.

B.4 H50

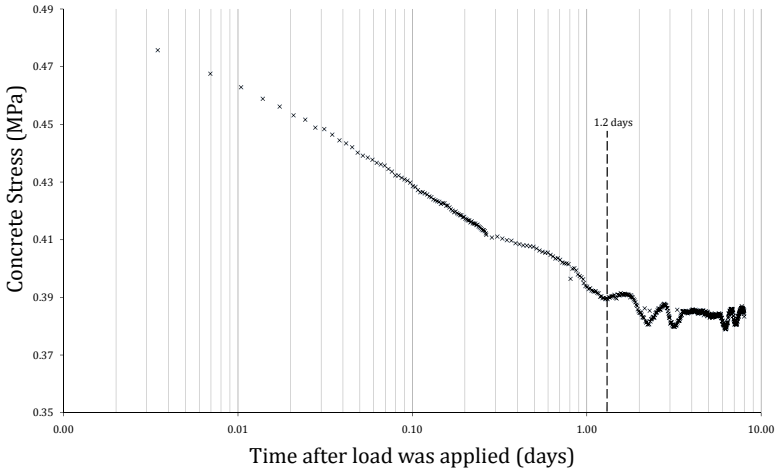

(a) Load Stage 1 (270 kN)

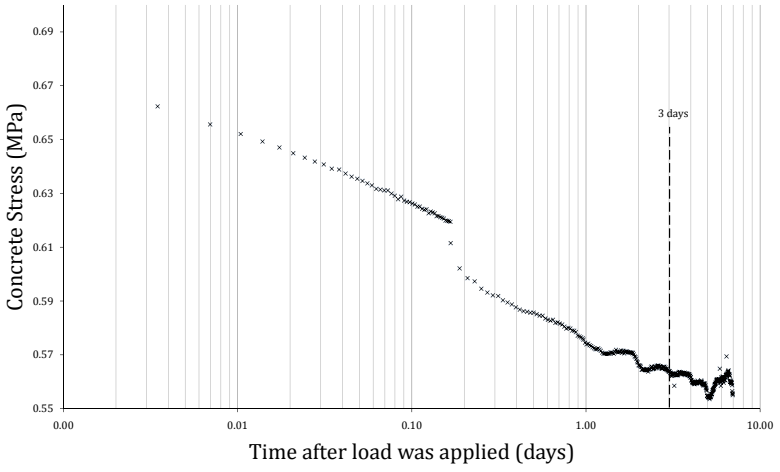

(b) Load Stage 2 (360 kN)

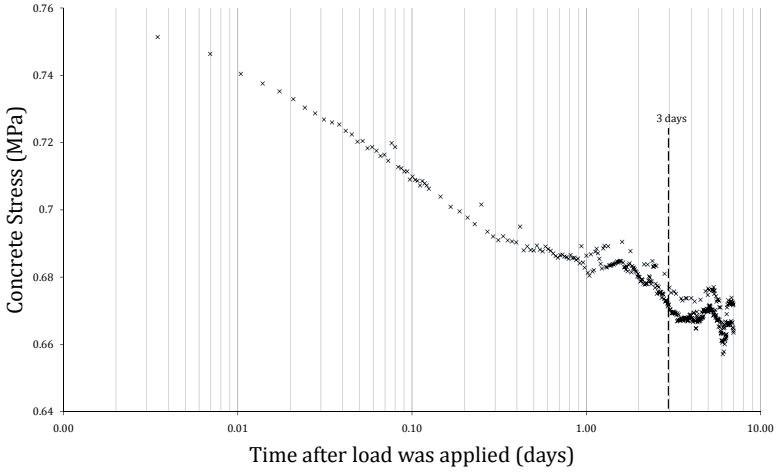

(c) Load Stage 3 (450 kN)

Figure B.4: Logarithmic plots of concrete stress against time with tension stiffening decay time indicated for H50 tests.

Appendix C

Selection of FEM Results

C.1 H25

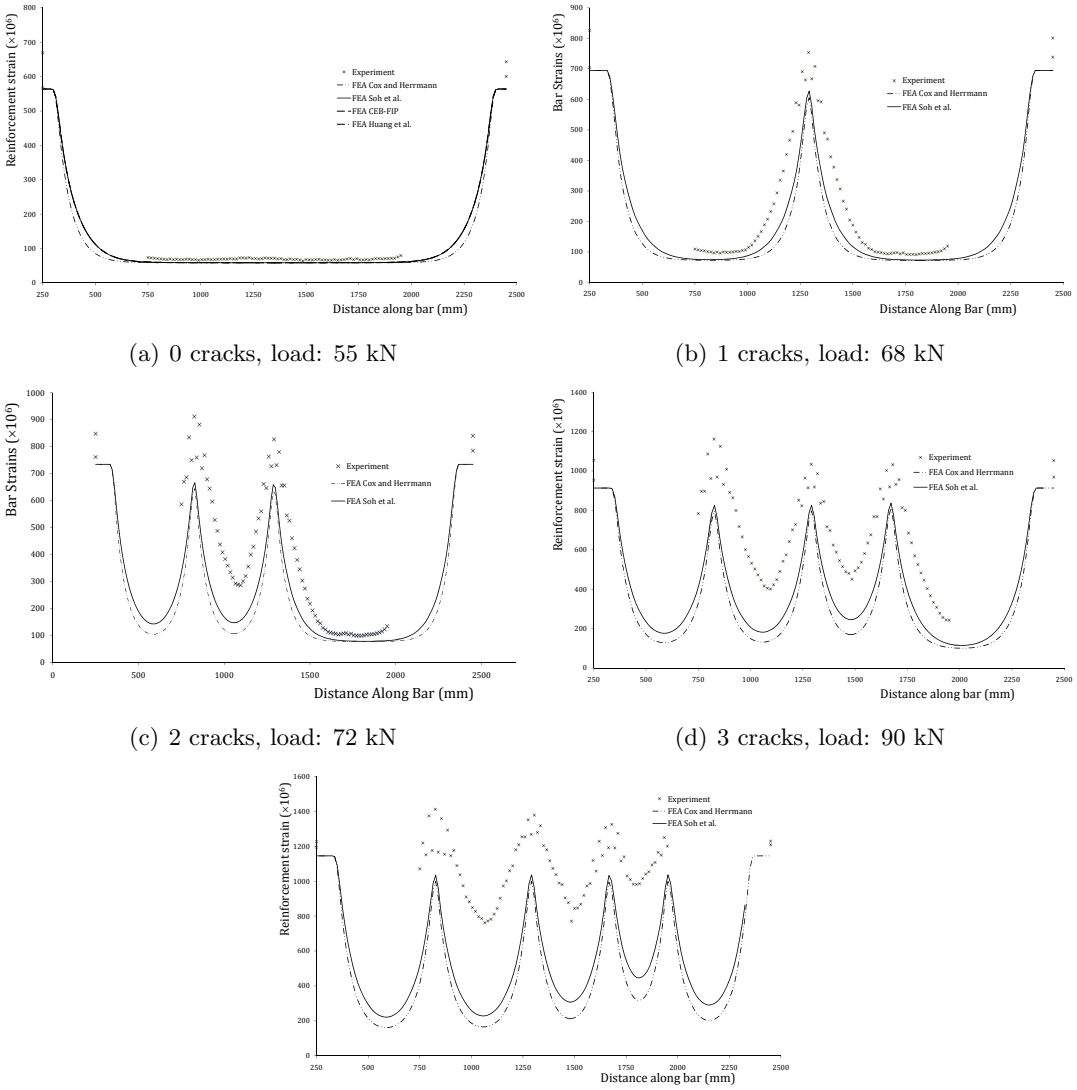

(a) 0 cracks, load: 55 kN

(b) 1 cracks, load: 68 kN

(c) 2 cracks, load: 72 kN

(d) 3 cracks, load: 90 kN

(e) 4 cracks, load: 109 kN

Figure C.1: FEM results for H25 specimen.

C.2 H32

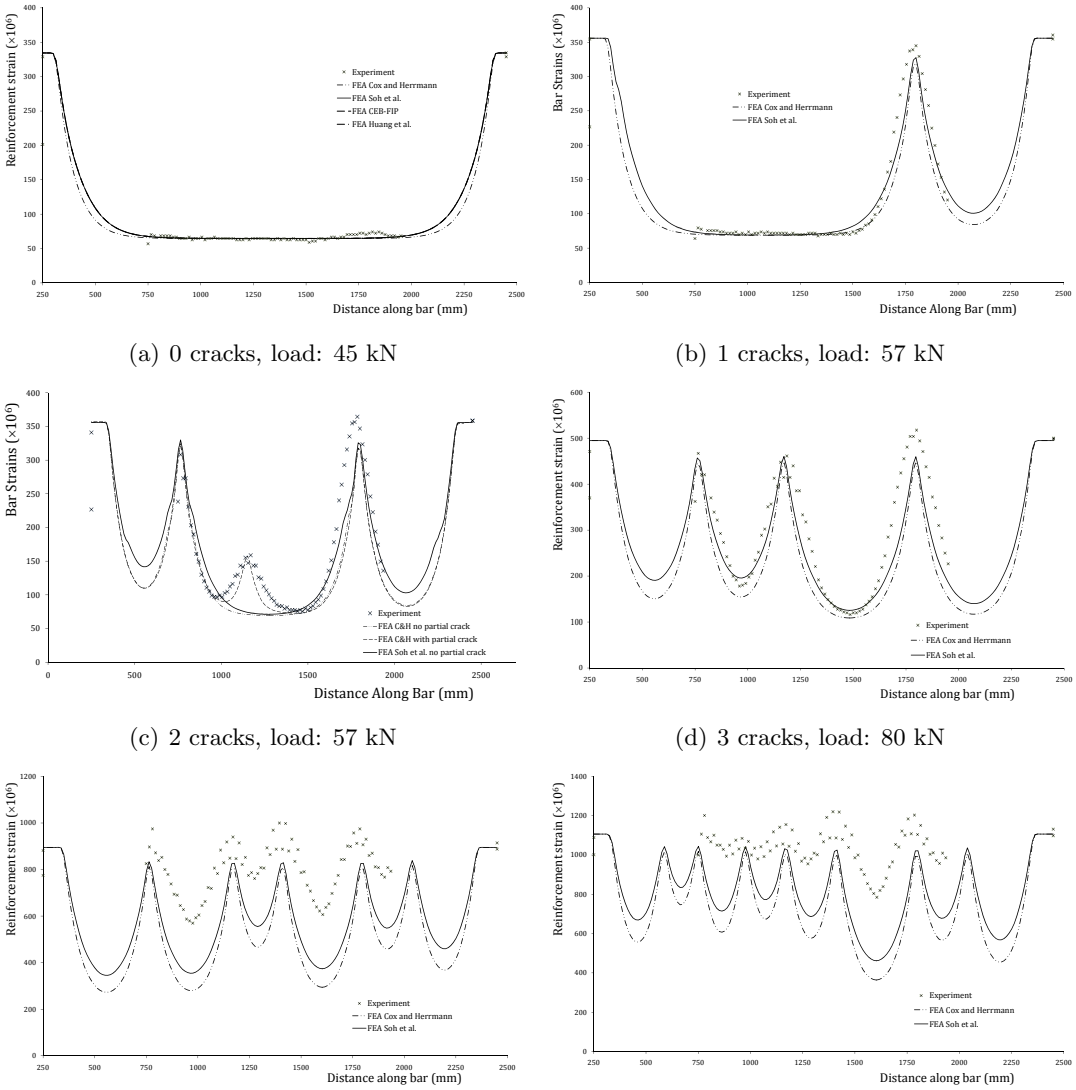

(a) 0 cracks, load: 45 kN

(b) 1 cracks, load: 57 kN

(c) 2 cracks, load: 57 kN

(d) 3 cracks, load: 80 kN

(e) 5 cracks, load: 143 kN

(f) 7 cracks, load: 177 kN

Figure C.2: FEM results for H32 specimen.

C.3 H40

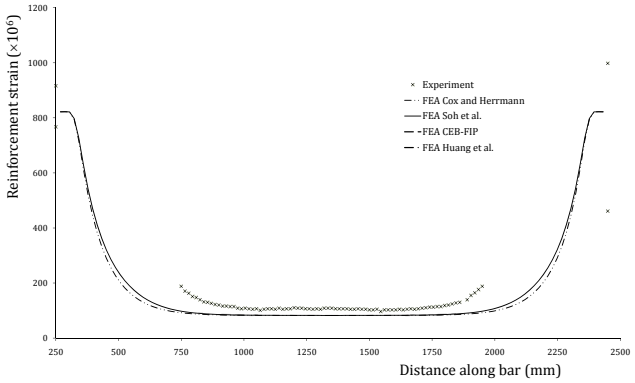

(a) 0 cracks, load: 207 kN

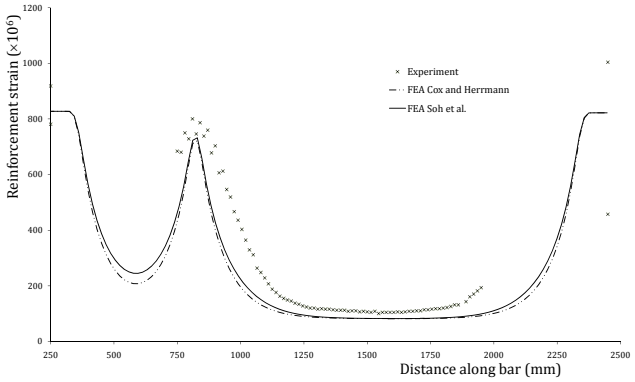

(b) 1 cracks, load: 208 kN

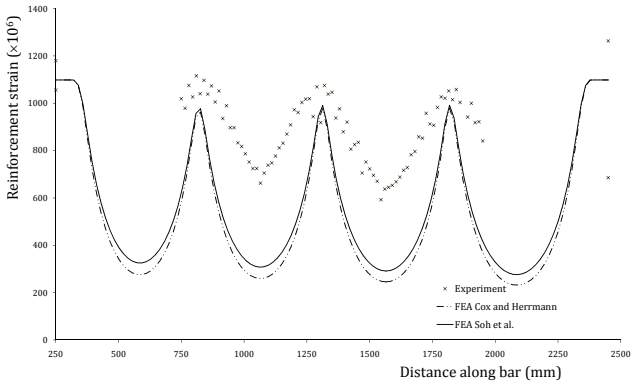

(c) 3 cracks, load: 276 kN

Figure C.3: FEM results for H40 specimen.

Note: No analysis was carried out for the two crack situation as cracks two and three occurred simultaneously and there was thus no experimental data to which the results could be compared.

C.4 H50

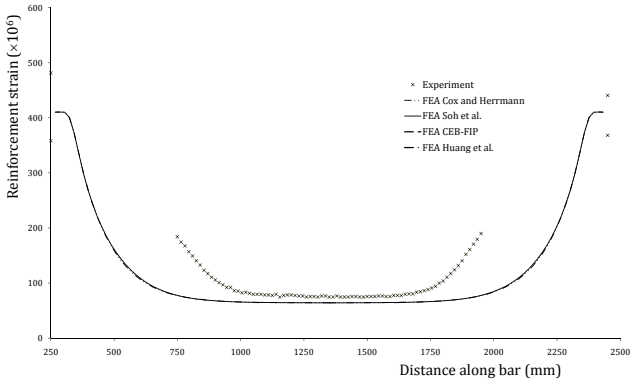

(a) 0 cracks, load: 161 kN

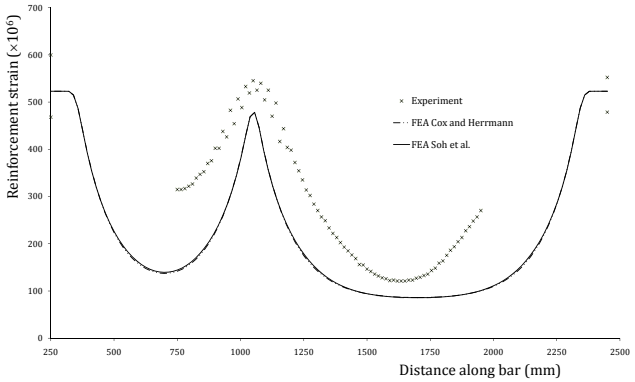

(b) 1 cracks, load: 205 kN

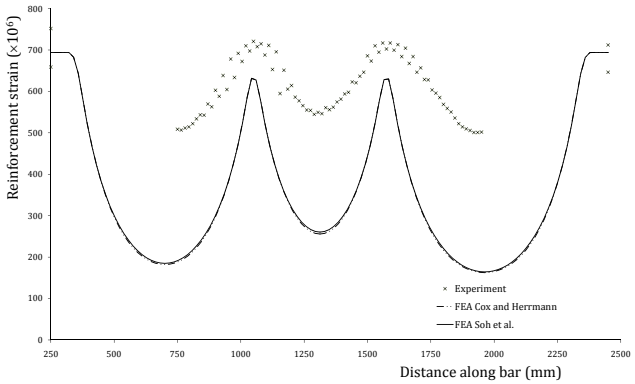

(c) 2 cracks, load: 272 kN

Figure C.4: FEM results for H50 specimen.